Cosmic Bubble Collisions

Observable Signature of A Classical Transition

Wei Lin

A Thesis Submitted to the Faculty of Graduate Studies in Partial Fulfilment of the Requirements for the Degree of Master of Science

Graduate Program in Physics and Astronomy
York University, Toronto, Ontario

May, 2015

Abstract

The theory of inflation was introduced to resolve many existing observational problems in cosmology. Inflation becomes eternal when a region of space continuously spawns non-inflation regions. This process arises from metastable vacua in a potential landscape. Our universe could be a realization of one of these many vacua predicted by the theory. In this thesis, we explored the idea that a universe can be born via a collision between two bubble universes. This process is known as a "Classical Transition". In this thesis, the potential observability of relics produced during the collision is studied. If a classical transition did happen in the past, its presence is imprinted on the CMB temperature anisotropy. In order to determine the pattern due to a primordial bubble collision, numerically simulating the entire history of a bubble collision is necessary. After running the simulation, we extracted the comoving curvature perturbation (which has a direct connection to the temperature fluctuations) from spatial slices. In our analysis, we calculated the observed CMB quadrupole for two models, $\mathcal{D}_2 \approx 1100[\mu K^2]$, as well as its correlation to the local curvature, Ω_k. In both models we studied, we showed that the produced signatures resulting from a classical transition can vary a lot. In addition, we surveyed the boundary of a classical transition for polynomial potentials in the model where false vacua are above the inflationary plateau. We showed that the position (in field space) of a classical transition boundary has a $1/\sqrt{\epsilon}$ relation to the slow-roll parameter, ϵ. In the second model where the false vacuum occupied by the nucleated bubbles are below the inflationary plateau, we confirmed that it is also possible to produce a classical transition regardless of the surrounding vacuum energy. However, the relative vacuum energy difference of the newly formed universe to its environment will potentially affect the post-collision behaviours of domain walls. In this study, we show there exist three different types of geometry in the domain wall (repulsive, marginal repulsive and oscillatory) when different surrounded vacuum energy is presented. We investigated a variety of vacua energy in the marginal limit in which the domain wall unveils a marginal repulsive geometry and showed that the new formed universe always has a vacuum energy slightly greater than its surroundings.

Acknowledgements

During this work, it is impossible for me to complete it without assistance from many people. First of all, I must thank Matthew C. Johnson for being a great supervisor and advisor. He leads me to this fascinating field of cosmology. In these couple years, I have a diverse experience in different research areas related to cosmology. The skills and broad knowledge required for studying the field of cosmology is more than I can imagine. Without his help, I would have not learnt this much. Moreover, I would like to thank my examine committee members, Michael Haslam and Roman Koniuk, for providing advices in this thesis to make it more complete. Next, many thanks to a friend of mine, Yu-Wei Huang, for helping me to illustrate some beautiful pictures in this work.

Doing research in the field of physics relies a strong background knowledge. For my undergraduate education in physics, I would like to thank those who had taught me and inspired me. Especially, I am grateful to Randy Lewis. He first introduced the subject of quantum mechanics to me and initiate my curiosity to physics. From time to time, when we have conversations about physics, his talk always enlighten me to think physics at a different angle. In the same year, I had my first research experience with Chorng-Yuan Huang from National Central University, Taiwan. Many thanks to him for supervising me, giving me this opportunity and sharing his research experience as his career.

Last but not the least, I would like to thank my colleagues, Alex Terrana, Ryan Deneault, Jesse Rogerson and George Conidis for offering hospitality and comfortable research environment, and of course, my family in Taiwan for supporting and encouraging me to continue my interest in physics.

11^{th} May, 2015

Wei Lin

Contents

List of Figures

Abbreviations

GR	**G**eneral **R**elativity
dS	**d**e **S**itter space
AdS	**A**nti **d**e **S**itter space
CDL	**C**oleman **D**e **L**uccia
HM	**H**awking **M**oss
CMB	**C**osmic **M**icrowave **B**ackground
LSS	**L**arge **S**cale **S**tructure
SZe	**S**unyaev **Z**el'dovich **e**ffect
AIP	**A**bove **I**nflationary **P**lateau
BIP	**B**elow **I**nflationary **P**lateau
FRW	**F**reidmann **R**obertson **W**alker

Chapter 1

Introduction

Cosmology is the study of the Universe. This includes how it is formed, how it has evolved and its ultimate fate in the future. The standard picture of modern cosmology postulates that the Universe started out hot and dense. As time progresses, the Universe expands and starts to cool down. At the point where the temperature was approximately 3000 K, the radiation decoupled from the electron-proton plasma and the Universe became transparent. This radiation which is observed today (from all direction) is red-shifted to the microwave range and form the comic microwave background (hereafter CMB). The golden age of cosmology begins after the discovery of the CMB [Penzias and Wilson, 1965]. Detecting the CMB radiation gives us access to an early image of our Universe and allows us to test the cosmological model. The uniformity of the CMB indicates that our observable Universe is nearly homogeneous and isotropic.

The predominant model which gives the initial conditions for the above features in modern cosmology is inflation (see section 1.1). In the idea of inflation, it is possible that inflating regions inside a universe will continue to spawn (non-)inflating regions such that inflation becomes everlasting. This process of continuously breeding new generations of (bubble or pocket) universes is usually referred as eternal inflation (see section 1.1.4) and our Universe may be among these younger generations. In eternal inflation, as Alan Guth says, "Anything that can happen will happen, and it will happen an infinite number of times." At first glance, this is probably one of the most radical ideas in modern theoretical physics. Despite that, the idea behind eternal inflation is universally

accepted. Since everything can happen in eternal inflation, this opens up many questions to the idea itself. People tackle and tend to complete this idea via different avenues, from a conventional basis by simply asking what are the aftermaths of the theory to an abstract level such as answering questions to where the theory itself might produce self-inconsistent arguments. Since our Universe is not unique in eternal inflation, it is possible that there exists other bubble universes and have collided with ours in the past. Our primary work concentrates on making several predictions for signatures on the CMB resulting from collisions between these universes (or bubble collisions) according to the idea. By comparing the predicted to the observed CMB signatures, this allows us to constrain and test the validity of eternal inflation. Specifically, the signatures produced by bubble collisions depend on the underlying potential and creation mechanism of bubbles. A bubble collision signature resulting from quantum tunnelling was studied recently by [Wainwright et al., 2014a,b]. This thesis is intended to focus on exploring the signature via a new mechanism that has not yet been studied before which is known as a "classical transition" (see section 1.2.2). There are some key questions that we want to address and answer in this thesis for the purpose of knowing if eternal inflation is a viable description of our Universe. First, is it possible that our Universe can result from a classical transition? Second, if our Universe is a consequence of a classical transition, what signatures do we expect to observe in the CMB? Last, is it possible to distinguish between a universe that results from quantum tunnelling and one that results from a classical transition?

1.1 What's Inflation?

Our expanding Universe can be described by an Friedmann Robertson Walker (hereafter FRW) metric of the form

$$ds^2 = -dt^2 + a(t)^2[\gamma_{ij}dx^i dx^j] \tag{1.1}$$

where $a(t)$ is the scale factor that indicates how fast the physical distance grows and γ_{ij} is the spatial metric which describes the geometry of a hypersurface embedded in a $4D$ spacetime. Inflation is an era in the history of the Universe where the scale factor super-grows. In a typical inflationary model the scale factor usually grows exponentially,

namely,

$$a \propto e^{Ht} \tag{1.2}$$

where H is the Hubble parameter that tells how fast the physical distance grows by powers of e.

1.1.1 Motivation

Inflation potentially solves many existing puzzles which arises from the observation of the CMB and the physical circumstances of our Universe itself. First of all, as mentioned, the CMB reveals an isotropic and homogeneous Universe. However, given the time since the beginning of the Universe until the formation of the CMB, there is a finite distance in which light can travel across the Universe. This is typically at the order of $\sim (aH)^{-1}$ and is about one degree as seen today on the CMB. Parts larger than a degree are essentially not in causal contact, yet we still observe a same temperature profile to a part in 10^5. This is usually referred as the *horizon problem*. The way that an inflation theory reconciles this problem is that there was an epoch during which our entire Universe could equilibrate and then when inflation happens, it drives the points to regions that are not in causal contact; This additionally explains why our Universe is so big. Secondly, the fact that our Universe is nearly flat often requires some fine tuning of initial conditions. This can be seen if matter is expressed in terms of fraction of energy density today, Ω. According to the Friedmann equation, the fraction of the critical energy density today after summing up all the contributions is nearly one[Planck et al., 2015], ie,

$$\Omega = \sum_i \Omega_i = 0.9993 \pm 0.0033, \tag{1.3}$$

where i indicates the contents that makes up the Universe. For example, radiation, matter and the cosmological constant. The deviation of Ω from one is the amount by which the spatial curvature contributes to the system; ie,

$$\Omega - 1 = \Omega_k. \tag{1.4}$$

When Ω is negative, 0 or positive, it represents the spatial curvature is either positive, flat or negative, respectively. As one can see from Eq. (1.3) and Eq. (1.4), there is no reason for Ω_k to be zero unless one specifies the contribution from the curvature in the

beginning. However, in inflation, as can be seen from Eq. (1.2),

$$\Omega_k \propto a^{-2} \propto e^{-Ht}. \tag{1.5}$$

Regardless what value of Ω_k started out with, inflation will always drive it to zero asymptotically. This solves the flatness problem. In addition to this, inflation also accounts for the fact that our Universe is magnetic monopole-free[Guth, 2007] if magnetic monopoles were produced during the epoch before the inflation. The expansion of space dilutes the population of magnetic monopole to the point where they are negligible today.

1.1.2 Potential Landscape

The condition of inflation, in Eq. (1.2), is quite general and provide a simple solution to the above problems yet. However, there is no specific theory that drives inflation and many features that arise from an inflation model depend on its underlying "potential landscape" of scalar fields. The configuration of the potential landscape can result from a well-motivated theory; string theory, for example. In a potential landscape, each point (in field space) can be interpreted as producing coupling constants or mass of particles through the Higgs mechanism. The degrees of freedom in the scalar fields are based on the choice of a specific model. In the simplest case, we consider a potential with a single scalar field which is sufficient to capture the basic properties for our study.

1.1.3 Different Inflationary Models

The original proposal of inflation that was intended to resolve the problems mentioned in section 1.1.1 is the so called "old inflation." In this model, the potential landscape is depicted in Fig. 1.1 where there exists two local minima separated by a barrier. The value of the potential at these minima (in a scalar field theory) is the energy density of a universe in which we referred the higher potential as the false vacuum and the global minima as a true vacua. In this picture, a universe was initially occupied by a vacuum state, V_A, and start to inflate. At the end of inflation, the field decays into V_B and new phase emerges from the background. This process is bubble nucleation. The duration of inflation should provide the scale factor to grow by a factor of $\gtrsim e^{60}$ in order to give

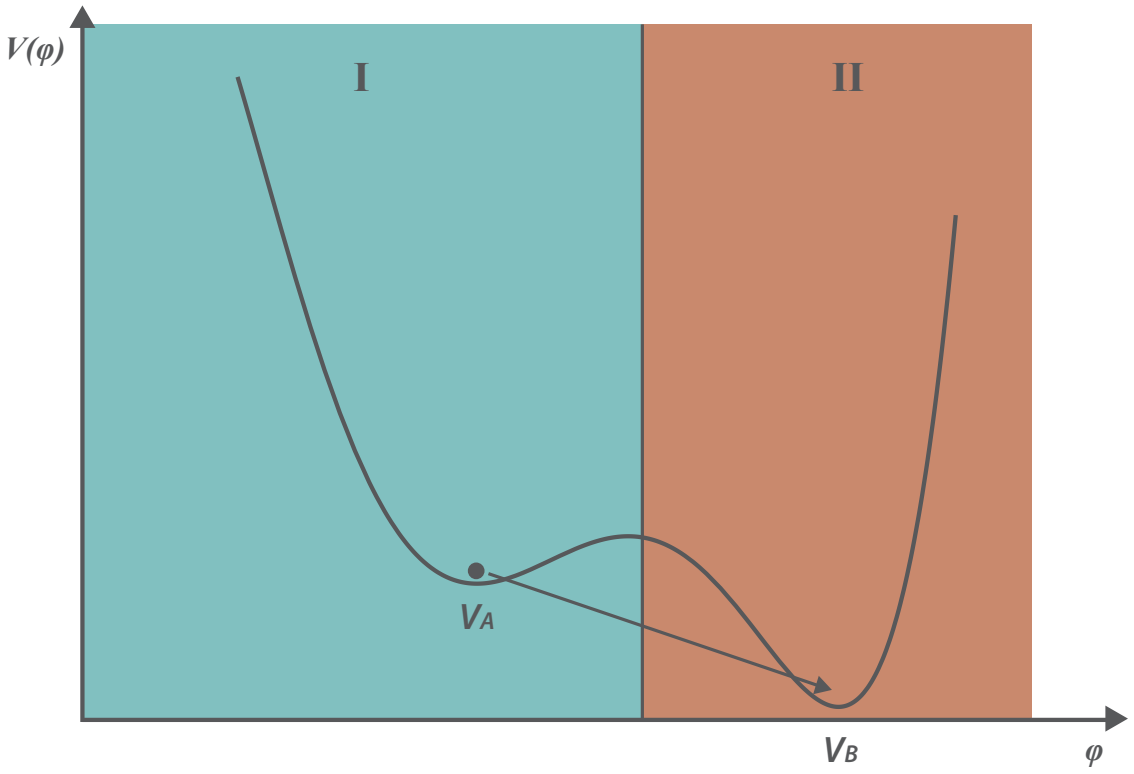

FIGURE 1.1: A potential landscape for an old inflationary model.

the features mentioned in section 1.1.1. The Hubble parameter in the expression of Eq. (1.2) characterises the expansion rate and is related to the vacuum energy by

$$H^2 = \frac{8\pi}{3}V. \tag{1.6}$$

For a universe to reheat homogeneously at V_B, this requires that many new formed bubbles to collide in order to thermalize the universe. However, this also requires the nucleation rate of the bubbles out of the false vacuum to be large enough. A detailed study by Guth and Weinberg [Guth and Weinberg, 1983] showed that the required decay rate of the field to the true vacuum from the false in order to provide homogeneous and isotropic universe is too large to solve the horizon and the flatness problem. In other words, the percolation complete too soon for inflation to end before it reaches 60 e-folds. One way to reconcile this problem is instead of having an inflation trapped in a local minimum, the field slowly rolls down a nearly constant potential subject to the condition $\dot{H}/H^2 \ll 1$ (where "$\cdot$" indicates time-derivative). This is depicted Fig 1.2, and the Universe reheats homogeneously at V_C as the field oscillates around the minimum. The inflation arises from this type of potential is known as "new inflation" (or slow-roll inflation)[Linde, 1982].

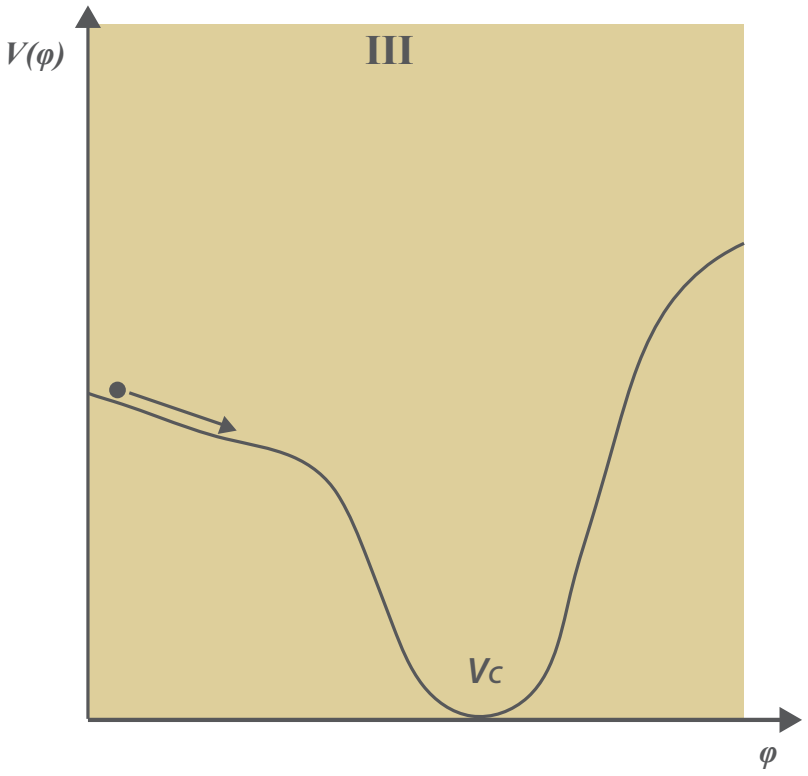

FIGURE 1.2: A potential landscape for a new inflationary model.

1.1.4 The Eternal Nature of Inflation

Recall that in old inflation, inflation stops when the background false vacuum is percolated. However, if there is still space for new bubbles to form at each Hubble time as inflation progresses, inflation becomes eternal or everlasting. A schematic diagram of such process is shown in Fig. 1.3.

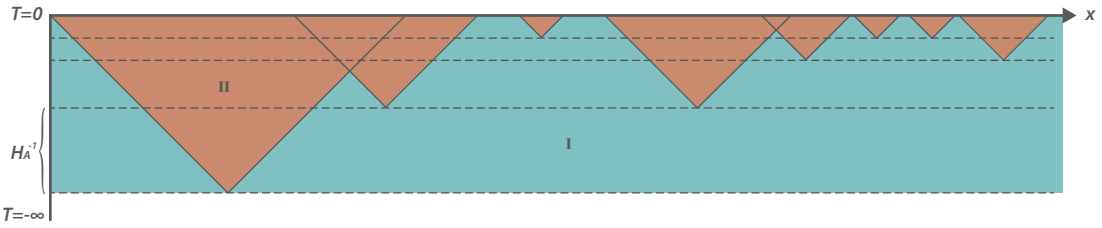

FIGURE 1.3: Bubble nucleations at different time slices. When $\gamma_A \lesssim 1$ as shown in the diagram, eternal inflation is everlasting and has a fractal structure at the future infinity.

In the diagram, the background dS space is foliated in the conformally flat slicing and the null ray travels at 45 degrees. For now, let us focus on the old inflation model with

two vacua which is labelled by region I and II. The characteristic time scale here is the Hubble time, H_A^{-1}, associated with the false vacuum (V_A). When the nucleation rate $\Gamma \gtrsim H_A^4$, the transition will reach completion and inflation ends. If $\Gamma \lesssim H_A^4$, the nucleation rate will not outrun the expansion rate, and inflation persists. The condition for Γ not outrunning the expansion can be rewritten in a dimensionless form

$$\gamma_A = \Gamma H_A^{-4} \lesssim 1. \tag{1.7}$$

If the condition in Eq. (1.7) is met at every time step, inflation goes on forever. This defines "eternal inflation." In addition, at each Hubble time that inflation progresses, the volume grows exponentially. This allows more room for bubbles to form at a later time. Eventually, this system will produce a fractal [Winitzki, 2002] at future infinity.

The eternal nature of inflation is usually a hybrid between the new and the old inflation although eternal inflation can exist in a new inflationary picture alone. For example, in New Eternal Inflation, the field can be at the top of a potential and decay exponentially with time. As it decays, bubbles expand at the same time. Another example is Chaotic Eternal Inflation. In chaotic eternal inflation[Linde, 1986], the field due to quantum mechanics will fluctuate. On average, if the deviation of the field fluctuation is greater than a Hubble length within a Hubble time, parts of universe possessing different field values will essentially not be in causal contact. Thus, different regions of universe will evolve independently and create many mini universes.

In the hybrid picture of the new and the old inflation, slow-roll inflation is followed by a potential with one or more local minima as depicted in Fig. 1.4 (This will also be the picture for studying bubble collisions.) The slow-roll inflation in region III is mandatory in order to explain the existing cosmology. In addition, region I and II provide the feature of eternal inflation in which bubbles can emerge from the background vacuum, V_A as the field tunnels through the first barrier. Subsequently, bubbles can collide in region II and trigger a classical transition (see description in section 1.2.2) to produce the next generation bubbles. During the process of bubble creation, the condition in Eq. (1.7) needs to be satisfied for inflation to be eternal.

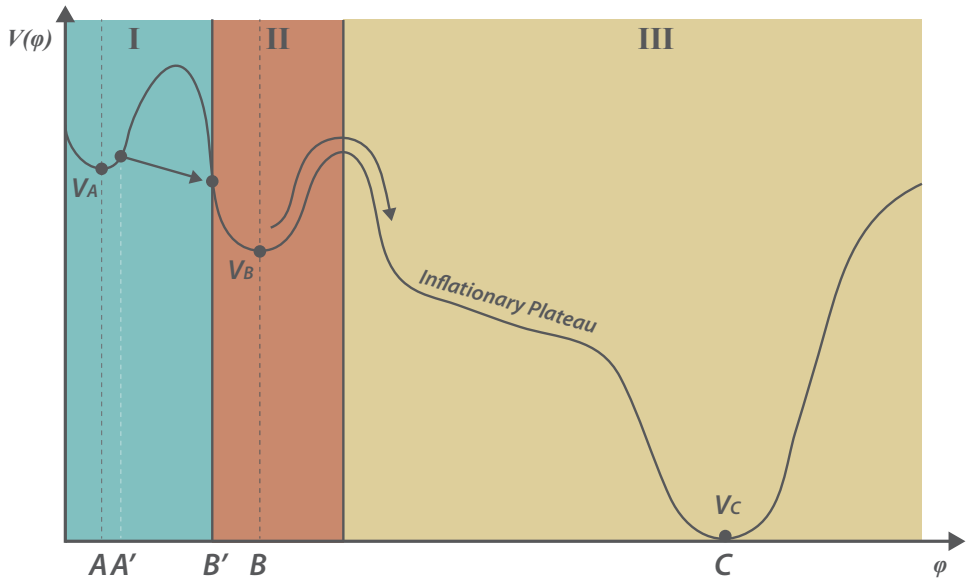

FIGURE 1.4: A viable potential landscape.

1.2 Bubble Creation Mechanisms

In the discussion of eternal inflation, a universe can give birth to the next generation universe. Here, we show how this process can occur in two different ways. First, a vacuum state is metastable quantum mechanically. If initially there only exists one single universe, say, occupied by V_A, the bubble creation process can only happen quantum mechanically. However, as soon as the first transition takes place, this opens up a new window where a chain of subsequent bubble creations can occur classically.

1.2.1 Quantum Transition

The process of bubble materialization via quantum tunnelling can happen in two ways. Firstly, as first studied by Coleman in flat space[Coleman, 1977, Callan and Coleman, 1977] where this process taken via quantum tunnelling. Later, Coleman and De Luccia (hereafter CDL) advanced the theory by including the gravity[Coleman and Luccia, 1980] with a semi-classical treatment. Secondly, as studied by Gibbon and Hawking[Gibbon and Hawking, 1977], the properties of a dS patch can be captured by a "thermal" system with a temperature of $H/2\pi$. In a thermal system, Hawking and Moss (hereafter HM)[Hawking and Moss, 1982] showed that the fluctuations due to thermal energy will allow the field to stochastically climb up the barrier (as mentioned in the discussion of

chaotic eternal inflation in section 1.1.4).

For the purpose of our model study, we will apply the CDL instanton and discuss this mechanism in more depth here. An instanton possesses an $O(4)$ symmetry and has a Euclidean metric that takes the form

$$ds^2 = dr^2 + \rho(r)^2 d\Omega_3^2, \tag{1.8}$$

where r is the bubble's Euclidean radius and $d\Omega_3^2$ is the metric on a three-sphere. The function $\rho(r)$ determines the radius of curvature. The equations of motion that govern the instanton can be derived from its Euclidean action (S_E). The field equation is

$$\frac{d^2\phi}{dr^2} + \frac{3}{\rho}\frac{d\rho}{dr}\frac{d\phi}{dr} = \frac{dV}{d\phi}, \tag{1.9}$$

and the equation for ρ is

$$\frac{d^2\rho}{dr^2} = -\frac{8\pi G}{3}\rho\left[\left(\frac{d\phi}{dr}\right)^2 + V\right]. \tag{1.10}$$

A non-trivial solution to these equations of motion can be found by interpolating between A' and B' as indicated in Fig. 1.4. This demands the following boundary conditions: $d\phi/dr|_{(r \text{ at } A')} = d\phi/dr|_{(r \text{ at } B')} = 0$ and $d\rho/dr|_{(r \text{ at } A')} = d\rho/dr|_{(r \text{ at } B')} = 1$. To transform a real spacetime to an Euclidean space, one makes a change of variable from real time to an imaginary time. This essentially affects a sign difference in the potential in Fig. 1.4 from $V(\phi)$ to $-V(\phi)$. A schematic diagram of an instanton in Euclidean geometry is shown in the lower panel of Fig. 1.5. In the diagram, a four sphere is embedded in a five dimensional Euclidean space. The X_0 is the temporal direction in an ordinary spacetime while X_i suppresses the other four spatial dimensions. As one can see, the top of the sphere flattens after the instanton tunnels through the barrier because the radius of curvature corresponds to a different vacuum energy at B' [1].

To study the subsequent behaviour of bubbles that nucleate at different spatial points, one must analytically continue the Euclidean instanton to an ordinary spacetime. The Euclidean $O(4)$ invariance becomes $O(3,1)$ invariance, and the interior of each daughter

[1] The radius of the sphere can be categorized by the characteristic distance scale, H, in which for $R_{A'} \sim H_A^{-1}$ and $R_{B'} \sim H_B^{-1}$. From Eq. (1.6), a smaller vacuum energy gives a smaller H.

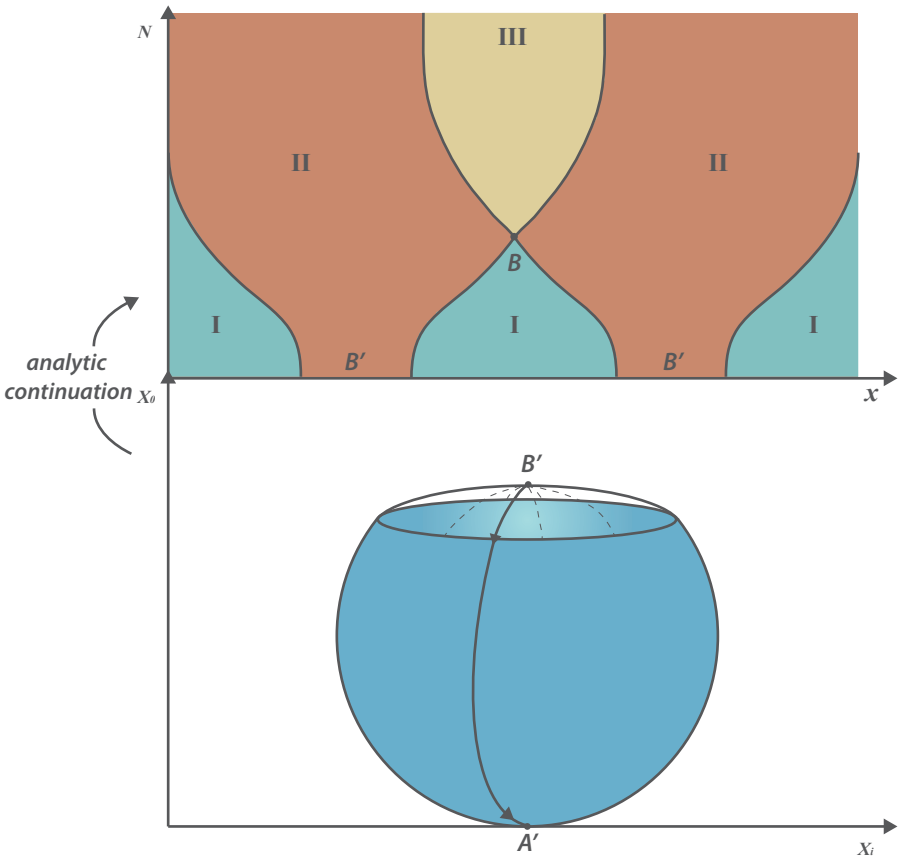

FIGURE 1.5: A schematic diagram showing the process from an instanton tunnelling to a bubble collision.

universe is described by an opened FRW metric. Furthermore, one can show that, in this first order phase transition, the evolution of the domain wall approaches the speed of light after bubble nucleation. This is due to the potential energy difference across the wall and the liberated vacuum energy is transferred to the kinetic energy of the domain wall.

1.2.2 Classical Transition

In a classical transition, when two or more bubbles collide, the energy is large enough such that it kicks the field over the barrier and give birth to the next generation universes[Easther et al., 2009]. Therefore, in the initial stage, when there are no bubbles, it is impossible to trigger a classical transition. This implies that a viable potential configuration for studying a classical transition requires at least two local minima before the field reaches the true vacuum. As one might guess, besides the shape of a potential, what determines a successful classical transition depends on the energy at the collision

point. This can be parametrized by the Lorentz factor, γ, at the collision and is given by

$$\gamma = \frac{\Delta x}{R}, \tag{1.11}$$

where Δx and R are the initial separation of bubbles and the initial radius, respectively. In Eq. (1.11), both quantities are measured in the units of the background Hubble parameter H_A. A classical transition will only occur after reaching a certain threshold. If the energy is insufficient, the field will return to its original vacuum state. However, there is no analytic solution that determines the exact form of the threshold. This can only be done by numerically simulating collisions. When the colliding energy reaches the threshold, a classical transition will always occurs regardless if the surrounding vacuum energy of the new formed bubble is higher or lower as we will see in chapter 3.

By now, we have a much clearer understanding of Fig. 1.4, and it is worth summarizing the logic flow here with a Penrose diagram as shown in Fig. 1.6. In the diagram, a dS patch of region I is occupied by V_A. A CDL instanton tunnels through the barrier to the field value B' and as the field rolls to V_B, its walls expand asymptotically to speed of light (labelled by lines of 45 degrees). If the bubbles are not too widely separated, there is a chance that they will collide and this event takes place at B (at $\eta = \pi/2$). When the walls have sufficient energy, the collision will trigger a classical transition and the field get kicked over the second barrier. The field has a period of slow roll inflation (labelled by region III) until reaching the Minkowskian minimum (yellow patch). If the collision energy is insufficient to bring the field over the barrier, it will return to V_B (region II).

1.3 Previous Work

Some numerical studies have been done to study a classical transition. In [Easther et al., 2009], a classical transition is successfully produced when two bubbles collide in the absence of gravity. In an earlier study of the aftermaths between two colliding bubbles, Hawking, Moss and Stewart[Hawking et al., 1982] showed that it is possible to produce a newly formed bubble in which its parent universes are occupied by a lower vacuum state. However, since this new born bubble is surrounded by a lower vacuum state, it collapses quickly. More recently, a classical transition (in Ref. [Johnson and Yang, 2010]) is

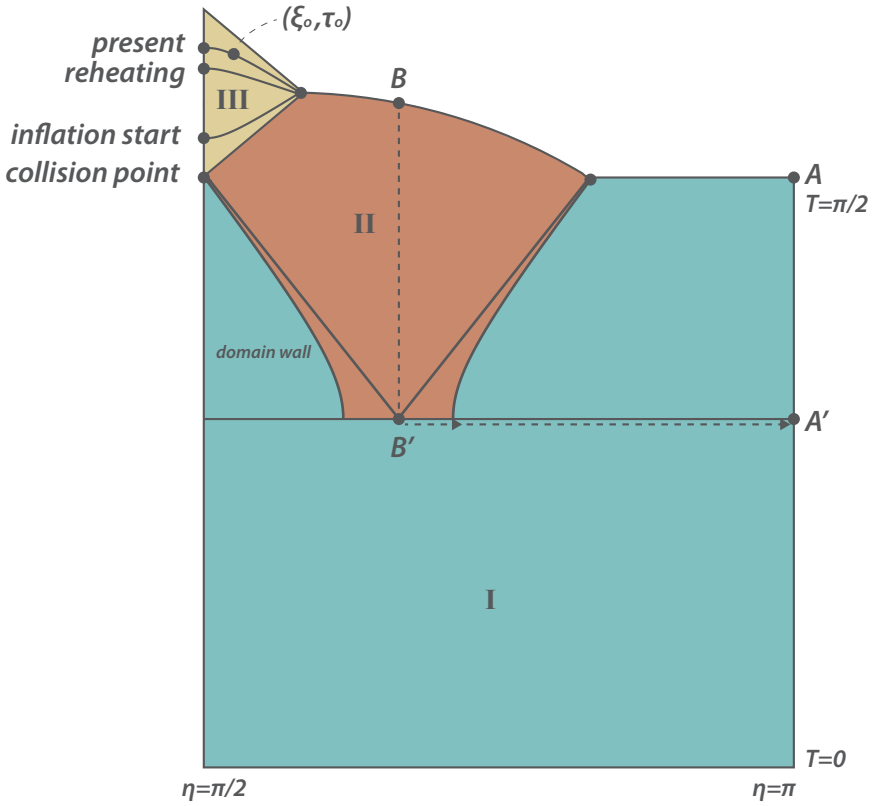

FIGURE 1.6: The digram shows a bubble nucleates at a field value of B' where the background dS patch is closed foliated (where $0 \leq \eta \leq \pi$ and $-\pi/2 \leq T \leq \pi/2$). As one moves away from the nucleation point (as indicated by the arrow,) one hits the domain wall first and enter region I. Eventually, when it reaches the spatial infinity (at $\eta = \pi$), it will return to the point (in field space) before the instanton tunnelled through (labelled by A'. As an comparison, see lower panel of Fig. 1.5.) Furthermore, if it waits long enough (at future infinity labelled by $T = \pi/2$), it will settle back to the false vacuum, V_A, in which the field value is at A. Inside region II, the future infinity is also a dS patch, where the bubble is occupied by V_B and the field value takes place at B. To the left of the diagram, after nucleation, the field rolls to V_B and the collision takes place at the same field value, B. As an aside, we have suppressed the other half of the picture such that the collision occurs at $\eta = \pi/2$. If a classical transition happens, the field will finally reach V_C and a Minkowski space is patched on top of a dS space (which is labelled by region III.) In region III, the events happen at different constant time surfaces as indicated. Notice that observers labelled by (ξ_o, τ_o) and live along the present surface will have a causal patch that intersects with the future light cone of the collision point. This means, all observers inside the bubble will have access to the information left behind from the collision.

studied in full general relativity. In this work, the post-collision domain wall has different geometrical properties. In the case where the gravity is absent, the domain walls can have a "Normal" or "Oscillatory" geometries when the surrounding vacuum of a newly formed bubble is lower/higher. When the gravity is included, two additional geometries in the domain walls unveil ("Repulsive" and "Marginal Repulsive" geometries). In the picture of these domain wall geometries, different geometries are classified according to how domain walls move away from each other in the post-collision. For a normal geometry, the domain walls are always normal to each other and move away from the lower to higher vacuum regions. In an oscillatory geometry, the domain walls initially move away from each other. However, since the newly formed bubble is occupied by a higher vacuum energy than its surrounding, the domain walls eventually turn around and collapse. In a repulsive and a marginal repulsive geometries of the domain walls, due the repulsive nature of gravitation in addition to the expansion rate of the newly formed bubble, it is possible for the domain walls to create a lasting region to prevent the newly formed bubble from collapsing even when its surrounding vacuum is lower. This will be one of the key features that we will explore in this thesis (see section 2.2.2 and section 3.4 for the second model).

1.4 Observing A Bubble Collision Signature

In section 1.2.2, we have mentioned that the collisions between bubbles can result in a classical transition. In fact, any bubble has a chance to collide regardless of it being produced by a quantum or a classical transition. If they did collide in the past and we happen to be in one of these bubbles, can we actually tell that we are the outcome of a collision?

This question was addressed and a substantial amount of work has been done to test the observability of this bubble collision signatures[Hawking et al., 1982, Aguirre and Johnson, 2009, Aguirre et al., 2007, Aguirre and Johnson, 2008, Kleban et al., 2011, Feeney et al., 2011a, Chang et al., 2009, Czech et al., 2010, Feeney et al., 2011b, Wu, 1983, Moss, Freivogel et al., 2007, Chang et al., 2008, Aguirre et al., 2009, Johnson et al., 2012, Salem, 2012, Feeney et al., 2013, McEwen et al., 2012, Osborne et al., 2013]. In principle, the relics left from the collisions is imprinted on the CMB anisotropy. Recently, various methods (using the large scale structure [Larjo and Levi, 2010, Alvarez et al., 2014]

(hereafter LSS) and the Sunyaev Zel'dovich effect[Zhang and Johnson, 2015](hereafter SZe) for example) were proposed to test the idea of bubble collisions. To check that if the produced signature is compatible with the CMB anisotropy, one needs to know the pattern of it. Some previous studies have predicted a distinctive pattern on the CMB anisotropy[Wainwright et al., 2014b, Kleban et al., 2011, Feeney et al., 2011a, Chang et al., 2009, Czech et al., 2010, Feeney et al., 2011b, Kozaczuk and Aguirre, 2012] in which the prediction can only be made via simulating the entire process of bubble collision[Wainwright et al., 2014a,b]. A direct impact from the bubble collisions is causing a perturbation in comoving curvature, $\mathcal{R}$ (see section 1.4.1). The effect on $\mathcal{R}$ is preserved as soon as the field enters slow roll inflation, where it freezes in on super-horizon scales. Consequently, $\mathcal{R}$ is insensitive to the details during the period of reheating and the relics from bubble collisions can still be observed today. Specifically, in the study of a quantum transition bubble collision[Wainwright et al., 2014a,b], they gave a prediction on what the signature would look like on the CMB. On the basis of this, the scope of this work is to investigate a potential observability via a classical transition (region III in upper panel of Fig. 1.5). If we were the observers that inhabit a bubble resulting from a classical transition, what signatures do we expect to see?

1.4.1 Comoving Curvature Perturbation

In the above paragraph, we discuss a direct impact of a bubble collision causes the comoving curvature perturbation, $\mathcal{R}$, and that quantity has a direct relation to the CMB (see section 3.1). In this subsection, we will elaborate how $\mathcal{R}$ is defined from a theoretical point of view, and in the next section, we will show how to calculate it directly from the simulation. The comoving curvature perturbation is the metric perturbation defined in a gauge where a local observer is moving with the coordinate. In other words, in this coordinate system (which is also referred as comoving gauge), the spatial components of an observer's four velocity vanishes, $\mathcal{U}^i = 0$ where $\mathcal{U}^i$ is the spatial component of the four velocity of the observer and $i = 1, 2, 3$). By construction, $\mathcal{R}$ is a gauge invariant quantity and is defined in an observer's Cartesian coordinate in theory. However, a residual $SO(2, 1)$ symmetry left from the collision intuitively allows us to approximate different patches of the bubble locally by a perturbed open FRW Universe. In this case, a convenient choice of coordinate system will be an anisotropic hyperbolic coordinate.

Therefore, in what follows, we will first make a connection (for $\mathcal{R}$) between a Cartesian and an anisotropic hyperbolic coordinate and then we will adapt the anisotropic hyperbolic coordinates to calculate the comoving curvature perturbation directly from the simulation (see section 1.4.3 for simulation outputs).

According to the cosmological perturbation theory, the perturbation of an induced FRW metric (g_{ij}) on a comoving hypersurface can in general be written as

$$g_{ij} = a(\tau)^2(1 + 2\mathcal{R})\delta_{ij}, \tag{1.12}$$

where $a(\tau)$ is the scale factor. The perturbed metric in Eq. (1.12) has a trivial transformation rule between coordinate systems since $\mathcal{R}$ is a gauge invariant quantity by definition and a is purely τ-dependent. To transform the coordinate system from Cartesian to anisotropic hyperbolic coordinates, we apply the transformation rule,

$$\begin{aligned} \sinh\xi &= \frac{X}{1 - \frac{R_{\rm curv}^2}{4}}, \\ \tanh\chi &= \frac{\sqrt{Y^2 + Z^2}}{1 + \frac{R_{\rm curv}^2}{4}}, \\ \tan\psi &= \frac{Z}{Y}; \end{aligned} \tag{1.13}$$

or equivalently

$$\begin{aligned} X &= \frac{2\sinh\xi}{1 + \cosh\xi\cosh\chi}, \\ Y &= \frac{2\sinh\chi\cosh\xi}{1 + \cosh\xi\cosh\chi}\cos\psi, \\ Z &= \frac{2\sinh\chi\cosh\xi}{1 + \cosh\xi\cosh\chi}\sin\psi. \end{aligned} \tag{1.14}$$

In both Eq. (1.13) and (1.14), $R_{\rm curv}$ represents the radius of curvature and is a tunable free parameter. Due to the planer symmetry in $\mathcal{R}(X)$, we can set $\chi = \psi = 0$ in Eq. (1.14) to simplify the algebra. In the era where curvature is not a dominant contribution (such as today where $R_{\rm curv}$ is negligible) and in the limit near the bubble center (where ξ is small), we can approximate $\sinh\xi = X/[1 - R_{\rm curv}^2/4]$ as $X \approx \xi$. Thus, $\mathcal{R}(X) = \mathcal{R}(\xi)$. This is the comoving curvature perturbation as seen by an observer at the bubble center.

In order to go to an arbitrary frame labelled by ξ_0, where the comoving curvature perturbation at ξ_0 is $\mathcal{R}(\xi')$, we need to know how X transforms to X' first and make a connection between ξ_0 and ξ'. This process can be done by performing a boost in the X direction. A boost that brings X to X' corresponds to a shift in ξ to ξ' by an amount of ξ_0, namely $\xi' = \xi - \xi_0$. The intuition here is that since ξ labels different rapidity of the observers on a hyperbola, and boosting in the X direction is equivalent to moving from one point to another on the hyperbola. Therefore, we have the relation, $\mathcal{R}(\xi') = \mathcal{R}(\xi - \xi_0)$ (see Ref [Wainwright et al., 2014a] for detailed description).

The next step is to obtain $\mathcal{R}''(\xi_0)$ from $\mathcal{R}(\xi - \xi_0)$ since it is the most relevant to the CMB power spectrum. Furthermore, one can relate the temperature variation in the CMB and the primordial perturbation of comoving curvature in the Sachs Wolfe limit (see section 3.1). To do this, note that the observers who live inside the bubble has to travel infinity proper distance to reach the bubble wall (see Fig. 1.7). Since the comoving curvature perturbation is only ξ dependent, and the proper distance labelled by ξ never touches the wall[2], we expect $\mathcal{R}$ to be a smooth function. As a result, the observer will see a C^∞ comoving curvature perturbation.

This allow us to expand $\mathcal{R}(\xi - \xi_0)$ in a power series,

$$\mathcal{R}(\xi - \xi_0) \approx \mathcal{R}(\xi_0) + \mathcal{R}'(\xi_0)(\xi - \xi_0) + \frac{1}{2}\mathcal{R}''(\xi_0)(\xi - \xi_0)^2 + ... \tag{1.15}$$

The first term in the expansion corresponds to rescaling of the scale factor and is irrelevant since we can always pick a reference point and normalize it to one. The linear term ($\mathcal{R}'$) corresponds to coordinate velocity, and observers can always go to a comoving frame locally. Thus, the leading term in the expansion is the quadratic term.

1.4.2 Simulation Procedure

To make the numerical simulation feasible, we will consider one bubble collision signature resulting from two colliding bubbles. Recall that the spacetime possesses an $SO(3,1)$ hyperbolic symmetry (if we exclude time-reversal and parity symmetry). During the collision, the intersection of two hyperboloids will break the symmetry from $SO(3,1)$

[2]The wall is located at infinite proper distance away

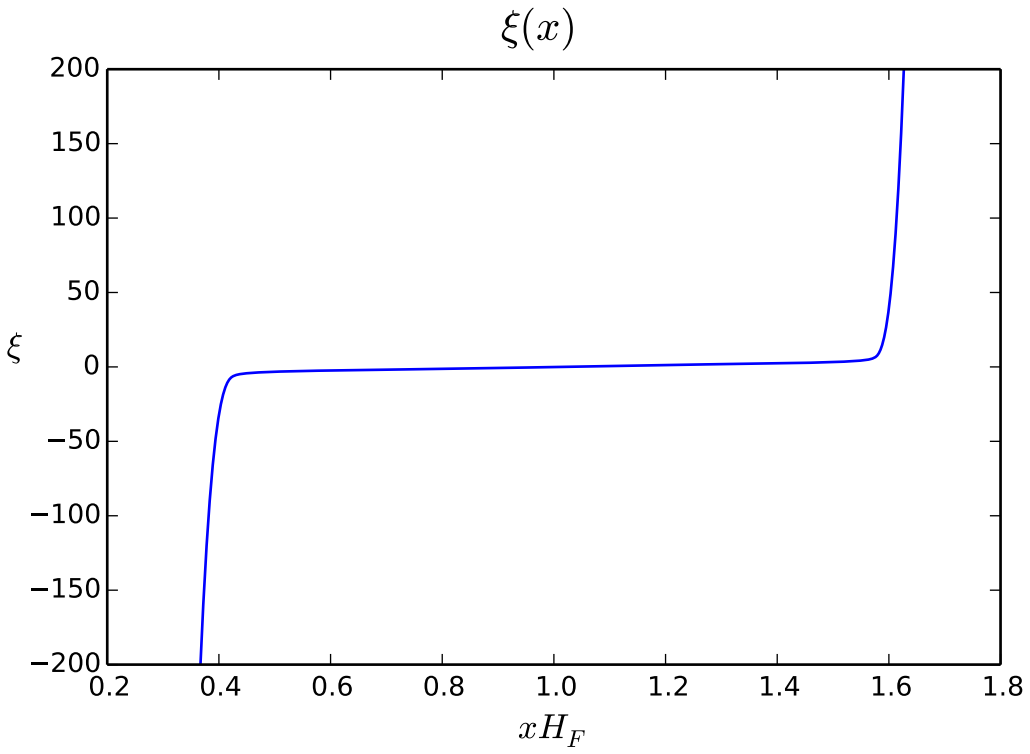

FIGURE 1.7: Anisotrpic hyperbolic coordinate, ξ, as a function of spatial simulation coordinate, xH_F. One can see that as ξ deviate away from the bubble center (corresponds to $xH_F = 1$), ξ asymptotically approaches the bubble wall. However, observers at any particular location labelled by ξ will never touch the wall. In order to reach the wall, they will need to travel an infinite proper distance.

to $SO(2,1)$. This allows one to perform the simulation in $1+1$ dimensions[Aguirre and Johnson, 2009]. In this work, we study a classical transition by using the package developed in [Wainwright et al., 2014a] and [Wainwright, 2006-2013]. To begin, we must define a potential to initiate the simulation. The potential should have the properties as depicted in Fig. 1.4 with two metastable false vacua and a true vacuum. The first barrier in between two false vacua provides the behaviour of an CDL instanton and the second barrier in between the inflationary plateau and the second false vacuum state gives rise to the classical transition. A specific model is chosen in chapter 2, and we will describe how this process is done in the remaining section.

First step: Instanton Profile The configuration of two identical bubbles nucleated at different spatial points are categorised by two wave packets (or solitons). These initial wave packets is given by the instanton profile that solves the Euclidean equations of motion. Since we assume that the instanton only connects points

A and B (in Fig. 1.4), the code will intake the parameter associated with the potential of the first barrier. Specifically, in our model, the first barrier is specified by two parameters, its amplitude and width. In addition to the shape of the potential, we must specify the positions (in field space) of the false vacua as well. This is because the code uses an iterative overshoot and undershoot method to interpolate between A' and B'. The reason for interpolating between A' and B' instead of A and B is due to the semiclassical analysis of the instanton profile. The field is stable at those metastable minima and if we start the field at A, it will not move. Therefore, the initial guess of $V(\phi)$ must be less than V_A. When the field has the exact momentum (after releasing from A'), it will stop at B' exactly with the radius associated with B' at that point. This is our solution. If the momentum is too large, $d\phi/dr \neq 0|_{r \text{ at } B'}$, the field will pass B'. This is an overshoot, and the initial guess of ϕ_0 must be modified to a higher vacuum energy. On the other hand, if the momentum is insufficient, the field will stop before reaching r associated with B' and return to A'. This is an undershoot, and the initial guess for ϕ_0 must be changed to a lower vacuum energy. This overshoot/undershoot method is implemented in the package in [Wainwright, 2006-2013] for finding the solution to the equations of motion.

Second step: Analytic Continuation to Simulation Spacetime To simulate bubble collisions, one analytically continues the Euclidean solution to the simulation spacetime with the metric given by[Wainwright et al., 2014a],

$$H_A^2 ds^2 = -\alpha^2(N,x)dN^2 + a^2(N,x)\cosh^2 N dx^2 + \sinh^2 N(d\chi^2 + \sinh^2\chi d\psi^2) \quad (1.16)$$

where N measures the numbers of false vacuum e-foldings, x labels the physical spatial distance, χ labels different rapidity as one performs boost perpendicular to the x-axis, and ψ labels the angular distance about the x-axis. The $\alpha(N,x)$ and $a(N,x)$ are unknown metric functions. In the pure de Sitter patch, $\alpha = a = 1$. The field equation in the simulation spacetime then becomes

$$\begin{aligned} &\frac{1}{\sqrt{-g}}\partial_\mu(\sqrt{-g}g^{\mu\nu}\partial_\nu\phi) = \partial_\phi V \\ &\Rightarrow \frac{d\Pi}{dN} = -\left[\tanh(N) + \frac{2}{\tanh(N)}\right]\Pi + \frac{d}{dx}\left[\frac{\alpha d\phi/dx}{a\cosh^2(N)}\right] - \alpha a\partial_\phi V \end{aligned} \quad (1.17)$$

and the Einstein equations are

$$\begin{aligned} \frac{d\alpha}{dN} &= \alpha(A+B) \\ \frac{da}{dN} &= a(-A+B) \end{aligned} \tag{1.18}$$

with the following definition of Π, A and B:

$$\begin{aligned} &\Pi \equiv \frac{a}{\alpha}\frac{d\phi}{dN}, \\ &A \equiv \tanh(N) + \frac{1}{2\tanh(N)} - \frac{\alpha^2}{2}\left[\frac{1}{\cosh(N)\sinh(N)} + 8\pi\tanh(N)V\right], \\ &B \equiv 2\pi\tanh(N)\frac{\alpha^2}{a^2}\left[\frac{(d\phi/dx)^2}{\cosh^2(N)} + \Pi^2\right]. \end{aligned} \tag{1.19}$$

The solution to these equation needs to satisfy the constraint equation:

$$\frac{d\alpha}{dx} = \frac{4\pi\tanh(N)\alpha^2\Pi d\phi/dx}{a}. \tag{1.20}$$

To evolve the above equation, we need a set of initial conditions for α, a and Π. In order to find these initial conditions, we must first identify the instanton solution after analytic continuation. In a dS patch, the metric in Eq. (1.8) after analytic continuation becomes

$$ds^2 = dr^2 + \rho^2(r)[-d\Psi^2 + \cosh^2\Psi d\Omega_2^2]. \tag{1.21}$$

When $\Psi = 0$, this is the throat of the dS in the absence of a bubble. On the other hand, in the limit where $N \to 0$, the simulation coordinates can be approximated as a slicing in Minkowski space of an $SO(2)$ symmetry. This can also be identified as the throat of the dS in which the metric takes the form

$$H_A^2 ds^2 = dN^2 + dx^2 + N^2 dH_2^2. \tag{1.22}$$

From Eq. (1.21) and Eq. (1.22), we see the coordinates x and r both measures the proper distance along the throat of the dS. Therefore, we can replace the instanton solution in Euclidean space by making a change of $\phi(r) \to \phi(x)$. Now, we have enough information to determine the initial conditions for the metric functions and the field equation. In the small N limit, we can perform a Taylor expansion about $N = 0$ (see Ref. [Johnson et al., 2012] for more detail) for ϕ, α, a and Π.

The lowest surviving terms are

$$\begin{aligned} \alpha &= 1 - \alpha_2(x)N^2 \\ a &= 1 + a_2(x)N^2 \\ \Pi &= 2\phi_2(x)N \\ \phi &= \phi_0(x) + \phi_2(x)N^2. \end{aligned} \tag{1.23}$$

We can solve $\alpha_2(x)$, $a_2(x)$ and $\phi_2(x)$ in terms of $\phi_0(x)$ by plugging Eq. (1.23) into the constraint and evolution equations. This gives,

$$\begin{aligned} \alpha_2 &= -\frac{1}{2} + \frac{2\pi}{3}[2V(\phi_0) - \phi_0'^2] \\ a_2 &= -\frac{1}{2} + \frac{4\pi}{3}[V(\phi_0) + \phi_0'^2] \\ \phi_2 &= \frac{1}{6}\left(\phi_0'' - \partial_\phi V|_{\phi_0}\right), \end{aligned} \tag{1.24}$$

where a prime denotes x derivative. Eq. (1.24) will then be used as an initial condition for the simulation.

Third step: Integration To integrate the above equations, the code use the method of lines[Baumgarte and Shapiro, 2010]. This done by finite differencing the x coordinate, and the equations of motion that involves the first and second spatial derivative can be calculated using the difference in grid point and the adjacent field values. For example, the first derivative can be calculated to the fourth order in Δx_{diff} as

$$\frac{dy_i}{dx} = \frac{y_{i-2} - 8y_{i-1} + 8y_{i+1} - y_{i+2}}{12\Delta x_{diff}} + \mathcal{O}(\Delta x_{diff}^4). \tag{1.25}$$

For a uniform grid, Δx_{diff} is the same. However, a uniform grid is not feasible in this context since the wall is length contracted as it approaches to the speed of light and the solution to the metric functions requires a higher resolution near the wall. To increased the resolution locally, the code implements the adaptive mesh refinement to take into account a non-uniform differentiation stencil in which the grid separation near the wall is finer. This turns a set of coupled partial differential equations into a set of coupled ordinary differential equations. To

integrate in the temporal direction, the code use a standard fourth order Runge-Kutta method. The time step for each integration is set by the Courant-Friedrichs-Lewy condition[Courant et al., 1928] which demands that the time step must be smaller than the time it takes for information to travel between adjacent points.

1.4.3 Simulation Inputs and Outputs

Inputs: As mentioned in section 1.4.2, the instanton profile is completely determined by the shape of the potential and the positions of the false vacua. However, this is not the whole story, and there is a subtly needs to be cleared up. Since the instanton is obtained by interpolating between A' and B', and the solution does not cover the point at the metastable minima. The point to which the instanton tunnels is not at V_B in Fig. 1.4. In fact, A' can be really close to A as long as it provides the right amount of momentum for the instanton to tunnel. However, the instanton endpoint on the other side the barrier has no restriction. The point at which the instanton re-emerge can be at V_B if two barriers are close enough or on the hillside if two barriers are separated far apart. This gives an additional parameter (shift between the barriers) that might potentially affect the shape of an instanton profile as we will see in section 2.2.1. In addition, in the thin wall limit, an instanton profile is essentially a step function. In this case, the size of the barrier width is proportional to the initial bubble radius; whereas, while maintaining the same barrier width, the barrier amplitude is inversely proportional to the initial bubble radius[Aguirre and Johnson, 2008]. On the other hand, besides the shape of a potential, the physical condition of two colliding bubble need to be taken into account as well. As a classical transition is determined by the Lorentz factor at the collision point, according to Eq. (1.11), the initial bubble separation is a potential source that will affect the outcome. Therefore, the input parameters: position of the two metastable false vacua, height and width of the barriers, shift between barriers, and the initial bubble separation completely determine the outputs of the simulation.

Outputs: The goal of the simulation is to extract $\mathcal{R}$. This quantity has the most direct connection to the observable CMB anisotropy. To find $\mathcal{R}$, we look for a constant field spatial slice at late time when the perturbation freezes in and the field value at that point is only defined at the interior of the bubble. This allows us to calculate the

comoving curvature perturbation directly from the simulation result and not to worry about the post-collision evolution.

Since the simulation coordinates cover the entire collision spacetime, it is more intuitive to go to the anisotropic hyperbolic coordinates system which covers the interior of a bubble. To calculate the comoving curvature perturbation directly from the simulation, we first label proper distance along the comoving slice by u in which it is defined as

$$u(x) = \int_0^x \sqrt{a^2 \cosh^2 N - \left(\alpha \frac{dN}{dx}\right)^2}\, dx'. \tag{1.26}$$

Thus, Eq. (1.16) becomes

$$H_A^2 ds^2 = du^2 + \sinh^2 N(u)(d\chi^2 + \sinh^2 \chi d\psi^2). \tag{1.27}$$

Note that Eq. (1.27) is only defined on a space-like surface. This implies the integrand in Eq. (1.26) is positive definite. The next step is we wish to write Eq. (1.27) in terms of an open FRW metric plus a small perturbation in the anisotropic hyperbolic coordinates,

$$H_A^2 ds^2 = a_0^2[d\xi^2 + (1-2B)\cosh^2 \xi(d\chi^2 + \sinh^2 \chi d\psi^2)] \tag{1.28}$$

where ξ labels rapidity in the X direction in the Cartesian coordinate system as we will see later. One can identify the relation between Eq. (1.27) and Eq. (1.28) by a linear transformation in u, namely,

$$u - u_0 = a_0(\xi - \xi_0), \tag{1.29}$$

where u_0, a_0 and ξ_0 are yet to be specified, and

$$1 - 2B = \frac{\sinh^2 N(u)}{a_0^2 \cosh^2 \xi}. \tag{1.30}$$

When $B = 0$, Eq. (1.28) reduces to the unperturbed anisotropic hyperbolic coordinates and a_0 is the scale factor. If B represents a perturbation, in the neighbourhood of some observer u_0, $B = dB/d\xi = 0$. This gives the expression for a_0 and ξ_0

$$\begin{aligned} a_0 &= \frac{\sinh N_0}{\cosh N_0} \\ \xi_0 &= \sinh^{-1}\left(\cosh N_0 \frac{dN_0}{du_0}\right), \end{aligned} \tag{1.31}$$

where $N_0 = N(u_0)$ and the scale factor a_0 is observer dependent along a comoving slice. To find the comoving curvature perturbation, we find the Ricci scalar (${}^3R$) of the hypersurface with Eq. (1.28),

$$ {}^3R(\xi) = -6 + \nabla^2\mathcal{R}. \tag{1.32}$$

This defines the comoving curvature. Since ${}^3R$ depends on ξ alone, we expect $\mathcal{R}$ is only a function of ξ. Thus,

$$ \nabla^2\mathcal{R} = \left(\partial_\xi^2 + \frac{2\tanh\xi - 2\partial_\xi B}{1-2B}\right)\mathcal{R}. \tag{1.33}$$

$\mathcal{R}$ can be found by integrating Eq. (1.33) with the integration constants: $\mathcal{R}(\xi_0) = d\mathcal{R}/d\xi|_{\xi_0} = 0$. The choice of these integration constants are explained in section 1.4.1 (see the explanation for Eq. (1.15)).

1.4.4 Signatures Resulting from Different Mechanisms

Are we able to tell the difference if our Universe is a result of a classical or a quantum transitions? In the previous study of a bubble collision signature, our Universe is a result of a quantum transition[Wainwright et al., 2014a]. The collision only affects the universe partially in which the comoving curvature perturbation only exists near the collision boundary. However, in the study of a classical transition which we are about to explore, the collision affects the whole universe. Therefore, the comoving curvature perturbation covers the entire sky. These distinct patterns of comoving curvature perturbation resulting from two mechanisms can potentially be distinguished, depending on the observers' location inside the bubble. In the quantum transition case, if an observer happened to live near the collision boundary, he/she will only see a perturbation that covers their sky partially; or equivalently, the observer will see the comoving curvature perturbation appear to affect higher modes in the CMB angular power spectrum. However, if observers' location moves towards the collision region. Eventually, the collision disk covers the entire sky and affects the lower mode in the CMB power spectrum. On the contrary, in a bubble resulting from a classical transition, regardless where the

observers are located, they should always observe a relic left behind from a bubble collision and the perturbation should affect the lowest mode in the CMB spectrum. We explore the properties of such signature, and the results of this are presented in chapter 3

Chapter 2

Modelling

2.1 Constructing Model and Goals

To initiate the simulation, we need to start with a potential that gives eternal inflation. However, the modern standard picture of cosmology with slow-roll inflation explains our Universe successfully, and we do not want to spoil its success after introducing eternal inflation. Therefore, the potential must contain region III in Fig. 1.4. On top of it, as mentioned, a universe resulting from a classical transition requires two additional local minima (regions I and II) as depicted in Fig. 1.4. In this chapter, we will investigate two different types of models (see section 2.2). In the first type of model, we explore the properties of a potential where both barriers are above the inflationary plateau (hereafter AIP). Since the aftermath of a bubble collision is related directly to how two solitons pass each other at the collision point. Because of this, the most intuitive way to study the outcome of a bubble collision is by changing the initial configuration of the solitons (or the instanton profile equivalently). As mentioned in section 1.4.3, the instanton profile is found according to the shape of the potential and the positions of the false vacua. Therefore, we will discuss how each parameter associated with the potential affects the shape of an instanton profile in section 2.2.1, and then explain how to obtain a set of parameters associated instanton profiles for studying the outcome of a bubble collision. In the second model, we look into where the second barrier of the potential is below the inflationary plateau (–hereafter BIP– see the left panel of Fig. 2.1.) In this case, since V_B is possible to lie below the inflationary plateau (depends on the amplitude of the second barrier), the vacuum energy during the transient phase, $V_{\rm TP}$ (the region

before the field enters inflation) may become greater than V_B. Based on the relative energy difference between V_B and $V_{\rm TP}$, one can in general categorize the geometrical behaviours of a domain wall that separate region II and III into "Repulsive", "Marginal Repulsive" and "Oscillatory" geometry (see the right panel of Fig. 2.1) as studied in [Johnson and Yang, 2010]. In this previous study, it has been shown that there is a clear distinction in the energy difference for a repulsive and oscillatory geometry. In the former, $V_B > V_{\rm TP}$ and the latter, $V_B < V_{\rm TP}$. However, it is unclear for a marginal repulsive geometry. This leads us to the most interesting case in which we would like to explore the properties of a marginal repulsive geometry of a domain wall since the relative energy difference in V_B and $V_{\rm TP}$ are in the marginal limit. In what follows, we will continue with the study in [Johnson and Yang, 2010] and make several predictions in the case of a marginal repulsive geometry (see section 2.2.2). The verification of these predictions will be presented in the next chapter.

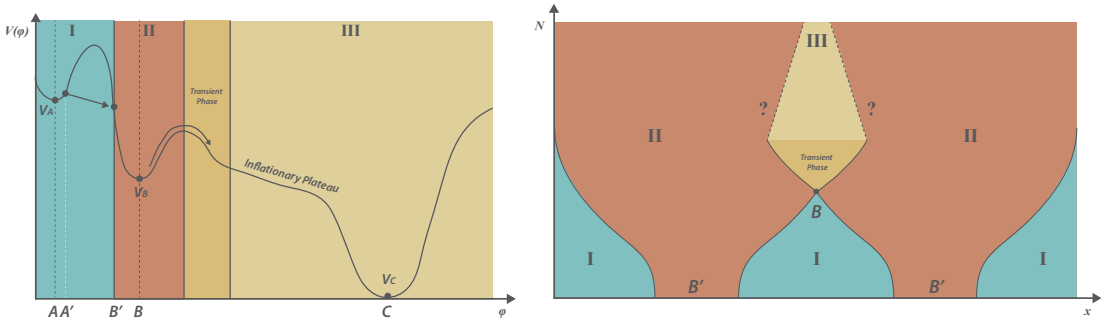

FIGURE 2.1: Schematic diagram of a potential landscape and bubble collision spacetime for the second model.

2.2 Gaussian-Quadratic Potential Model

As a particular model, we use a quadratic potential with two Gaussian bumps. The choice of this model is arbitrary, there might exist a more motivated potential that can be derived from a well established theory. Despite the fact that a Gaussian model is a random choice, it is convenient to manipulate since there are more independent variables that are tunable. The potential takes the form,

$$V(\phi) = A_1 Exp\left[-\frac{\phi^2}{2\Delta\phi_1^2}\right] \pm A_2 Exp\left[-\frac{(\phi-\sigma)^2}{2\Delta\phi_2^2}\right] + \frac{1}{2}m^2(\phi-\phi_0)^2, \qquad (2.1)$$

where the "+" is referred to the AIP case and the "−" for the BIP case. To make our models compatible with a slow-roll inflation, we need a slow roll phase which generates 60 e-folding (to resolve the problem mentioned in section 1.1.1). This requires $\Delta\phi_{CCT} \approx M_p$ and $\Delta\phi_{AB} \sim \Delta\phi_{BCT} \ll M_p$, where $\Delta\phi_{CCT} \equiv \phi_C - \phi_{CT}$ with ϕ_{CT} being the classical transition boundary, $\Delta\phi_{AB} \equiv \phi_B - \phi_A$ and $\Delta\phi_{BCT} \equiv \phi_{CT} - \phi_B$. Therefore, we set $\phi_0 = 2M_p$ such that the location for both bumps are significantly far away from V_C. Also, in Eq. (2.1), we define the amplitudes, $A_1 \equiv \beta_1|m^2\phi_0\Delta\phi_1 e^{1/2}|$ and $A_2 \equiv \beta_2|m^2\phi_0\Delta\phi_2 e^{1/2}|$ for the first and second bumps and are parametrized by the heights, β_1 and β_2 (we follow the parametrization from [Wainwright et al., 2014b]). The quantities $\Delta\phi_{1/2}$ are the widths of the bumps, σ is the shift of the second bump from the first one, and ϕ_0 specifies the location of the true vacuum. In general, we have five variables associated with the barriers; the width ($\Delta\phi_{1/2}$), the parametrized bump height ($\beta_{1/2}$) and the shift (σ). However, the instanton profile only depends on the first barrier shape (where the field tunnels through) as long as two bumps do not overlap. Therefore, in the AIP case where we are interested in the aftermath from different shapes of the instanton profile, we will fix the parameters associated with the second barrier. In the BIP case, to control the relative energy difference between V_B and $V_{\rm TP}$, the easiest way is to allow the second barrier parameters to vary alone while holding the overall instanton shape fixed.[1]

2.2.1 Preliminary for AIP

As mentioned in section 2.1, an instanton profile is one the most relevant factors to the outcome. In general, if we approximate an instanton profile as a step function, its properties can basically be captured by the initial bubble radius (R) and its field amplitude ($\phi_{\rm amp}$), the distance (in field space) between V_A and the instanton endpoint (see Fig. 2.3). These two quantities determine the shape of an instanton. In order to vary R and $\phi_{\rm amp}$, we need to know how an instanton profile behaves accordingly when the barrier shape is altered. The initial bubble radius (R) and the initial bubble separation (Δx), together determine the kinematics of bubble collisions. Although R is obtained by changing the potential configuration, in the case of studying the aftermath due to the kinematics factor, the potential shape is a secondary affect as we will see in section

[1] In this case, we are only investigating the energy difference between different vacua. Fixing the instanton profile guarantees that the value of V_A remain constant. Although we might not necessarily change the value of V_A while varying the instanton profile, it is in general hard to do.

3.2. The ϕ_{amp}, on the other hand, depends on the barrier shape along (the kinematics plays no role of determining the amplitude of an instanton profile).

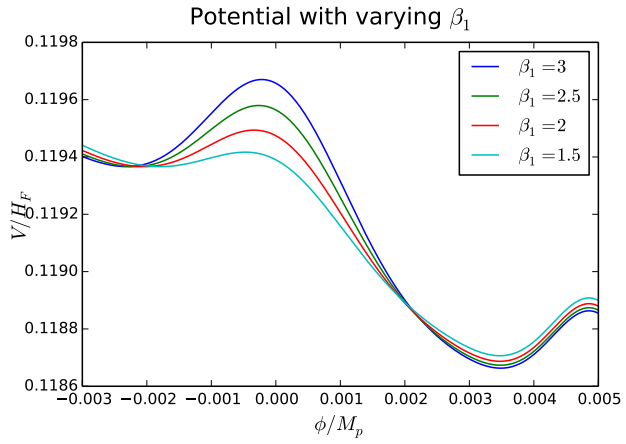

(A)

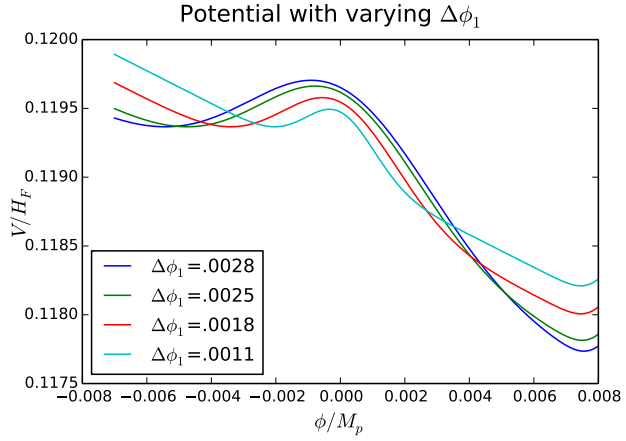

(B)

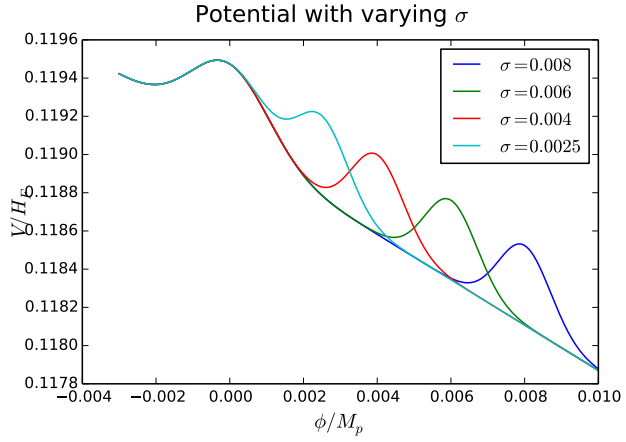

(C)

FIGURE 2.2: Potential for varying different parameters

In addition, as one can see from Fig. 2.3, it is impossible to change one parameter

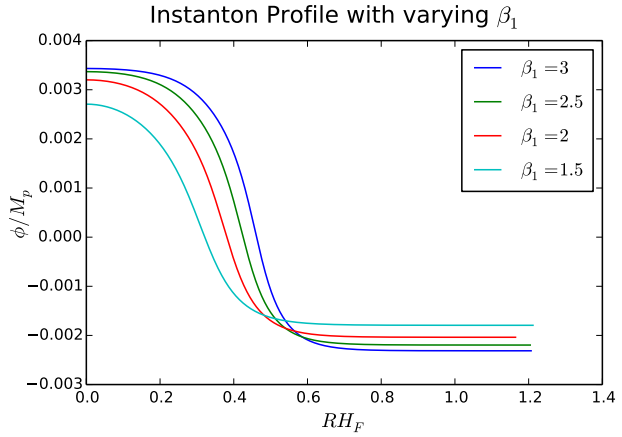

(A)

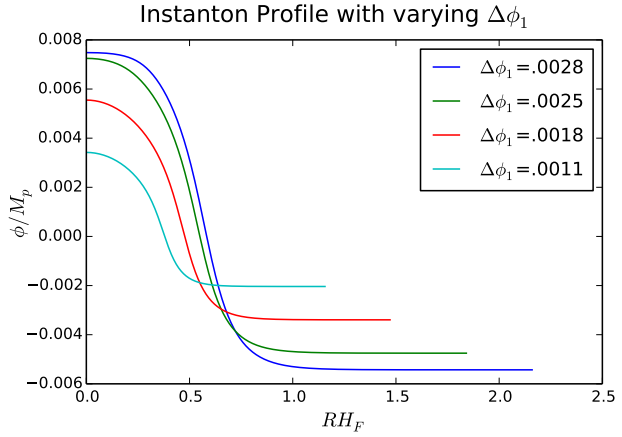

(B)

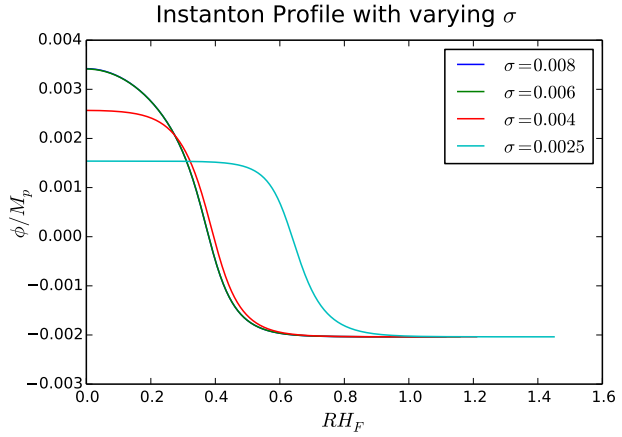

(C)

FIGURE 2.3: Instanton profiles with corresponding field potential in Fig. 2.2

associated with the barrier alone while varying parameters associated with the instanton profile individually. Nonetheless, if we allow two parameters associated with the barrier to vary simultaneously, we will be able to vary R and ϕ_{amp} independently (at least in some window). In what follows, we will use three degrees of freedom ($\Delta\phi_1$, β_1 and σ) in all possible combinations to vary R and ϕ_{amp} one at a time. In theory, we can pair $\Delta\phi_1$, β_1 and σ in three different combinations ($\Delta\phi_1 - \beta_1$, $\Delta\phi_1 - \sigma$ and $\beta_1 - \sigma$). In the constant R case, we do get a variety of distinct ϕ_{amp} for all combinations (Fig. A.1). However, in the constant ϕ_{amp} case, only $\Delta\phi_1 - \sigma$ and $\beta_1 - \sigma$ are managed to give distinguishable R (Fig. A.2). The window in the $\Delta\phi_1 - \beta_1$ sector is too narrow to show significant differences in ϕ_{amp}.

2.2.2 Preliminary for BIP

In the BIP case, (as our first step) we verify that when we alter β_2, the instanton profile remain unchanged (as long as two barriers do not overlap with each other, see Fig. A.3). Next, as we mentioned in section 1.3, we want to explore the properties of a marginal repulsive geometry that follows from the work in Ref. [Johnson and Yang, 2010]. We start by running the simulation for different β_2 using our second model. Indeed, we reproduce three distinct geometries of the domain walls (see Fig. 2.4). In these cases, the relative energy difference in the newly formed bubble (V_{TP}) and its surrounding vacuum energy (V_B) is the only relevant factor that gives rise of different geometries as studied 1.3. However, they need to satisfy a criteria in advance: $V_A > V_B$ (by default, the bubbles need to expand and then collide in the first place). The V_{TP} here is defined to be at the filed value with the first appearance of the space-like spatial slice (ϕ_{sp}). The choice of ϕ_{sp} is base on the fact that the coordinates inside the bubble is well defined and this indicates we have successfully created a new bubble universe.

In the case of a repulsive geometry, it was found that (in [Johnson and Yang, 2010]) V_B is always larger than V_{TP} and in a oscillatory geometry, V_B is always less than V_{TP} (but V_{TP} still need to be less than V_A). However, it is unclear for a marginal repulsive geometry at this point either V_B or V_{TP} is larger than one to the other and we will return to this analysis in a few sentences. Nevertheless, as we can see from Fig. 2.4, we do not get a marginal repulsive geometry for a domain wall after a classical transition for

arbitrary β_2. Luckily, this problem can be solved if we alter two parameters associated with the second barrier simultaneously. We therefore investigate two sectors ($\sigma - \beta_2$ and $\Delta\phi_2 - \beta_2$) that will produce a domain wall which possesses marginal repulsive geometry. Now, we will return to the question about the relative energy difference between V_B and $V_{\rm TP}$ in the marginal repulsive geometry. From a previous work of studying the domain wall geometry in[Johnson and Yang, 2010], it was found that there is an upper bound energy constraint for a repulsive geometry. We would like to know if there also exists an energy bound for a marginal repulsive geometry. We substitute the boundary constraint with a marginal repulsive geometry and found a lower bound for $V_{\rm TP}$,

$$V_{\rm TP} \geq \frac{(V_A + V_B)^2}{4V_A}. \tag{2.2}$$

Although this criteria gives an lower bound for $V_{\rm TP}$, it does not give an intuitive relation to V_B. Therefore, we define a new quantity

$$\delta \equiv V_{\rm TP} - V_B \tag{2.3}$$

and look for a constraint on δ from Eq. (2.2). By replacing $V_{\rm TP}$ in Eq. (2.2) with δ, we find

$$\delta \geq \frac{(V_A - V_B)^2}{4V_A}. \tag{2.4}$$

Since the RHS of Eq. (2.4) is positive definite, $V_{\rm TP}$ in a marginal repulsive geometry is always greater than V_B. In chapter 3, we will test this inequality in the parameter space that produces a marginal repulsive geometry of a domain wall and see if Eq. (2.4) holds for all circumstances.

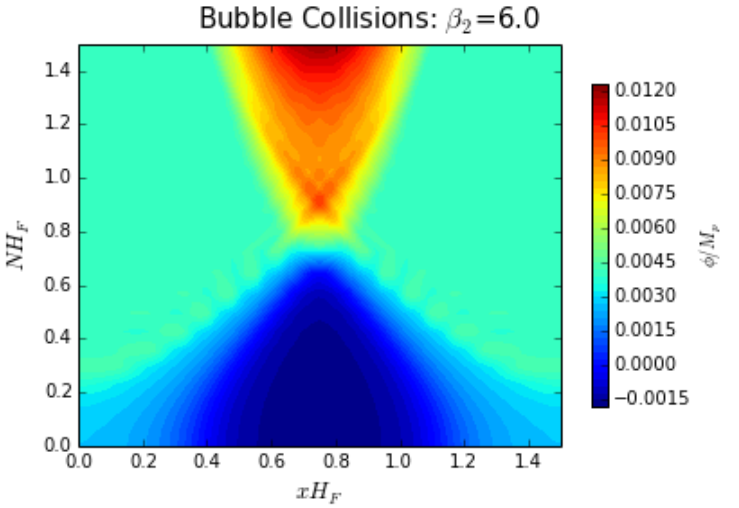

(A)

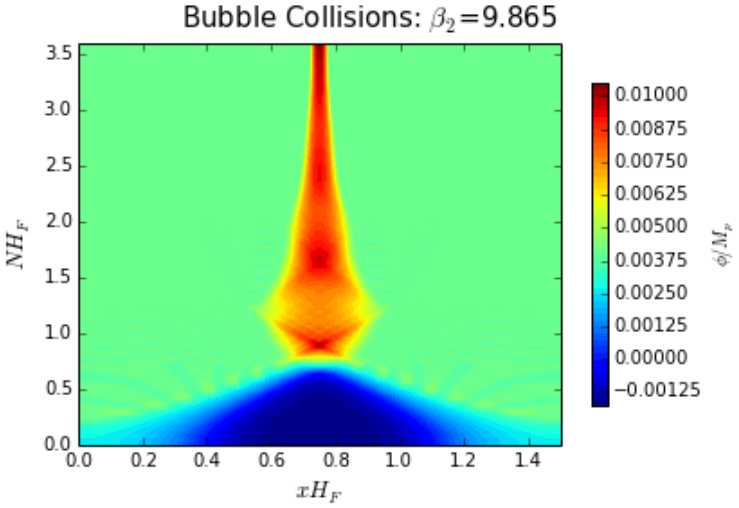

(B)

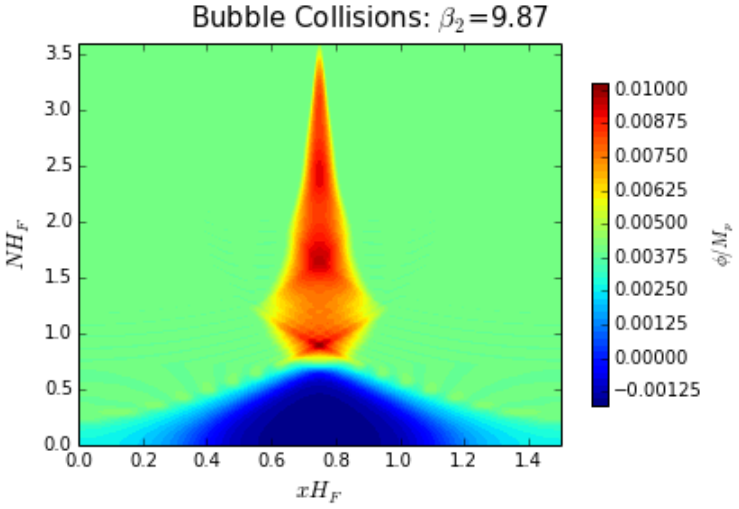

(C)

FIGURE 2.4: Bubble collison simulations for various β_2. (A) *Repulsive* (B) *Marginal Repulsive* (C) *Oscillatory* geometries

Chapter 3

Simulation Results and Analysis

In this chapter, we will first highlight some of our main results on the prediction for the CMB quadrupole moment due to the primordial perturbation of a bubble collision. Since the collision will potentially distort the geometry of the bubble, it is possible that different regions inside the bubble will expand differently. This essentially affects the locally observed curvature. Although the geometry of the bubble is ill-defined, it is possible to approximate (locally) different patches of the bubble as a perturbed opened FRW metric from the residual $SO(2)$ symmetry of spacetime as mentioned in chapter 1. This allows us to make a connection between the scale factor and the perturbation. Since the metric is defined locally, making predictions of a quadrupole moment (which is related the comoving curvature perturbation as we will see in section 3.1) at different regions alone is meaningless unless we specify the local curvature (this is related to the scale factor as shown in Eq. (1.31) associated with it. In what follows, we will show a correlation between the quadrupole moment and the local curvature (see section 3.2). Furthermore, we will explore different trends in different model as we vary the parameters associated with the instanton profiles (for the first model) and the value of the V_B for the second model (see section 3.3). Lastly, we survey the classical transition boundary in the first model. This is motivated by the lumpiness feature (as we will see in a few lines) arises during the analysis of the $\beta_1 - \Delta\phi_1$ sector as well as comparing a quadratic potential with polynomials of higher order (see section 3.4).

3.1 CMB Quadrupole Moment

In chapter 1, we found the dominant contribution of the comoving curvature perturbation to be the quadratic term in a Taylor series expansion. To compare our results with the CMB data, we must relate the temperature fluctuations to the comoving curvature perturbation. Specifically, the bubble results from a classical transition covers the entire bubble. We expect this will affect primarily to the lowest mode of the CMB power spectrum ($l = 2$). As we will see in a few lines, the $l = 2$ mode is proportional to the quadratic term in the expansion of the comoving curvature perturbation. We begin by taking the Sachs Wolfe limit in which the temperature fluctuation can be approximated as[Sachs and Wolfe]

$$\frac{\Delta T}{T} = \frac{\mathcal{R}(\xi - \xi_0)}{5}. \tag{3.1}$$

Using Eq. (1.15), Eq. (3.1) reduces to

$$\frac{\Delta T}{T} \approx \frac{1}{5}\left[\frac{1}{2}\mathcal{R}''(\xi_0)(\xi - \xi_0)^2 + \mathcal{O}(h)\right]. \tag{3.2}$$

On the other hand, the temperature fluctuation at the same time be decomposed as a linear combination of a complete set of multipole moments,

$$\frac{\Delta T}{T} = \sum_l \sum_m a_{lm} Y_{lm}, \tag{3.3}$$

where

$$a_{lm} = \int_\Omega \frac{\Delta T}{T} Y^*_{lm} d\Omega. \tag{3.4}$$

In Eq. (3.3) and Eq. (3.4), Y_{lm} are the spherical harmonics, and the power spectrum, C_l, is then defined as

$$< a_{lm} a_{l'm'} >= \delta_{ll'}\delta_{mm'} C_l. \tag{3.5}$$

Since the observers at an arbitrary location do not have access to the entire universe (due to causality), we need to restrict the observers with a causal boundary. For our Universe, we only have access to the events happen after photons decouple. Therefore, we evaluate Eq. (3.2) at the point in which the past light cone intersects the surface of

last scattering (ls),

$$\left.\frac{\Delta T}{T}\right|_{\xi=\xi_{ls}} \approx \frac{1}{5}\left[\frac{1}{2}\mathcal{R}''(\xi_0)(\xi_{ls}-\xi_0)^2+\mathcal{O}(h)\right]. \tag{3.6}$$

In the limit where $X \approx \xi_{ls}-\xi_0 \approx R_{ls}\cos\theta$ (with θ being the viewing angle), Eq. (3.6) becomes

$$\left.\frac{\Delta T}{T}\right|_{R_{ls}} \approx \frac{1}{5}\frac{1}{2}\mathcal{R}''(\xi_0)R_{ls}^2\cos^2\theta. \tag{3.7}$$

By comparing Eq. (3.7) and Eq. (3.4), we identify the quadratic term in Eq. (3.7) corresponds to $l=2$ and $l=0$ modes of the spherical harmonics Y_{2m} and Y_{00}. This is exactly what we are looking for. Furthermore, due to an azimuthal symmetry in $\mathcal{R}$, we can pick $m=0$ to simplify the algebra. After combining Eq. (3.7) and Eq. (3.4), we get

$$\left.\frac{\Delta T}{T}\right|_{R_{ls}} \approx \frac{1}{15}\sqrt{\frac{4\pi}{5}}\mathcal{R}''(\xi_0)R_{ls}^2Y_{20}. \tag{3.8}$$

One quantity yet to be specified is the radius at the last scattering. This is related to the local curvature by[Aguirre and Johnson, 2009]

$$R_{ls} = 2\sqrt{\Omega_k} \tag{3.9}$$

where Ω_k is the energy density fraction of the local curvature today. In different regions of the bubble, there is a potential variation in local curvature caused by the collision. The curvature for observers at different location is related to the local expansion rate by

$$\Omega_k(\xi_0) = \Omega_k(0)\frac{a_0^2(0)}{a_0^2(\xi_0)}, \tag{3.10}$$

where we have picked $\xi_0=0$ to be our reference point. By combining Eq. (3.10) and Eq. (3.8) together with the definition of power spectrum in Eq. (3.5), we obtain the CMB quadrupole power spectrum, C_2 as

$$C_2 = \frac{16}{225}\frac{4\pi}{5}\mathcal{R}''(\xi_0)^2\Omega_k(0)^2\frac{a_0^4(\xi_0)}{a_0^4(0)}. \tag{3.11}$$

The CMB power spectrum is usually expressed in $\mathcal{D}_l$ instead of C_l, where $\mathcal{D}_l$ is defined as[Planck et al., 2015]

$$\mathcal{D}_l = \frac{l(l+1)C_l}{2\pi}[\mu K^2]. \tag{3.12}$$

The present constraint on the local curvature is $\Omega_k = 0.000 \pm 0.005$ [Planck et al.,

2015]. This gives an upper bound of $\Omega_0 = 0.005$, and we will use it as our reference, $\Omega_k(0) = \Omega_0$. In addition, the present theoretical prediction on the CMB quadrupole moment is $\mathcal{D}_2 \approx 1100[\mu K^2]$. In what follows, we will show our results in terms of the reference free quadrupole moment, $\mathcal{D}_2/\Omega_0^2$ (this gives a clearer picture of $\mathcal{D}_2$ since the reference, Ω_0, can be chosen by any observer arbitrarily.)

3.2 Simulation Predictions for $\mathcal{D}_2$ and Ω_k

In this section, we show our prediction of $\mathcal{D}_2$ and Ω_k according to the simulation. In the first part, we devote our discussion to the the first model in which we can categorize the effect to the post-collision signature by **(1)** the kinematics and **(2)** the potential shape. In the kinematics factor case, we show that (see Fig. 3.1) the signature agrees with Eq. (1.11). For a larger/smaller initial bubble separation/radii, we obtain a greater value of quadrupole moment. In addition, according to the simulation, we found that the threshold energy in this particular case is $\gamma = 3.7$ provided that the initial bubble separation $\Delta x = 0.9$. Conversely, in the potential shape factor case (3.2), different field amplitudes (while holding the initial bubble radius the same) is unclear at this point if the signature has a particular trend and we will leave the discussion to the next section. Nevertheless, it also produces a signature that is compatible with the one due to the kinematics factor and the maximum signature is observed at the bubble center.

In all of the $\mathcal{D}_2$ plots we have produced, the noise starts to build up as the simulation approaches the edges, and the plots only show the regime in which the simulation results are trusted. In order to distinguish the noise from the real signature produced by the simulation, we reran the simulation with increasing the resolution. In each consecutive run, we found that the new signature does not produce the same wiggles and the the point at which the noise starts to build up has been pushed towards the edges. By comparing results at different resolutions, we see a trend of vanishing perturbation near the edges and the cut-off of these plots are determined by which the noise is indistinguishable between different resolutions.

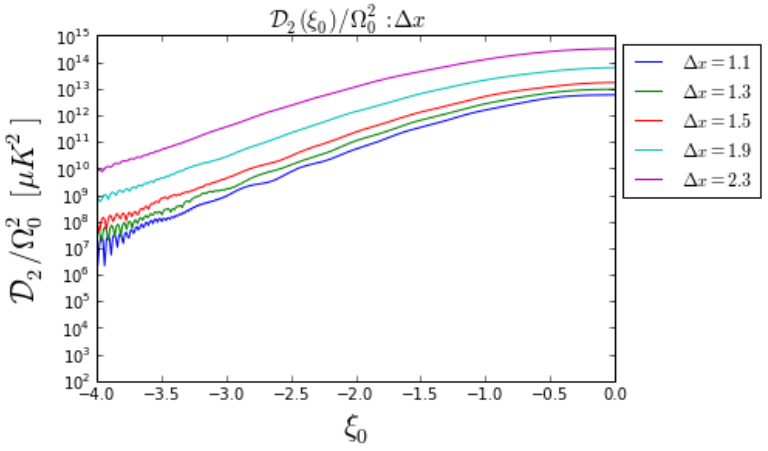

(A)

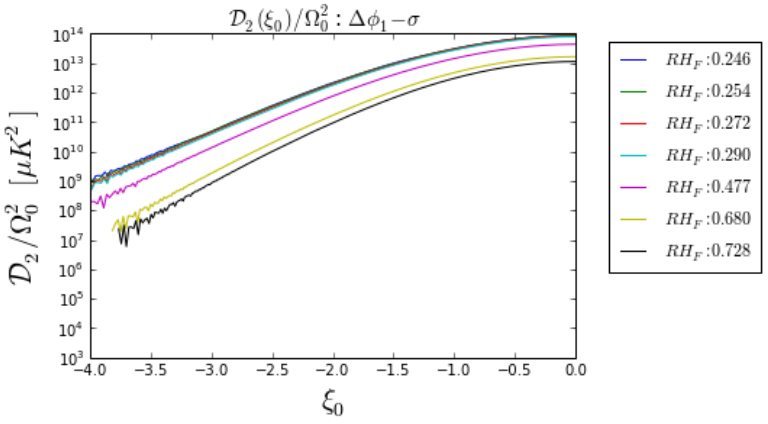

(B)

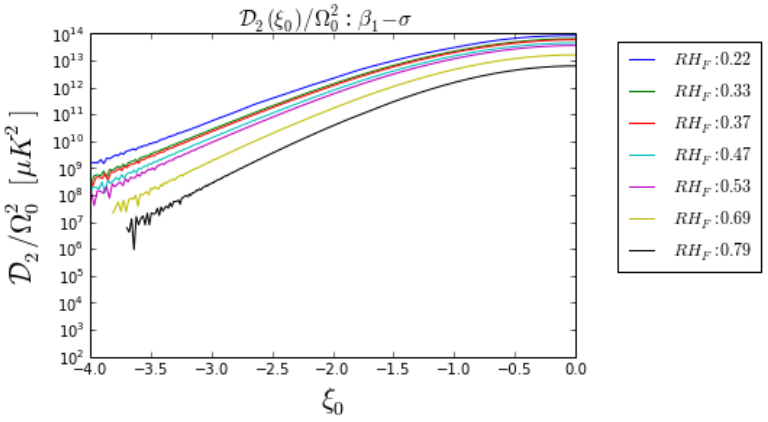

(C)

FIGURE 3.1: $\mathcal{D}_2$ predicted by the simulation for the kinematics factor. (A) indicates different initial separation, (B) and (C) for different initial radii in two different sectors for the first model.

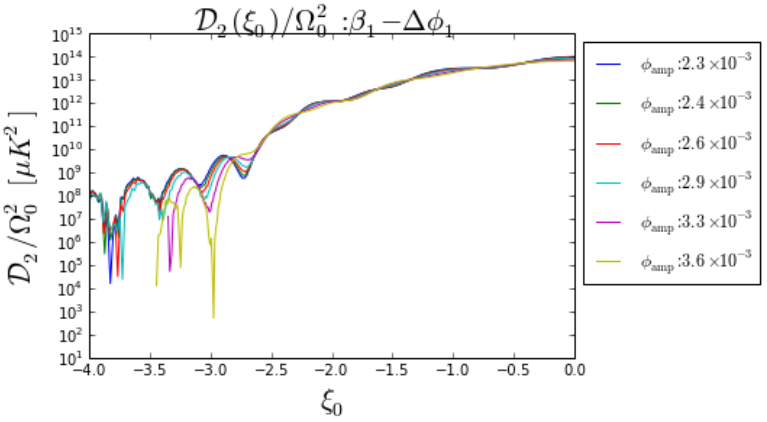

(A)

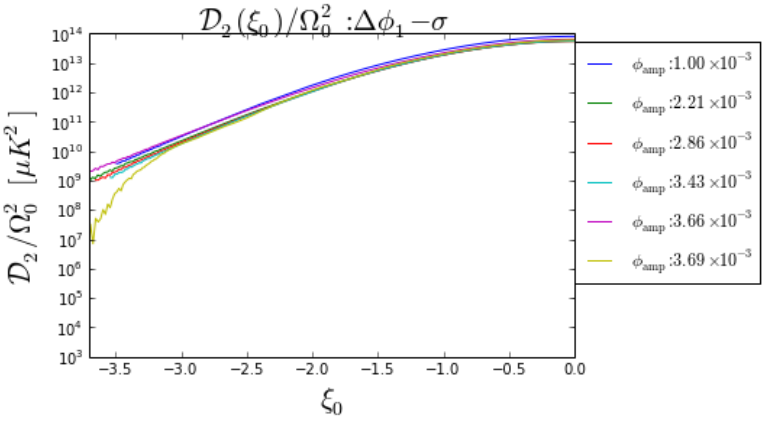

(B)

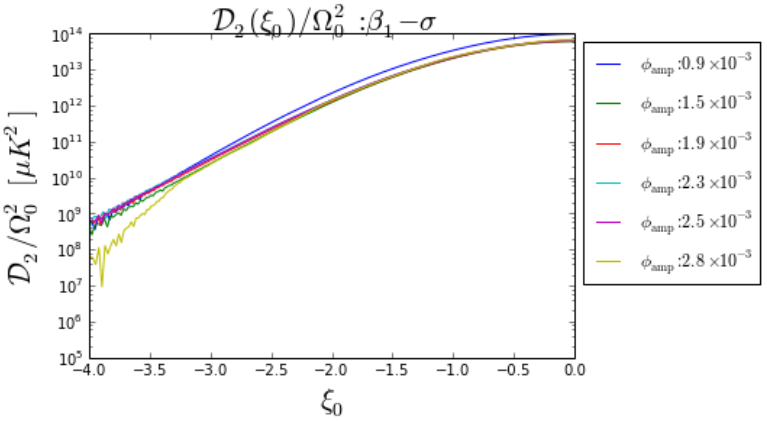

(C)

FIGURE 3.2: $\mathcal{D}_2$ predicted by the simulation for the potential shape factor. (A), (B) and (C) indicate different ϕ_{amp} in three different sectors for the first model

In the second model (see Fig. 3.3), we predict the value of the quadruple moment that is at least order six to ten magnitude larger than the observed CMB quadrupole moment. In these plots, we see a trend in both $\sigma/\Delta\phi_2 - \beta_2$ sectors where the position of the first space-like constant field spatial slice ($\phi_{\rm sp}$ from low to high) is proportional to the CMB anisotropy. This is counter-intuitive and the argument is as follow. Since $\phi_{\rm sp}$ implies that the field will eventually rolls to V_C in region III as depicted in Fig. 2.1. Therefore, we are guaranteed that a newly formed bubble will not collapse. In this sense, if a bubble has a smaller $\phi_{\rm sp}$, this indicates that the bubble should exit the transient phase and enter the inflationary phase sooner than the one formed at a larger $\phi_{\rm sp}$. When the bubble starts to inflate, the perturbation freezes in (at least within a short amount of time). Therefore, in theory, a smaller $\phi_{\rm sp}$ should give a greater observed signature at late time. However, from Fig. 3.3, we see exactly the opposite; for a smaller $\phi_{\rm sp}$, the resulting perturbation is smaller. Therefore, it is unclear at this point if ϕ_{sp} is a good indication to categorise the trend that we observe. In other words, does ϕ_{sp} truly represent the starting point of inflation? We will loop back and discuss this observation in the next section.

Moreover, in the $\mathcal{D}_2$ plots, we give a reference free prediction to the value of $\mathcal{D}_2$. Namely, the exact value of $\mathcal{D}_2$ is based on the measurement of the local spatial geometries, Ω_0 as well as the observer's position in the universe. Since the current measurement on local spatial curvature, $\Omega_0 = 0.000 \pm 0.005$, includes all possible spatial curvatures, positive, zero or negative (within the error bar), we cannot conclude if this agrees with our prediction at this point. Nonetheless (as an example of how we can proceed if the future experiment is sensitive enough), if we assume local curvature is at its upper bound, $\Omega_0 = 0.005$, and as measured by an observer at the center of the bubble, the prediction on the quadrupole moment gives a lower bounds, $\mathcal{D}_2/\Omega_0 \approx 10^7 \mu K^2$. In this situation, the first model is still a plausible description of our Universe; whereas, the second model is ruled out. However, if the future experiment indicates that the spatial curvature is zero within an error of 10^5 (the same order as the CMB temperature fluctuation), the signature predicted by both models is consistent with no bubble collision and the detectability of bubble collision signature is not achievable.

For different observers, we show that (in Eq. (3.10)) there is a variation in the local curvature at different location due to a bubble collision. In the first model, we see that (from Fig. 3.4 and Fig. 3.5) the variation in the local curvature is small (an order one

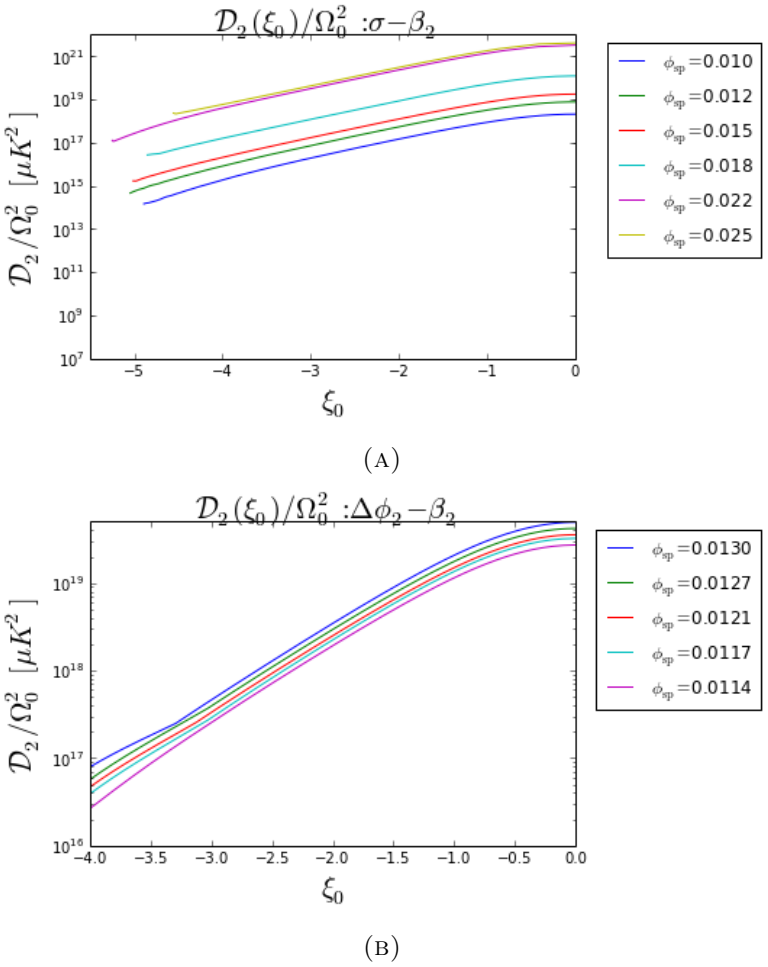

FIGURE 3.3: $\mathcal{D}_2$ prediction for the second model. Two plots are subjected to the Marginal Repulsive geometry of the domain walls after a classical transition studied in (A) $\sigma - \beta_2$ and (B) $\Delta\phi_2 - \beta_2$ sectors

magnitude difference) as an comparison to the second model. In the second model, the local curvature (in Fig. 3.6) changes by three orders of magnitude near the edges. This indicates that at the edge of the bubble (in the BIP case), the scale factor remains the same. Thus, the bubble is stationary (not inflating) near the edges. In addition, we have normalized the local spatial curvature to one for an observer at the center of the bubble. This reference choice of normalization can be chosen arbitrarily by observers at other locations. We made this choice is because the relative magnitude of the local spatial curvature is minimized at the bubble center, and the value of $\mathcal{D}_2$ will therefore be maximized.

As argued in chapter 1, the local geometry is determined by the local expansion rate, a, and perturbation, $\mathcal{R}$. These two quantities in terms of observables are Ω_k and $\mathcal{D}_2$. Hence, we show the correlation between $\mathcal{D}_2$ and Ω_k from Fig. 3.7 to Fig. 3.9.

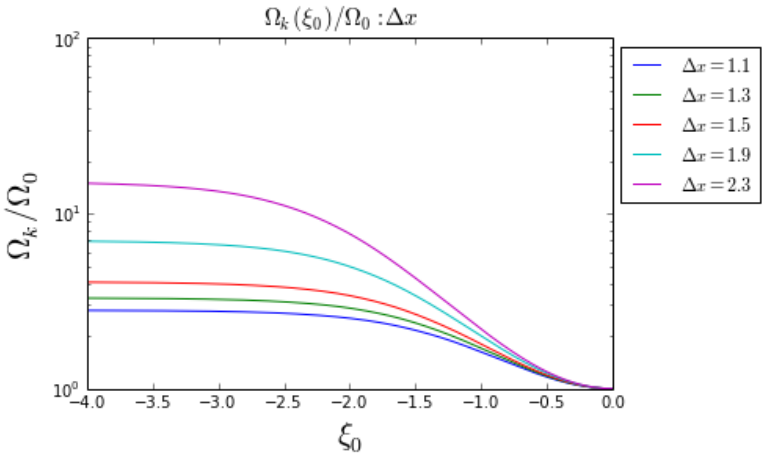

(A)

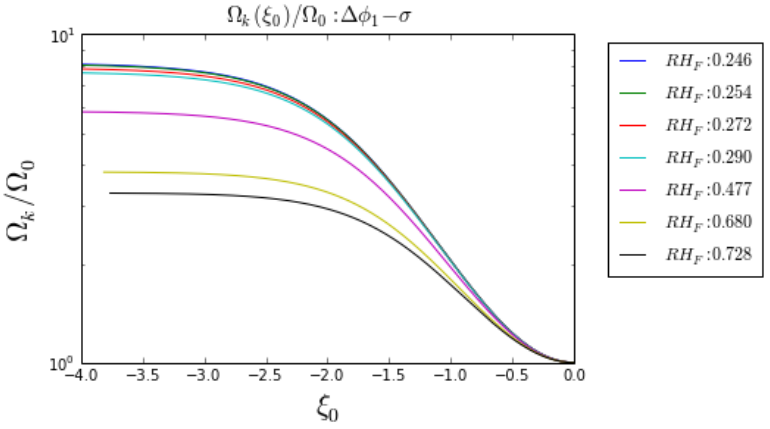

(B)

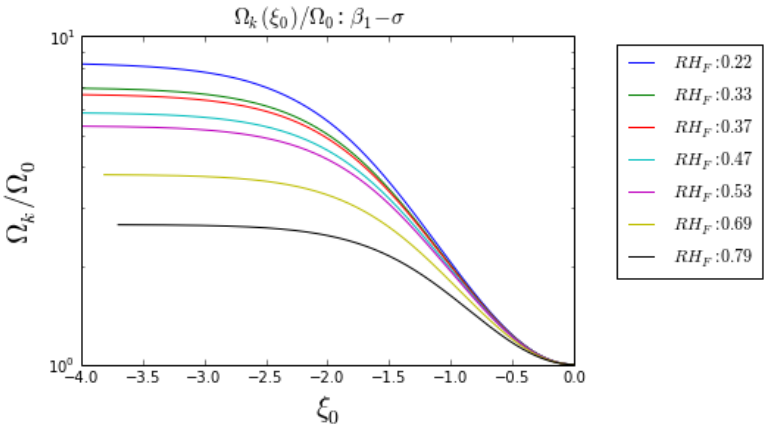

(C)

FIGURE 3.4: Ω_k predicted by the simulation for the kinematics factor. (A) indicates different initial separation, (B) and (C) for different initial radii in two different sectors for the first model.

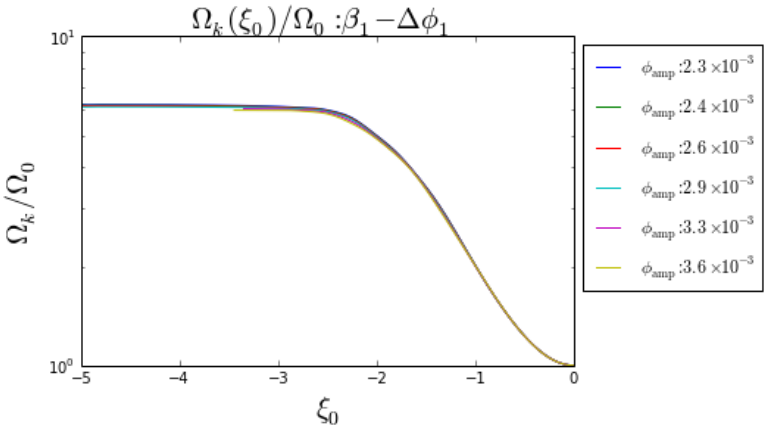

(A)

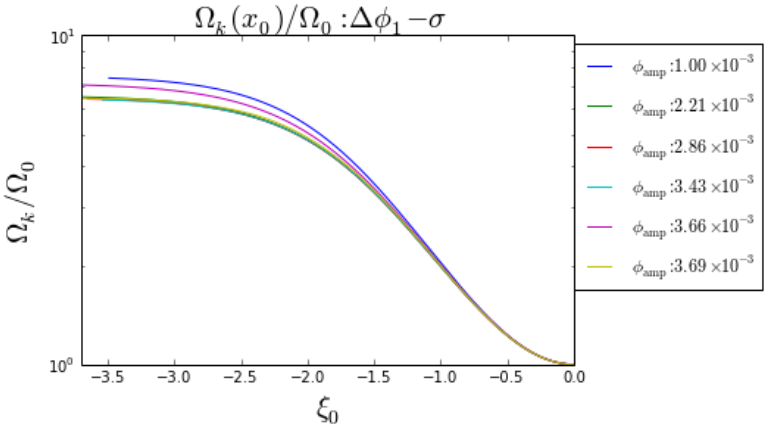

(B)

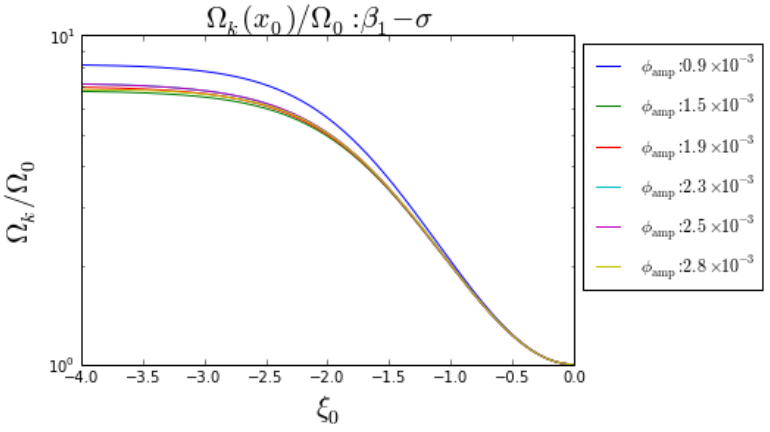

(C)

FIGURE 3.5: Ω_k predicted by the simulation for the potential shape factor. (A), (B) and (C) indicate different ϕ_{amp} in three different sectors for the first model

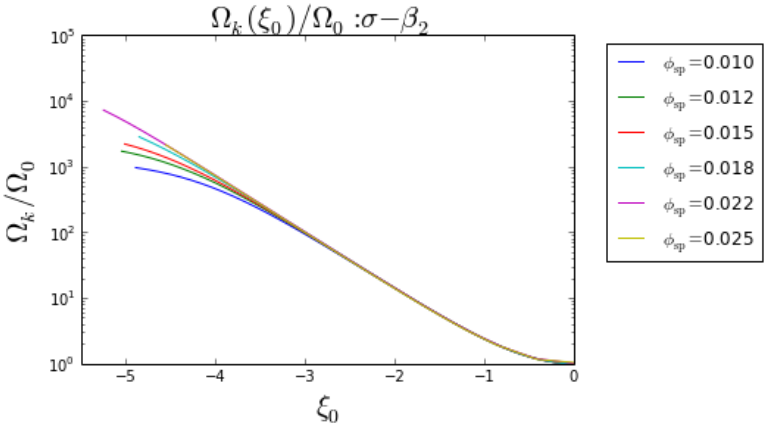

(A)

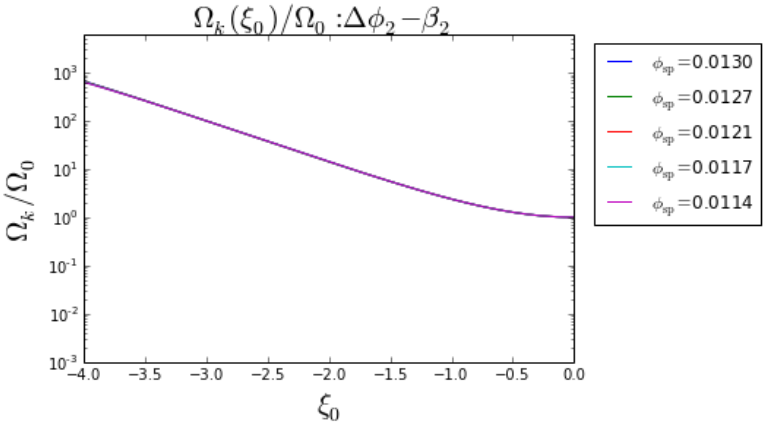

(B)

FIGURE 3.6: Ω_k prediction for the second model. Two plots are subjected to the Marginal Repulsive geometry of the domain walls after a classical transition studied in (A) $\sigma - \beta_2$ and (B) $\Delta\phi_2 - \beta_2$ sectors

3.3 Trends in Different Models

So far, we present the results of the CMB quadrupole moment and the associated local curvature from $\mathcal{R}''$ and a based on the simulations. The profile of $\mathcal{R}''$ and a are similar to the $\mathcal{D}_2$ and Ω_k as shown in the previous sections. Thus, we will leave the readers who is interested in these profiles to see Appendix B. In the remaining chapter, we will explore features in different models.

In the first model, we showed that the kinematics factor (various R and Δx) and the resulting perturbation are proportional to each other as shown in section 3.2. To explore if a specific trend in the resulting perturbation follow from different parameters, we extract the maximum in each $\mathcal{R}''$ profile (where it turns out to be at the center of

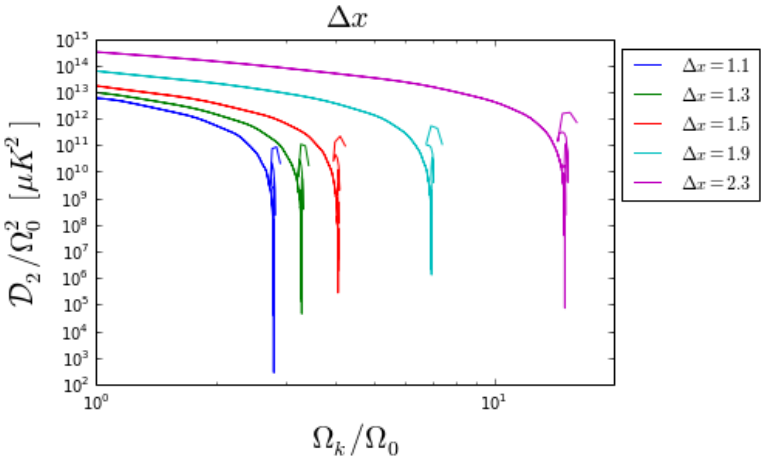

(A)

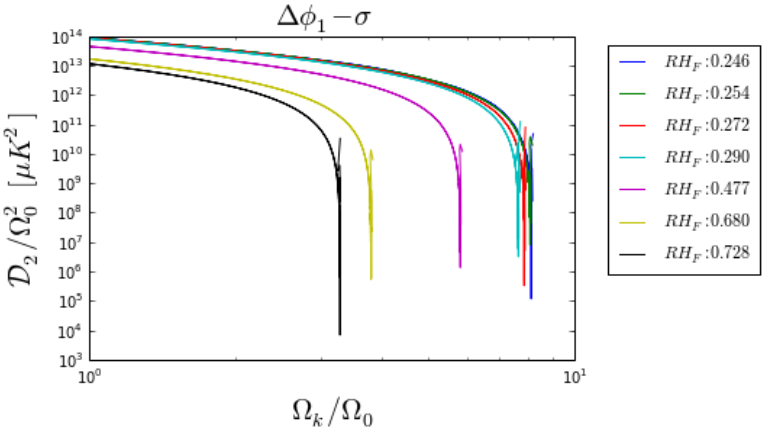

(B)

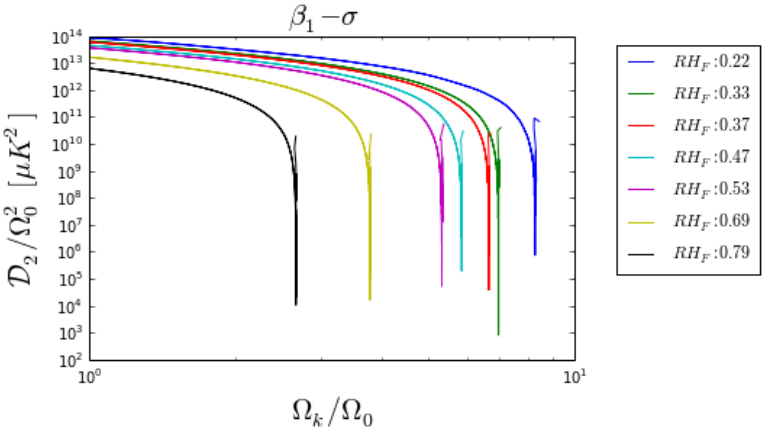

(C)

FIGURE 3.7: Correlation between $\mathcal{D}_2$ and Ω_k for the kinematics factor. (A) indicates different initial separation, (B) and (C) for different initial radii in two different sectors for the first model.

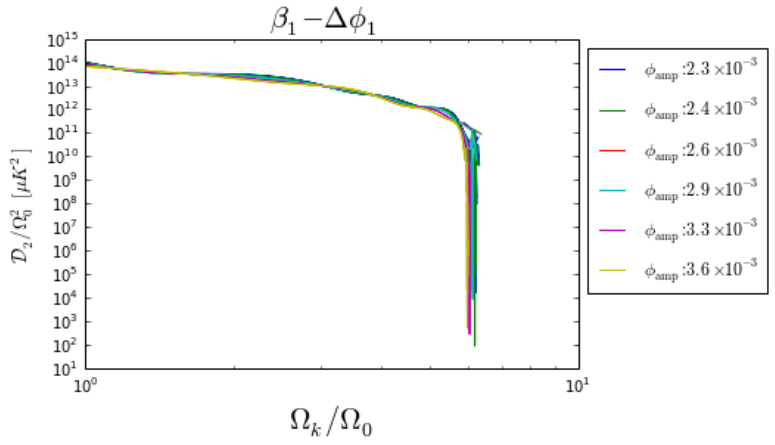

(A)

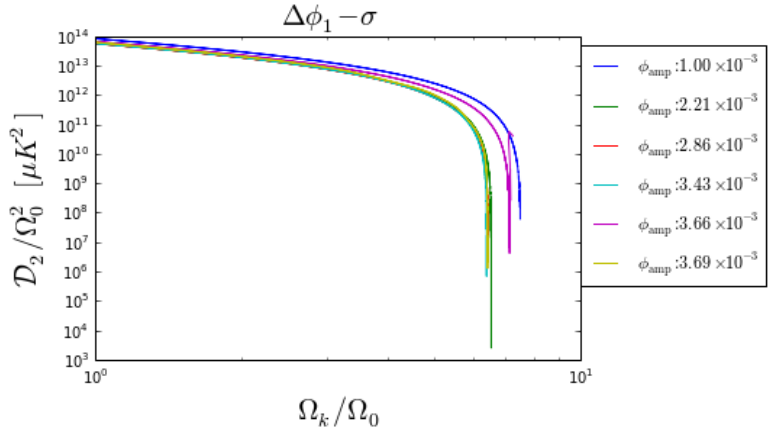

(B)

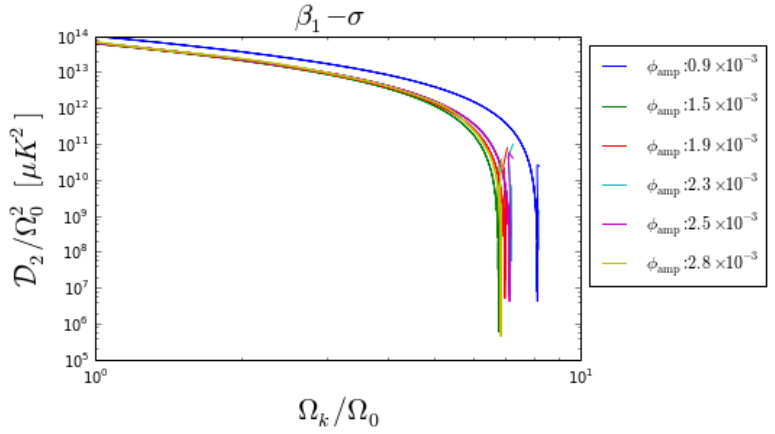

(C)

FIGURE 3.8: Correlation between $\mathcal{D}_2$ and Ω_k for the potential shape factor. (A), (B) and (C) indicate different ϕ_{amp} in three different sectors for the first model

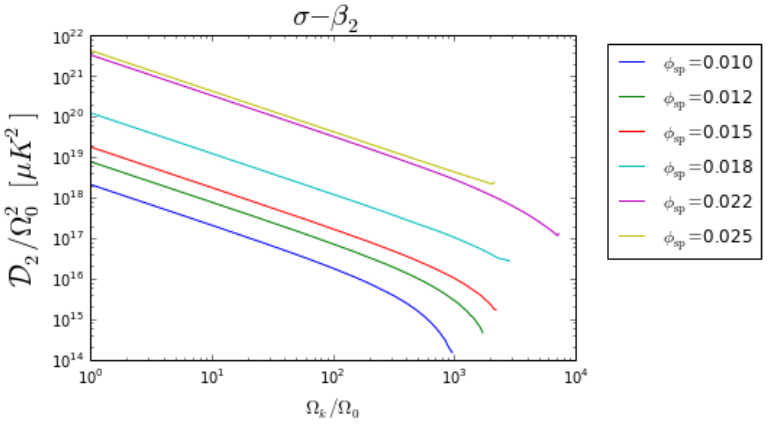

(A)

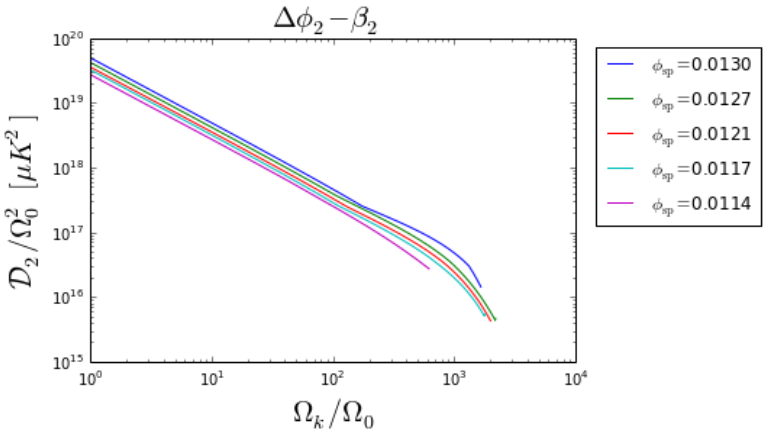

(B)

FIGURE 3.9: Correlation between $\mathcal{D}_2$ and Ω_k for the second model. Two plots are subjected to the Marginal Repulsive geometry of the domain walls after a classical transition studied in (A) $\sigma - \beta_2$ and (B) $\Delta\phi_2 - \beta_2$ sectors

the bubble $\xi_0 = 0$). In the kinematics factor, we show that the perturbation linearly increases as the initial bubble radii decreases (see Fig. 3.10a). Note that we obtained different radii by changing $\Delta\phi_1/\beta_1 - \sigma$ in the first barrier and we still get a linear trend. As we will explain in the next few lines, when we vary the same parameter associated with the potential we do not get the same linear trend for various ϕ_{amp}. This shows that the initial bubble radius is more a kinematics factor over a potential shape factor. This is because when σ is small, essentially, two barriers start to interfere, thus, the overall shape of an instanton profile are distorted. As a result, it is hard justify if a specific trend follows (in different ϕ_{amp}) as the bumps start overlapping with each other. On the other hand, we do get a linear trend in the $\beta_1 - \Delta\phi_1$ sector (where we have chosen σ to be large enough to prevent the bumps from overlapping.) As we can see, for a smaller ϕ_{amp}, the simulation shows a greater perturbation. To understand this, one realizes

the distance of which the instanton can travel (after a classical transition) comes from three contributions. The first effect comes from the distance (in field space) between V_A and the instanton endpoint (approximately proportional to $\Delta\phi_1$). Second, the slow roll phase between the first and the second barriers (distance between after which the instanton tunnels through and the position of V_B). Third, the second bump where the field hops over. The second contribution is an irrelevant factor for different $\phi_{\rm amp}$ since as the field rolls down on the same potential, the amplitude of the solitons growth identically for all cases of $\phi_{\rm amp}$. The third contribution is the most relevant factor; whereas, the first contribution provides an indirect connection as we will explain in the next couple lines. We will start by explaining the third contribution. Technically, how far the field is displaced after a collision can only be done via simulating two colliding incoming solitons without any approximation. However, it is possible to understand this picture with the free passage approximation[Giblin et al., 2010]. At the collision point, the bubble is occupied by the false vacuum energy V_B in which the field at that point is denoted by ϕ_B. Outside the bubbles, the parent false vacuum, V_A, should have a field value ϕ_A. Since we are colliding two identical bubble and both of them are occupied by the same vacuum state and thus takes the same field value ϕ_B, the amount ($\delta\phi_{kick}$) in which the field is displaced (or kicked) according to the free passage approximation is

$$\delta\phi_{kick} = 2(\phi_B - \phi_A). \tag{3.13}$$

Note that the field position of V_B is identical for all cases of $\phi_{\rm amp}$ since we fix the location of the false vacuum at ϕ_B. In order to maximize $\delta\phi_{kick}$, we need to minimize ϕ_A. This is where the first contribution comes in. Since the only controlled variable here is the initial $\phi_{\rm amp}$ of the instanton. As the amplitude increases, it pushes the false vacuum position towards a more negative field value (ϕ_A decrease). This results in a greater kick in $\delta\phi_{kick}$ and thus the instanton can travel further. This implies that the bubble enters the slow roll inflationary phase at a larger field value. Therefore, the bubble spends more time during non-inflating regime in which during this period, the perturbation is still on a sub-horizon scales and will decay more.

In addition, we show a plot associated with the scale factor. Similarly, we only see a particular trend in the $\beta_1 - \Delta\phi_1$ sector (for the potential shape factor) and in the various initial bubble radii case. However, when we compare Fig. 3.11 and Fig. 3.10, we see that

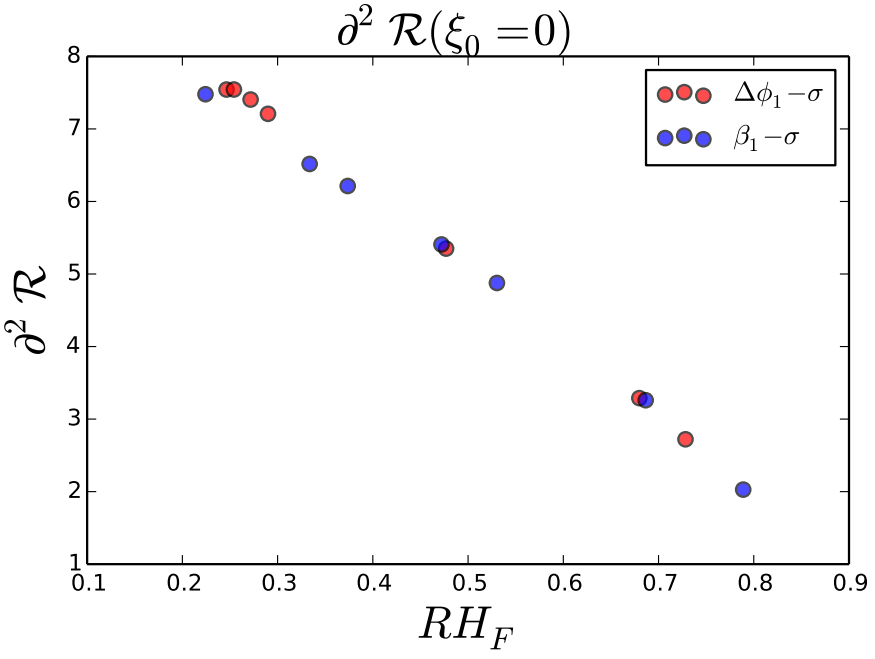

(A)

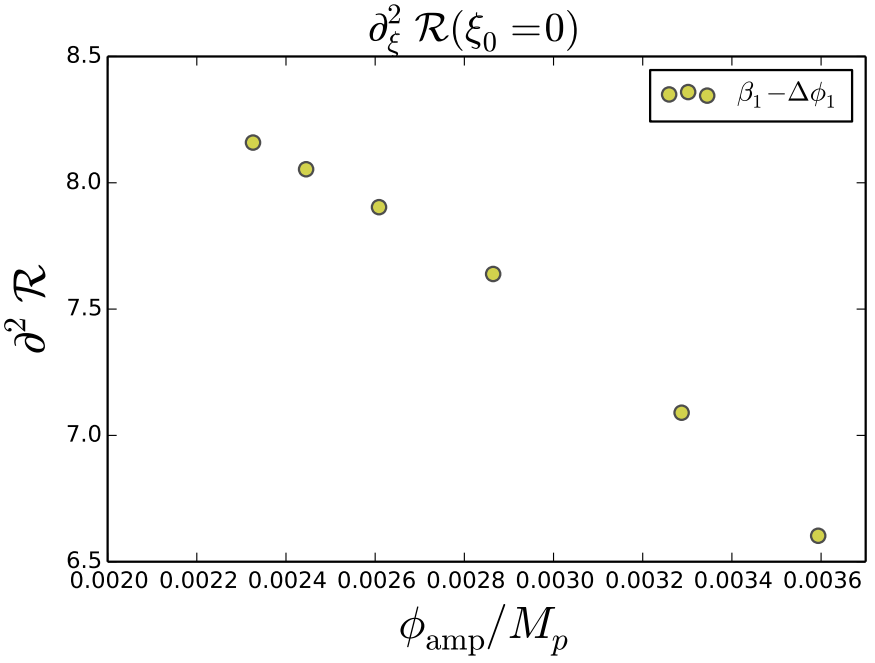

(B)

FIGURE 3.10: Scatter plots for $\partial_\xi^2 \mathcal{R}$ for observer at $\xi_0 = 0$ with constant $RH_F = 0.356$: (A) $\Delta\phi_1/\beta - \sigma$ and (B) $\Delta\phi_1 - \beta$ sectors.

for a larger perturbation, it always corresponds to a larger scale factor. This is because a larger expansion rate leads the bubble universe enters the super-horizon scales faster. This makes $\mathcal{R}$ freeze in sooner.

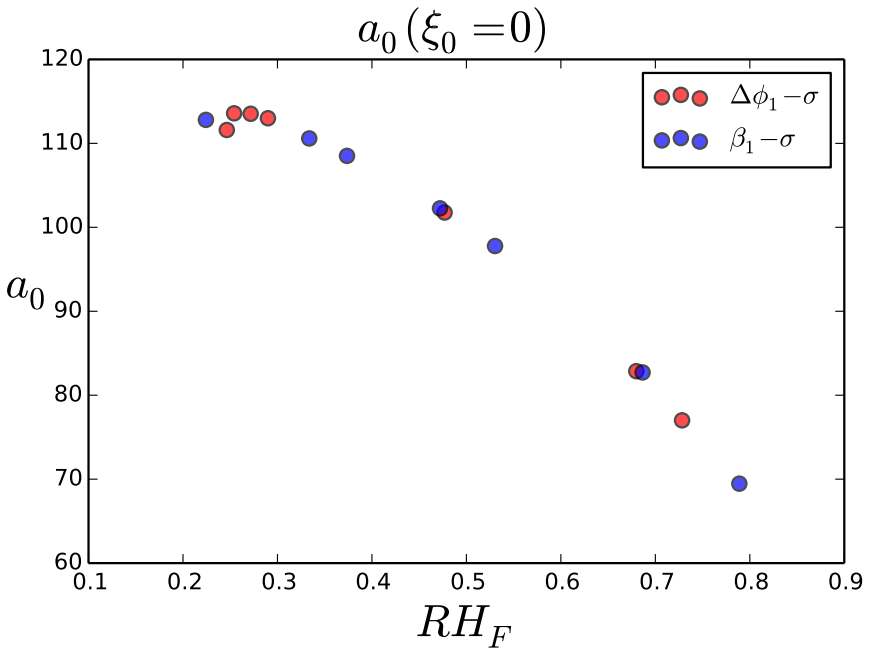

(A)

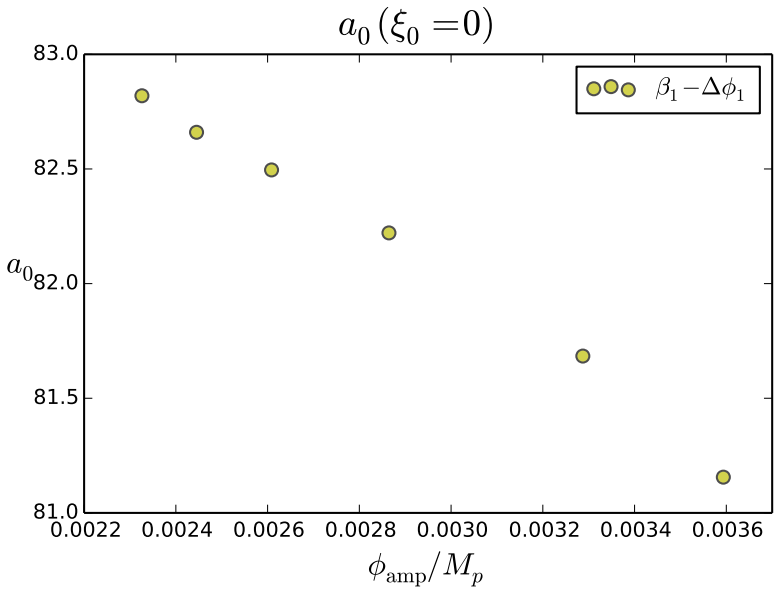

(B)

FIGURE 3.11: Scatter plots for a_0 with observer at $\xi_0 = 0$ with constant R in sector (A) $\Delta\phi_1 - \sigma$ and $\beta_1 - \sigma$ (B)$\Delta\phi_1 - \beta_1$.

In the second model, as we predicted in Eq. (2.4), $V_{\rm TP}$ is always greater than V_B in a marginal repulsive geometry of the domain wall. We verify this by finding the first

appearance of a space-like spatial slice (ϕ_{sp}) for each case and the potential energy at that field value defines $V_{\rm TP}$. From Fig. 3.12, we see that each ϕ_{sp} (in stars) that corresponds to a $V_{\rm TP}$ lies above V_B and satisfy the marginal repulsive geometry constraint in Eq. (2.3) (in diamonds) where we have defined $\delta V_{\rm bound} \equiv V_{\rm TP} - (V_A + V_B)^2/4V_A$. Since in all cases we studied, $V_{\rm TP} > V_B$, we expect a contracting phase in the post-collision behaviour (see Fig. 3.13). Besides a contracting phase, we also observe a field oscillatory period before the field enters the inflationary phase. This is due to the field get dragged towards different vacua in between $V_{\rm TP}$ and V_B. In a marginal repulsive geometry, we know a classical transition is guaranteed to happen, the field will eventually get affected by $V_{\rm TP}$ more than V_B and enter the inflationary phase. As a contrast to the marginal geometry, in an oscillatory geometry of a domain wall, this oscillatory behaviours of field also appears. However, in this case, the bubble is doomed to collapse and the field will eventually return to the false vacuum state, V_B. Nonetheless, we indicate the bounds for this oscillatory range of a marginal repulsive geometry case (in the light filled circles). A clearer behaviour can be seen from Fig. 3.14.

To explain the trend observed in Fig. 3.3, we take a constant slice through the bubble center at $\xi_0 = 0$. Fig. 3.14 shows this slice for the two different sectors. The plots begin at the collision point and the stars indicate the first appearance of a space-like spatial slice (ϕ_{sp}). In both plots, we see crossing points between lines in the vicinity of ϕ_{sp}. Instead of ϕ_{sp}, the crossing point is a more relevant indication at which the perturbation starts entering the inflationary phase (or super-horizon scales). This is because, from the plots, the curves approach to a steady state (different curves shows the field increase at a steady rate) after the crossing occurs. This implies that the field is in the regime of inflation and the scale factor starts growing exponentially. At some later time (depends on how scale factors grow in different cases), we know that the one with a larger expansion rate freezes in faster (as argued in the previous paragraph). To show which curves results a larger expansion rate, one needs to find out at which value the perturbation freezes in. We contrast two sectors and show that (in Fig. 3.15 and Fig. 3.16) the frozen point for all curves in the $\sigma - \beta_2$ is around $\phi \approx 0.037 M_p$, and $\phi \approx 0.033 M_p$ for the $\Delta\phi_2 - \beta_2$ sector. At these points, we realize in the $\sigma - \beta_2$ sector for example, it takes a shorter time for the blue curve to reach the same field value compare to the yellow curve (from Fig. 3.14, and any curve in between has the same pattern).

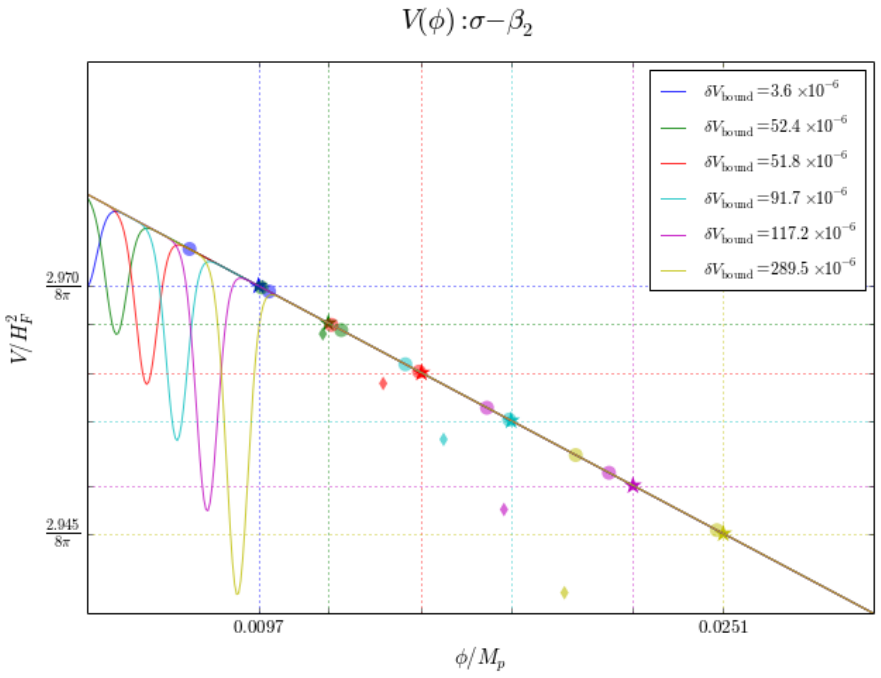

(A)

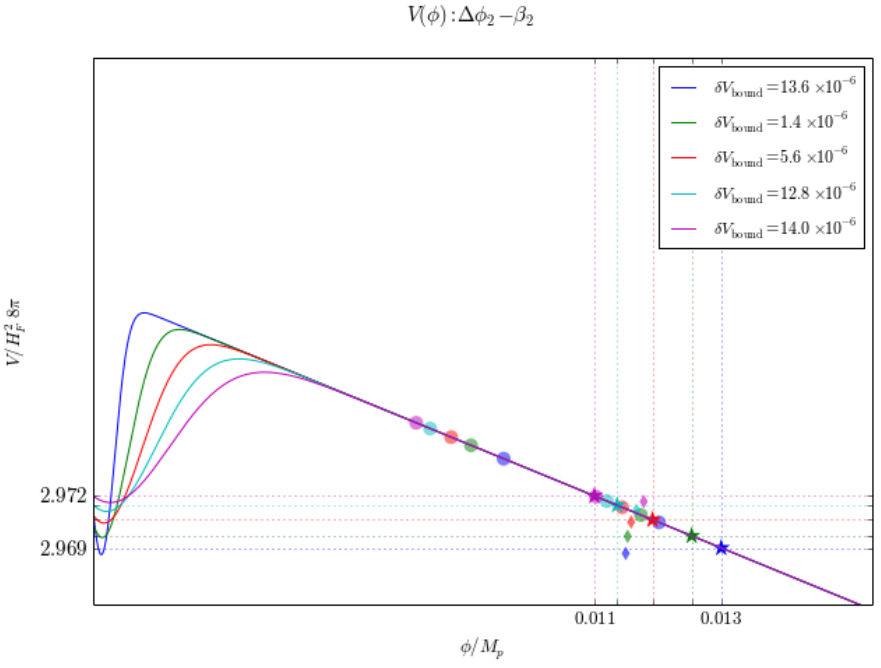

(B)

FIGURE 3.12: Potential for (A) varying $\sigma-\beta_2$ and (B) varying $\Delta\phi_2-\beta_2$. In these plots, we show an upper and lower bound of the field oscillating period (in light filled circles). In addition, we show the first emergence of space-like constant time slice (in stars) which define the V_{TP}. Note that V_{TP} for all cases satisfy the energy constraint as predicted according to Eq. (2.2) in which it lies above the lower bound energy (indicated by diamond).

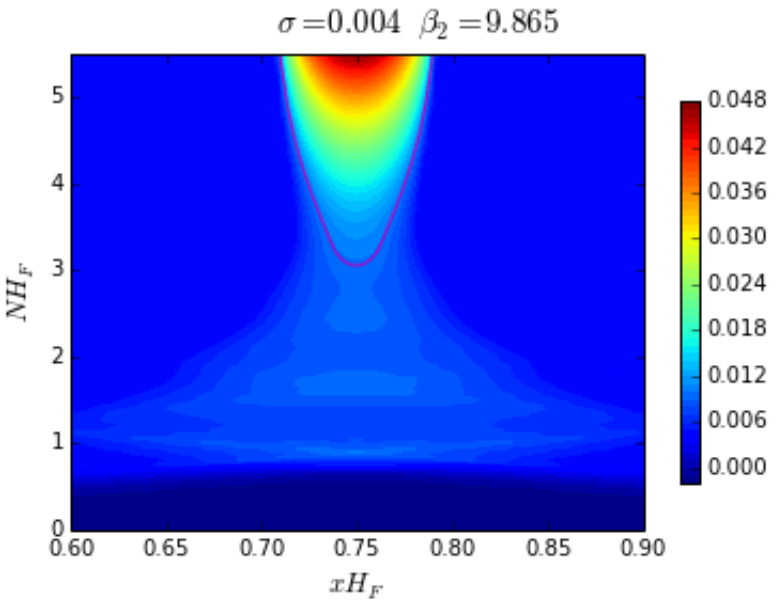

FIGURE 3.13: An example of countour plot for the second model in the $\beta_2 - \sigma$ sector. The magenta line indicates the beginning of inflation.

Therefore, the resulting scale factor is smaller (less time to grow). This indicates that the perturbation in the post-collision decays more. Similarly, the same analysis can be applied to the $\Delta\phi_2 - \beta_2$ sector, and we find the perturbation in the magenta curve decays more.

3.4 Near The Classical Transition Boundary

As we analysed our simulation result for the $\Delta\phi_1 - \beta_1$ sector, it shows a series of bumps start developing near the edge of the bubble (see Fig. 3.2a). This scenario does not appear in the $\beta_1/\Delta\phi_1 - \sigma$ sectors. Recall that in the $\Delta\phi_1 - \beta_1$ sector, σ is chosen to be large enough such that we are guaranteed two bumps do not influence each other (otherwise, we will not be able to distinguish the trend). We then suspect that this is a feature arises from the location of the second bump is in a classical transition boundary. The boundary of a classical transition is defined at the boarder of which the bubble about to enter the slow roll inflationary phase sooner than reaching V_B. We then examined a variety of σ and show that as we push the second barrier towards a greater field value, the lumpiness in $\mathcal{R}''$ starts to build up (see Fig. 3.17.) In the case we investigated, the classical transition boundary is (or vanish) at $\sigma = 0.01875 M_p$.

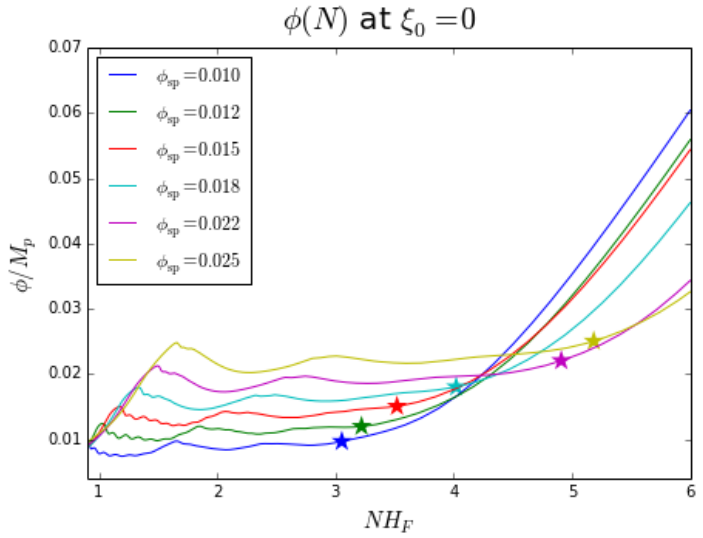

(A)

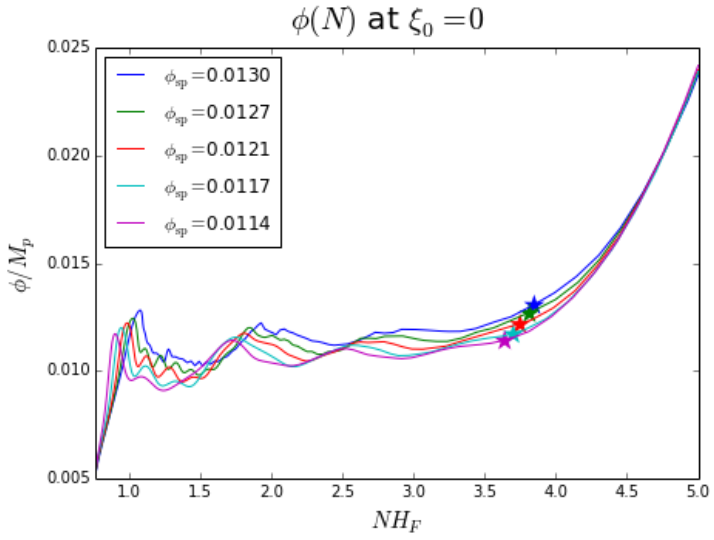

(B)

FIGURE 3.14: $\xi_0 = 0$ slice for (A) varying $\sigma - \beta_2$ and (B) varying $\Delta\phi_2 - \beta_2$. These plots begin at the collision point and the stars indicate the first emergence of space-like constant time slice.

3.4.1 Different Polynomial Potentials

In the first model, we also compare the quadratic potential with polynomial potentials of different orders. In theory, the distance for which the instanton can travel is approximately twice $\Delta\phi_1$. This constrains the second barrier width, $\Delta\phi_2$, to be smaller than the first one. However, in fact, after examining the classical transition boundary for each case, we discovered that for different polynomial potential models, the boundary

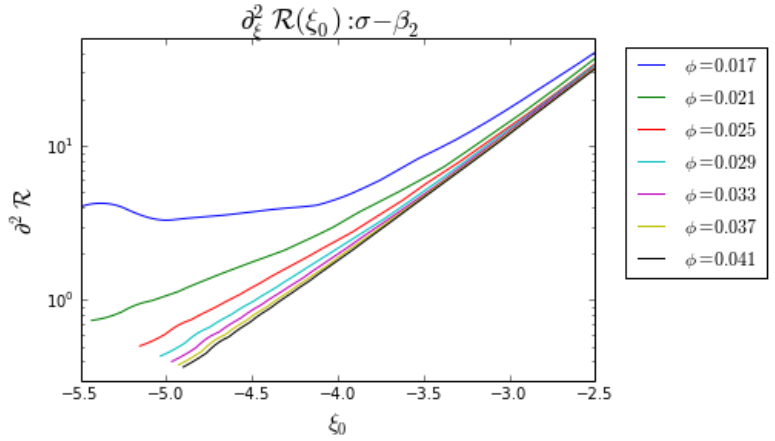

(A)

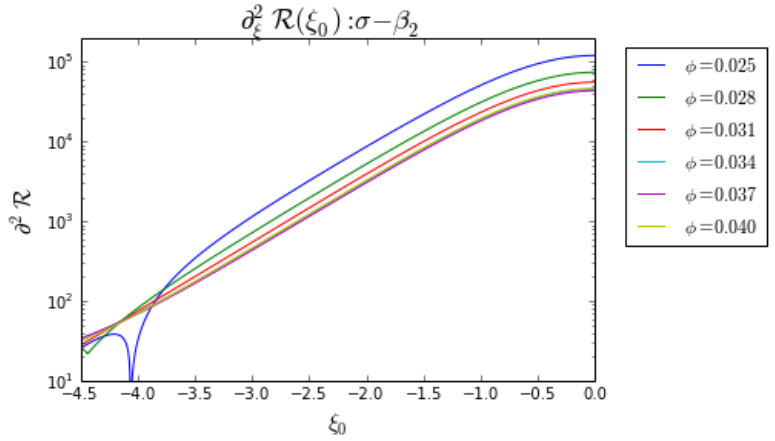

(B)

FIGURE 3.15: Perturbation (for $\sigma - \beta_2$) at different constant field spatial slice near the collision point (A) $\phi_{sp} = 0.01 M_p$ and (B) $\phi_{sp} = 0.025 M_p$.

for which a classical transition can happen is always much greater than $2\Delta\phi_1$ (see Fig. 3.18).

From this observation, the requirement of $\Delta\phi_2 < \Delta\phi_1$ seems invalid. We show a phase diagram (in Fig. 3.19 for $n = 2$ case) for different combinations of β_1 and $\Delta\phi_1$ where a classical transition can happen and find is that there exists a plenty of combinations in which $\Delta\phi_1$ can be smaller than $\Delta\phi_2$. In fact, these combinations trace out a curve and any combination of $\Delta\phi_1$ and β_1 below the curve will forbid a classical transition.

To explain this phenomenon, we looked into the evolution of instanton profiles prior the collision. We find that there are mainly two contributions might potentially give rise to this scenario. The first one is $\phi_{\rm amp}$, which corresponds to the distance that an instanton

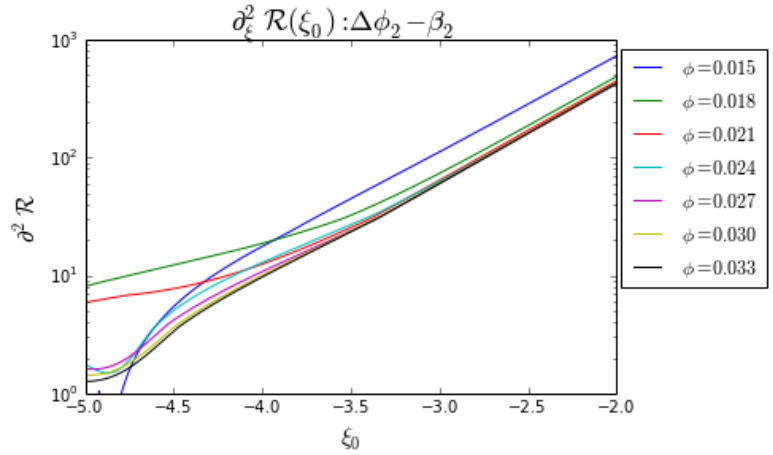

(A)

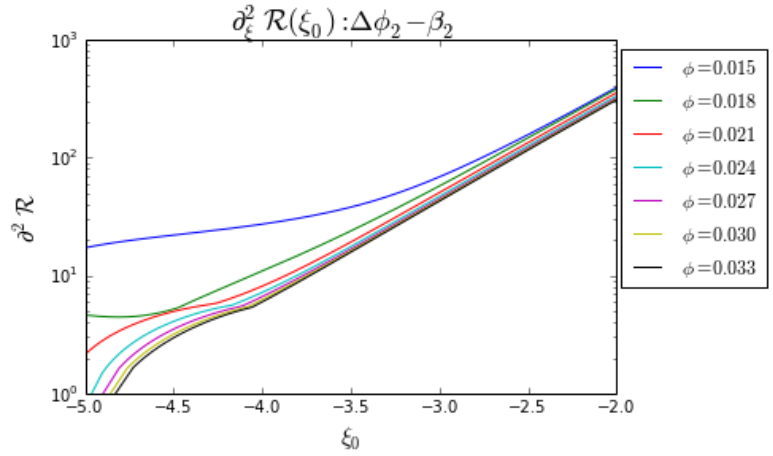

(B)

FIGURE 3.16: Perturbation (for $\Delta\phi_2 - \beta_2$) at different constant field spatial slice near the collision point (A) $\phi_{sp} = 0.013 M_p$ and (B) $\phi_{sp} = 0.0114 M_p$.

tunnel and is associated with $\Delta\phi_1$. The second contribution comes from the fact that the field is rolling down the potential. As the field rolls down, it gains more energy to travel further. To determine if both factors have an equal effect on this, we first notice that, from Fig. 3.18a, as the polynomial becomes higher order, the distance in which the instanton can travel shrinks. However, from Fig. 3.18b, we see the instanton profile for different orders of polynomials, the amplitude, ϕ_{amp}, remains the same. This indicates that the instanton endpoint remain the same in all cases and the contribution due to ϕ_{amp} is irrelevant. Thus, the main contribution should come from the rolling part. We verify this by showing that (in Fig. 3.20) the jump size ($\delta\phi \equiv \phi_B - \phi_A$) is proportional to $1/\sqrt{\epsilon}$, where ϵ is the slow roll parameter.

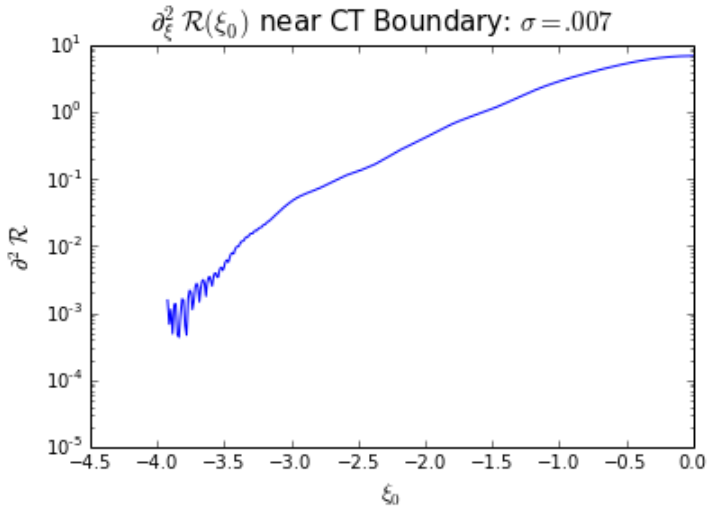

(A)

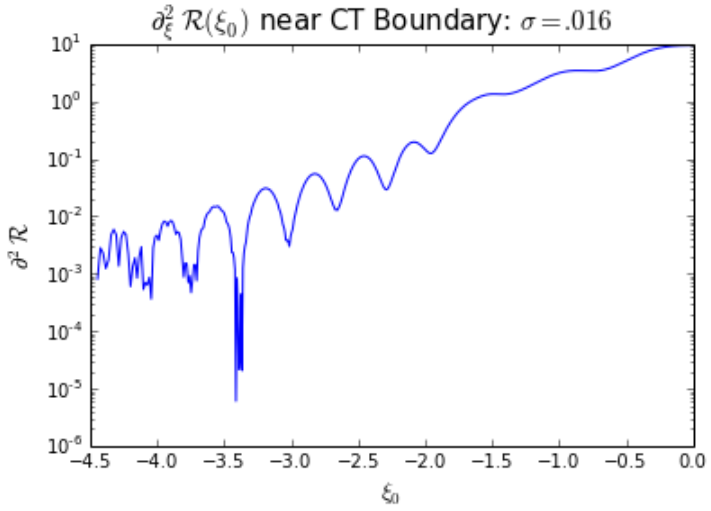

(B)

FIGURE 3.17: Growth of lumpiness as the second bump approaches classical transition boundary (A) show a shift at $\sigma = .007$ (B) shows a shift at $\sigma = .016$ with the following parameters: $\Delta\phi_1 = 0.001061$, $\Delta\phi_2 = 0.00071$, $\beta_1 = 2.0$ and $\beta_2 = 3.0$.

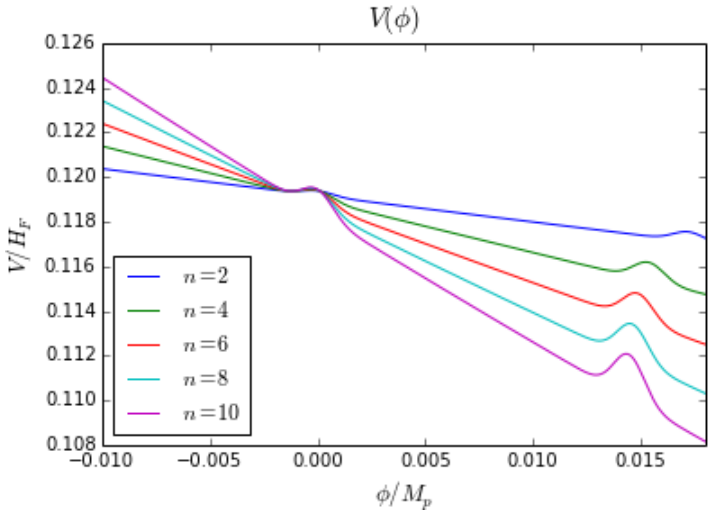

(A)

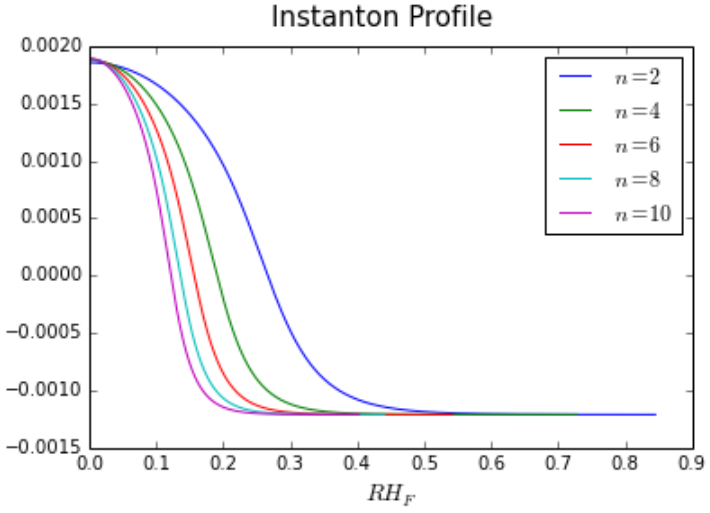

(B)

FIGURE 3.18: (A) Pontentials with different even powers. The metastable minimum indicates classical transition boundary. (B) Instanton profiles for different even powers.

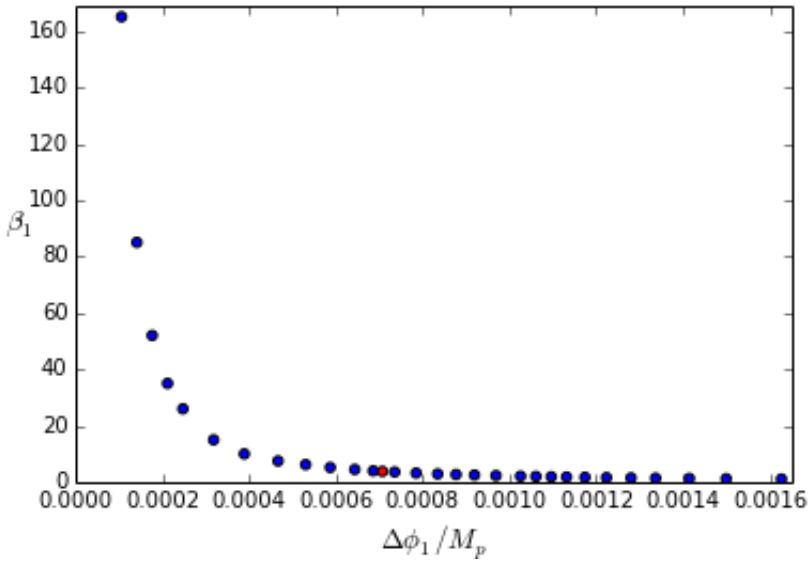

FIGURE 3.19: Boundary for classical transition with parameter: $\sigma = 0.01875$, $\Delta\phi_2 = .000707$ and $\beta_2 = 3$. Any combination below the line will forbid a classical transition to occur. The red filled dot indicates the point at which $\Delta\phi_1$ becomes smaller than $\Delta\phi_2$

.

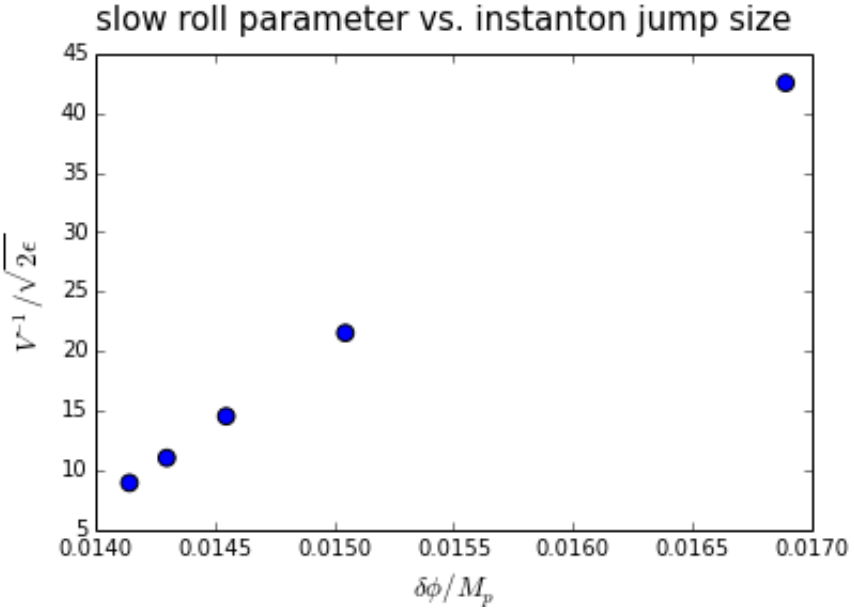

FIGURE 3.20: Jump size for instanton at different powers of field potential and its relation to the slow roll parameter, ϵ.

Chapter 4

Conclusion

The theory of inflation explains the picture of our Universe successfully. However, inflation can become eternal and allow a universe with many bubbles. This is known as a multiverse. These bubbles can be descended from their parent universe(s) via different mechanisms depending on an underlying potential landscape. One possibility of giving birth to the next generation universes is through the process of a bubble collision which is referred to as a classical transition. In this thesis, we investigated the possibility of observing the signature associated with a classical transition. As a starting point, we studied two types of models, both of them a quadratic potential with two Gaussian bumps. In the first model, both Gaussian barriers are above the inflation plateau. In the second model, the second barrier is beneath the inflationary plateau. Our primary task was to determine if the aftermath of a bubble collision is a potential source of a CMB anisotropy. Particularly, we expect a universe resulting from a classical transition has an impact primarily on the lowest mode in the CMB power spectrum since the collision always covers the whole universe. We relate the CMB multipole moment to the comoving curvature in the Sachs Wolfe limit. In this case, as we expand the comoving curvature perturbation around an arbitrary observer's location, the first dominant contribution is from the second spatial derivative of the comoving curvature perturbation. We find this directly from simulations, by extracting a spatial slice at later time by which the comoving curvature perturbation has frozen in. This corresponds to the $l = 2$ mode in the CMB power spectrum. However, specifying the perturbation in a particular patch of the universe is insufficient to determine the observability unless we specify the local curvature associated with it. This is related to the local expansion rate in which it can

be calculated directly from the simulation as well. The result indicates that the second model will produce a much greater signature as compared to the first model.

We also investigated each individual model from different aspects. In the first model, we showed that there are primarily two sources that determine the aftermath: **(1)** the kinematics and **(2)** the potential shape. The kinematics is parametrized by the Lorentz factor (γ) at the collision point and depends on the initial separation as well as the initial bubble radius. To create the largest perturbation signature in the CMB quadruple moment, one finds this can be done by minimizing the initial radius or maximize the initial separation to obtain a larger γ. On the other hand, in the potential shape factor, we showed that the aftermath only depend on the configuration of a potential as long as the kinematics is fixed. If the two barriers do not overlap with each other, we showed that there is a linear trend in the comoving curvature perturbation as well as the scale factor where a smaller field amplitude will result a larger perturbation (and a smaller scaler factor). During the analysis, we survey in the vicinity of a classical boundary and conclude a few observations:

1. Near a classical transition boundary, there is an evidence of growth of lumpiness in the comoving curvature perturbation.
2. Classical transition boundary is located at a point much greater than twice of $\Delta\phi_1$ in which the contributions come from
   (a) distance between V_A and the instanton endpoint
   (b) the slow roll phase between the instanton endpoint and V_B
3. There is a phase boundary in $\beta_1 - \Delta\phi_1$ in which a classical transition is forbidden.
4. In different polynomial potentials, the location of a classical transition boundary is proportional to $1/\sqrt{\epsilon}$, where ϵ is the slow roll parameter.

In the second model, when the energy at the collision point is sufficient, regardless of the surrounding vacuum energy being higher or lower than the transient energy, a classical transition will always happen. Depending on the relative energy difference between V_B and V_{TP}, it is possible to produce different post-collision geometry. We verify this by

using different amplitudes in the second barrier (parametrized by β_2) and explore three different kinds of geometries in the domain wall:

1. $V_B > V_{\rm TP}$: *Repulsive*
2. $V_B \lesssim V_{\rm TP}$: *Marginal Repulsive*
3. $V_B \ll V_{\rm TP}$: *Oscillatory*

We then focus on the investigation of a marginal repulsive geometry. Since the energy difference in this case is in the marginal limit, it is possible that the condition of $V_B \lesssim V_{\rm TP}$ is violated. We examine this condition by first deriving an expression for the lower bound energy where $V_{\rm TP}$ can exist. After running the simulation, we extract the first appearance of space-like spatial slices in which the coordinate of a new formed bubble is well defined. This field value defines the $V_{\rm TP}$. As we have shown, in all cases of marginal repulsive geometry that we examined, the lower bound energy constraint is satisfied and since $V_B < V_{\rm TP}$, we showed that there is a contracting phase in the post-collision region. Furthermore, due to the vacuum energy between V_B and $V_{\rm TP}$ are really close, there is a period that the the field oscillates in the transient region as it rolls towards the true vacuum.

In this thesis, we give a prediction to the CMB anisotropy of a bubble collision and the associated local curvature in different patches of the bubble. The signature can vary a lot based on a specific choice of the model, as we have shown from the models we studied. The prediction to the value of $\mathcal{D}_2$ depends on the observed local curvature and in order to conclude if the prediction is consistent with observation, a more precise measurement on the local spatial curvature is required. In our future work, we will extend the degree of freedom from a scalar field to a multi-fields theory since the nature may contain more than one single scalar field. In this case, the superposition of these scalar fields may produce an alternate signature. Also, the choice of our potential model is arbitrary. In our next step, we can extend the theory by deriving a potential landscape from a well motivated theory. For example, string theory predicts the existence of extra spatial dimensions. Since we do not observe these extra dimensions, they are meant to be compact. The effect of these extra dimensions can indirectly influence our four dimensional world via the process of compactification. As a result, these extra degrees of

freedom in spatial dimensions becomes an effective four dimensional field theory which potentially allow us to study its properties. The potential derived from this theory as a study tool for a bubble collision may be a smoking gun to explore the nature in strings.

Appendix A

Preliminary Instanton Profile

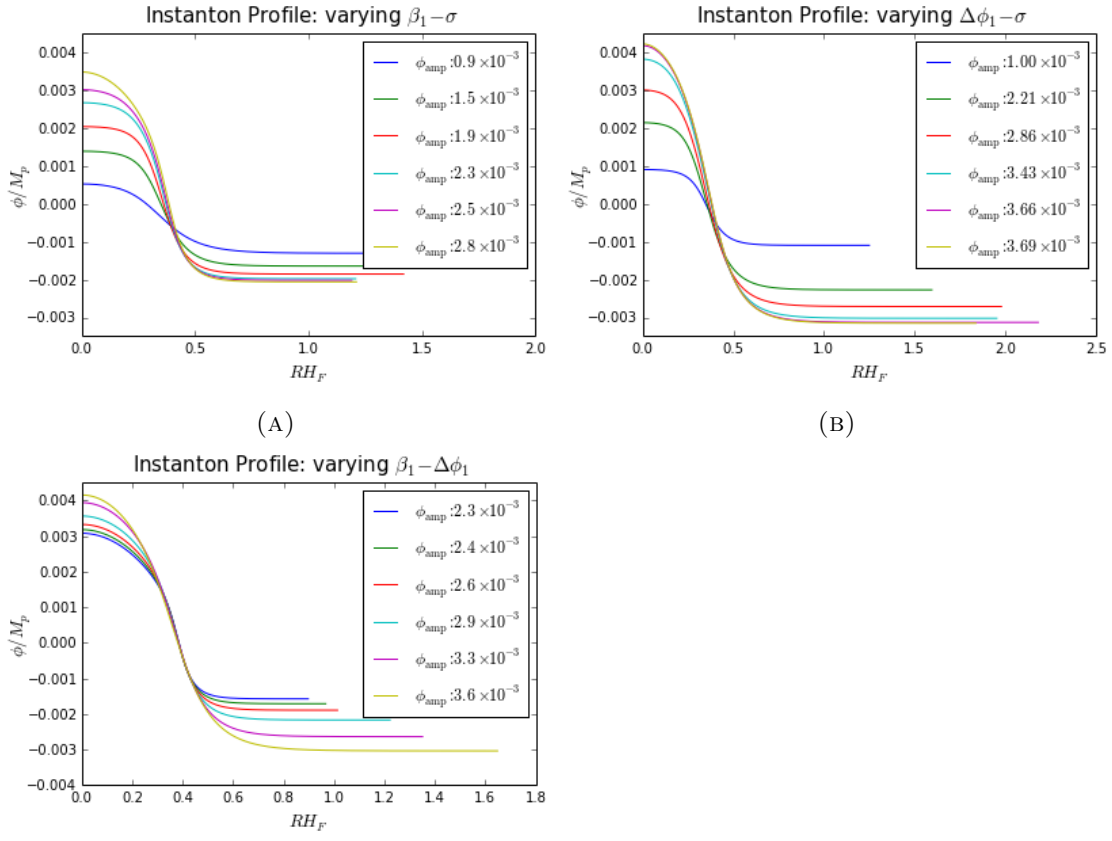

(A) (B)

(C)

FIGURE A.1: Instanton profiles showing different sectors with constant $R = 0.351 H_A^{-1}$. In these plots we vary different parameters associated with the potential shape in all possible combinations to obatian a variety of instanton smplitude while holding the initial bubble radius the same.

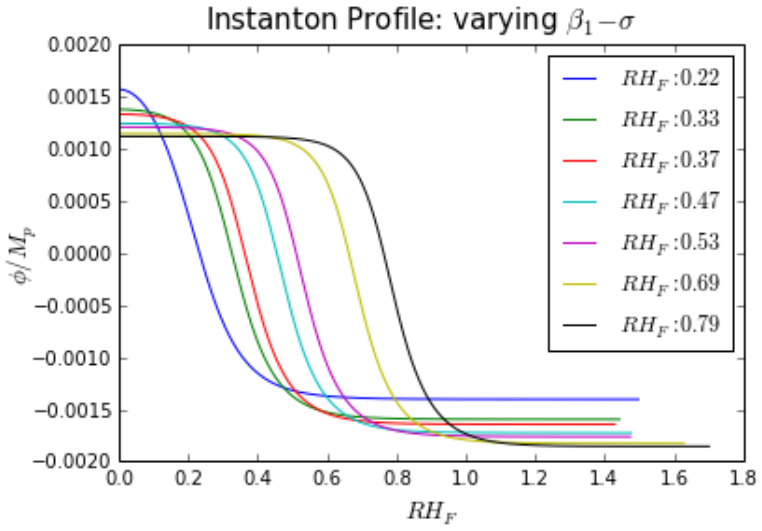

(A)

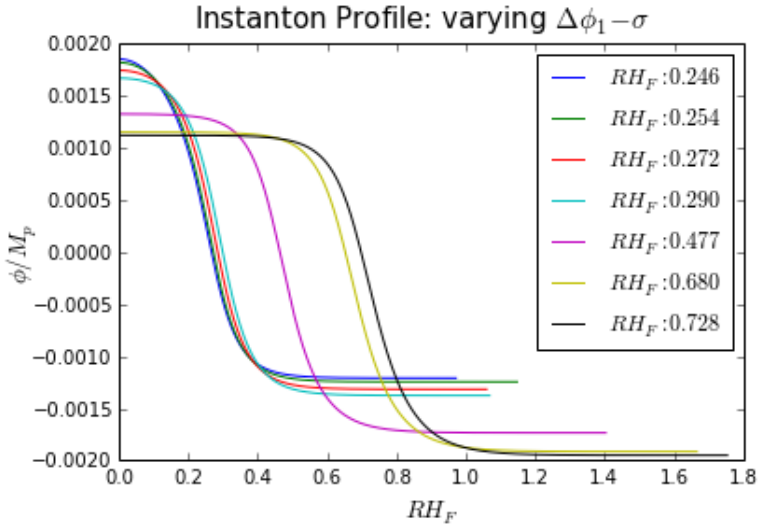

(B)

FIGURE A.2: Instanton profiles showing different initial bubble radii in (A)$\phi_{\text{amp}} = 0.00148M_p$ (B)$\phi_{\text{amp}} = 0.00153M_p$. In these plot, we are able to vary two parameter sets associated with the potential shape to obtian a variety of initial bubble radii while maintianing the instanton amplitude constant.

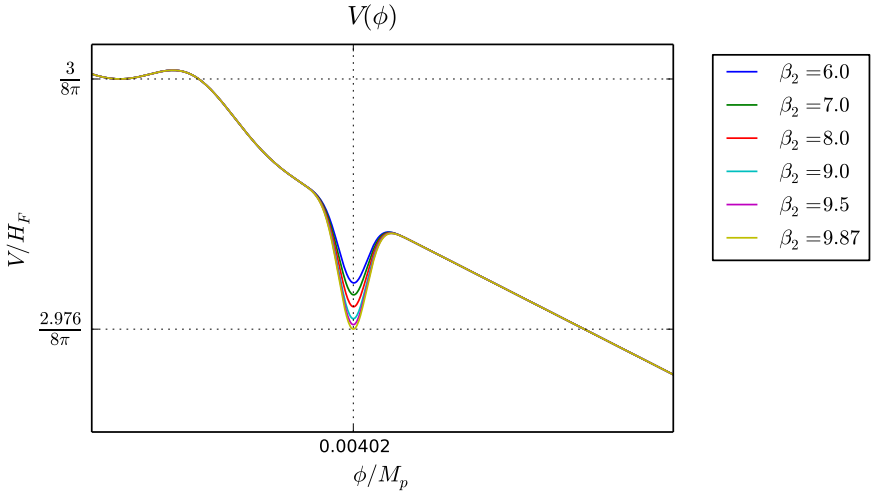

(A)

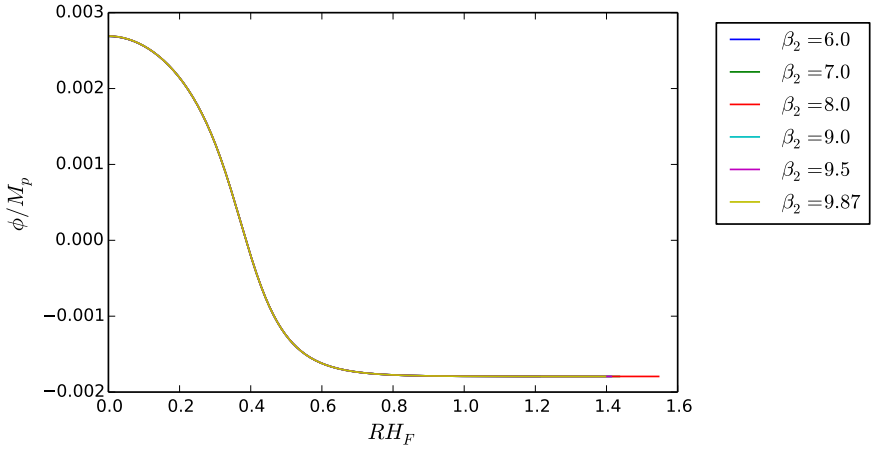

(B)

FIGURE A.3: At different β_2 (A), the instanton profile (B) remain the same. In these plots, we verify that for different potential amplitude parametrized by β_2, the corresponding instanton profiles remain the same.

Appendix B

$\mathcal{R}''$ and a_0 Profiles

B.1 AIP

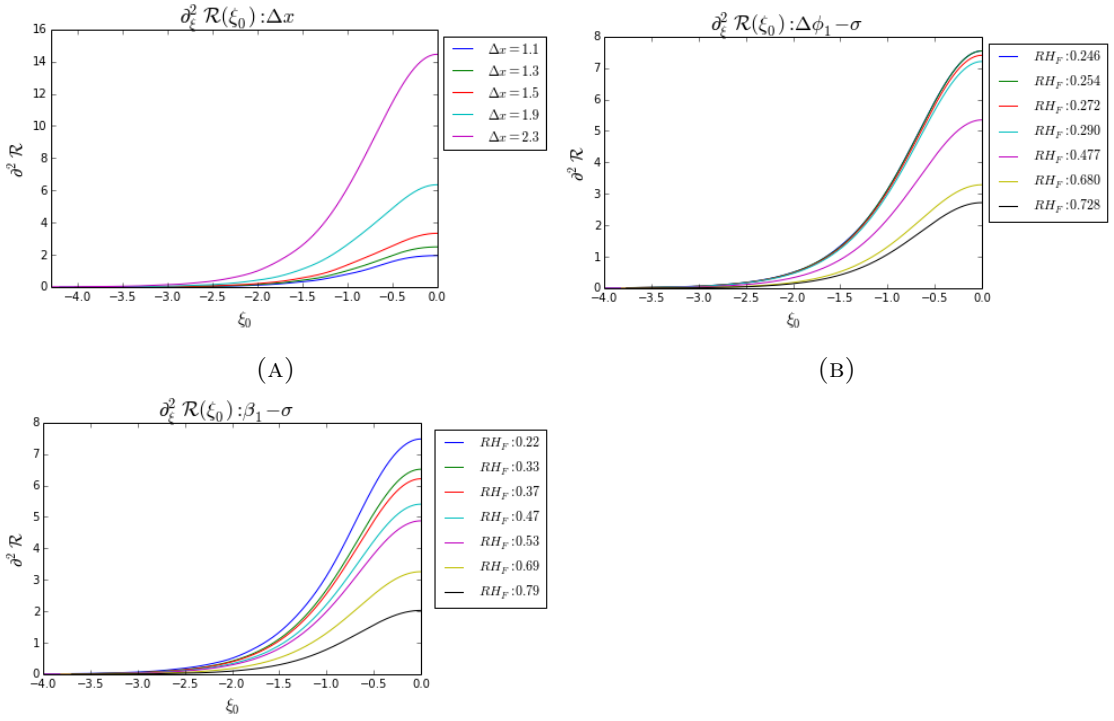

FIGURE B.1: $\mathcal{R}''$ profiles for the kinematics factor (AIP case). (A) indicates different initial separation, (B) and (C) for different initial radii. These plots show the second spatial derivative of the comoving curvature perturbation as a function of different observer labelled by ξ_0. As we can see, the observers at the bubble center ($\xi_0 = 0$) see the greatest signature. The outcome here is studied for the kinematics factor

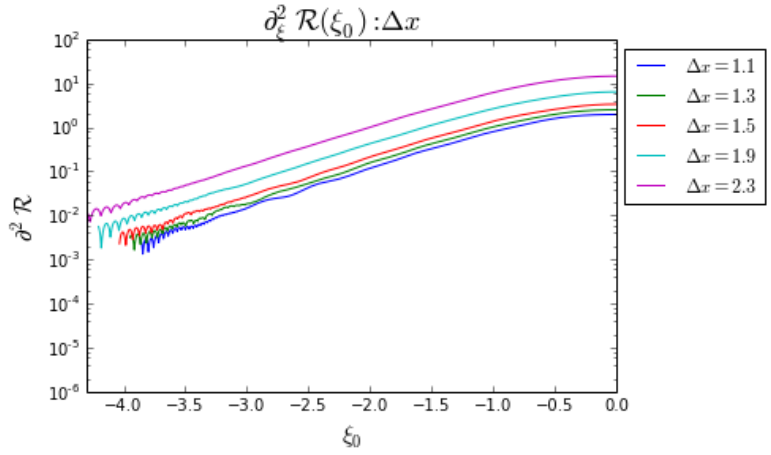

(A)

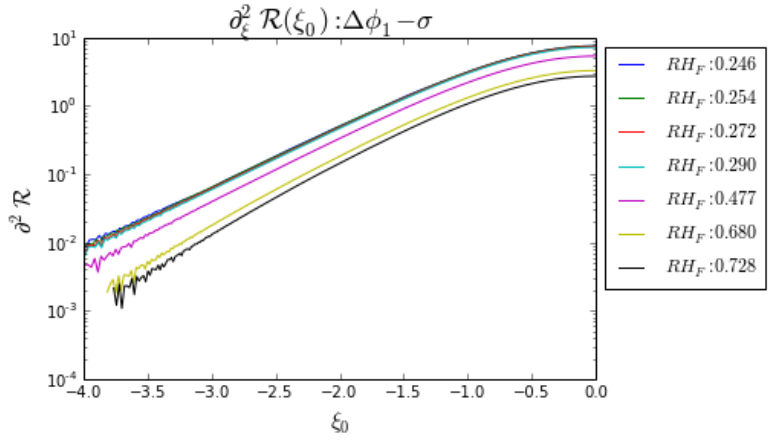

(B)

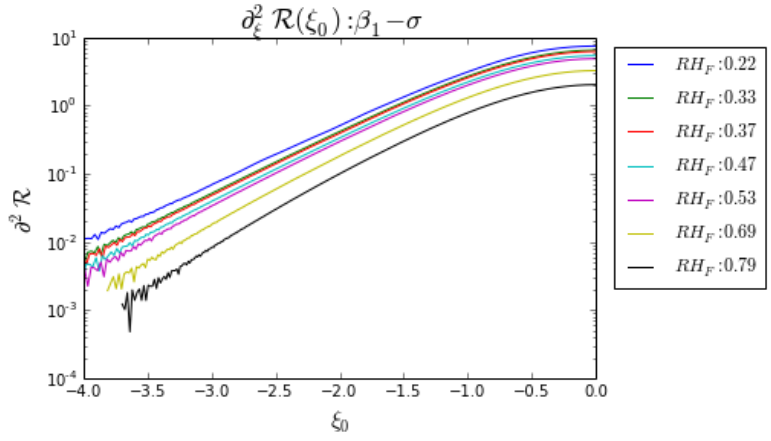

(C)

FIGURE B.2: Identical plots as in Fig B.1 but shown in logged scale. In these plots, a clearer end heaviour near the bubble edge are shown

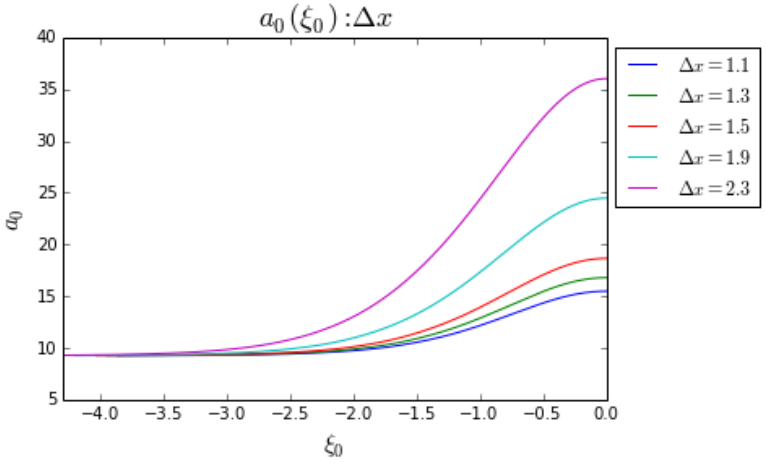

(A)

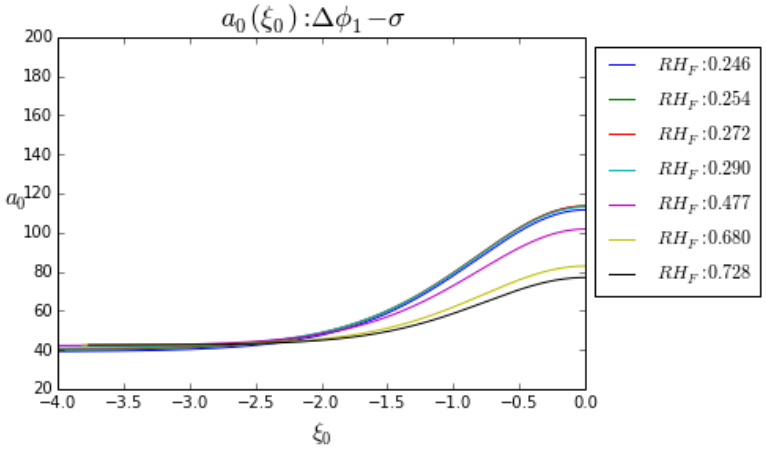

(B)

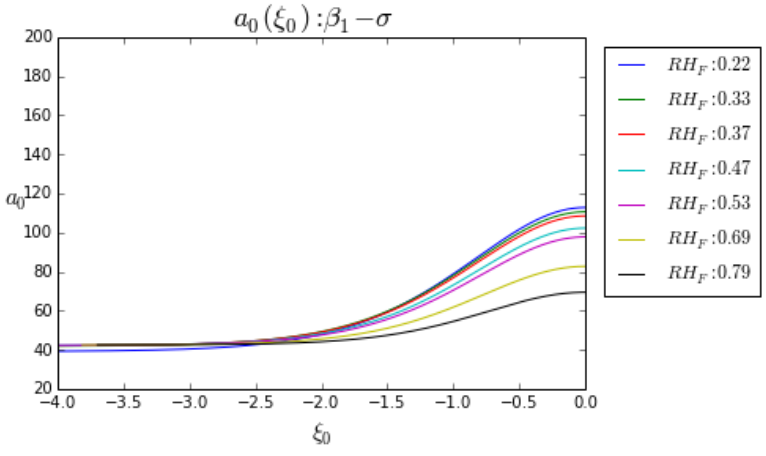

(C)

FIGURE B.3: a_0 profiles for the kinematics factor. (A) indicates different initial separation, (B) and (C) for different initial radii. These plots show the scale factor for different observer labelled by ξ_0. The observer located at the bubble center will experience a larger expansion rate than the one near the bubble edge.

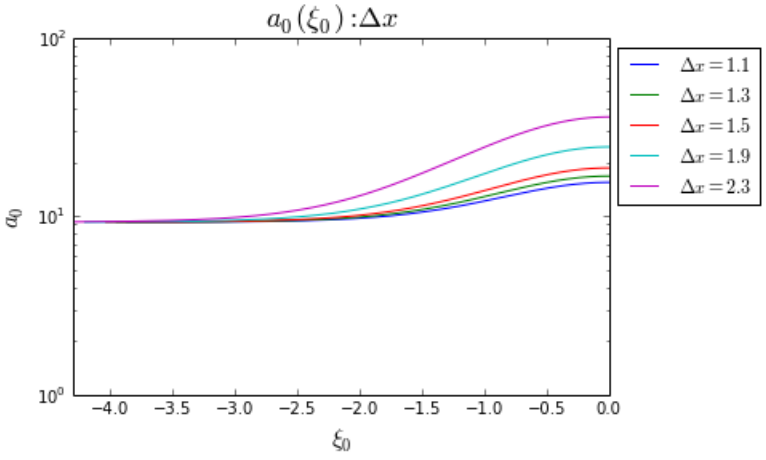

(A)

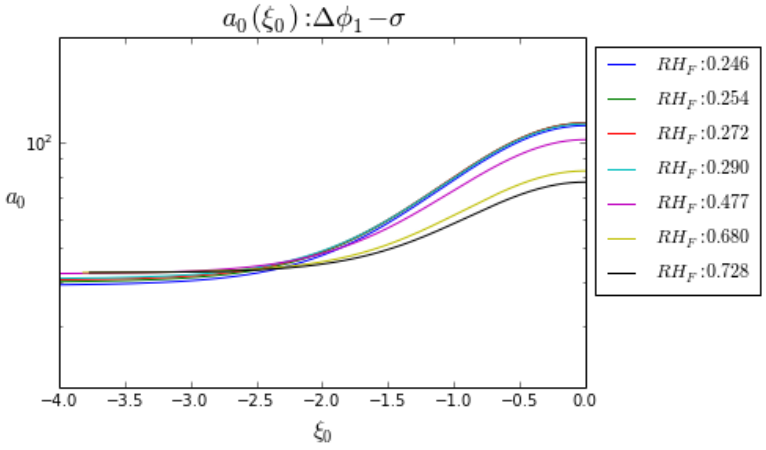

(B)

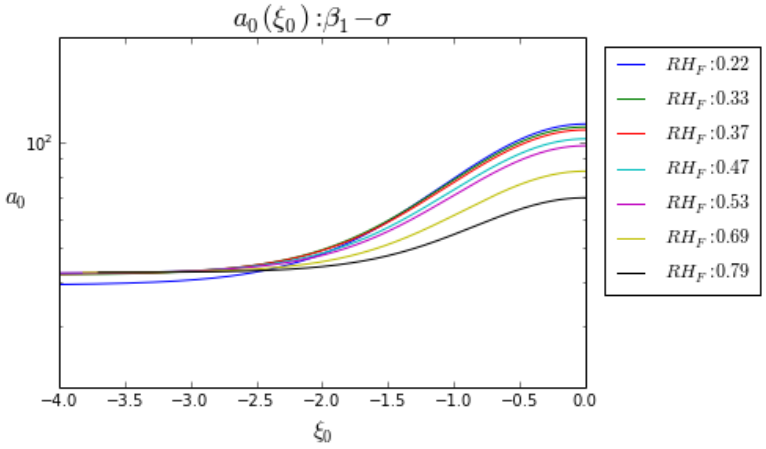

(C)

FIGURE B.4: Identical plots as in Fig B.3 but plotted in log scale which gives a clearer behaviour near the bubble edge.

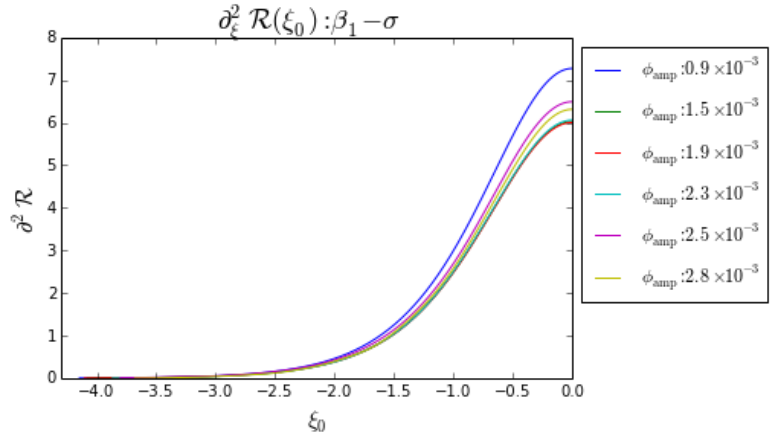

(A)

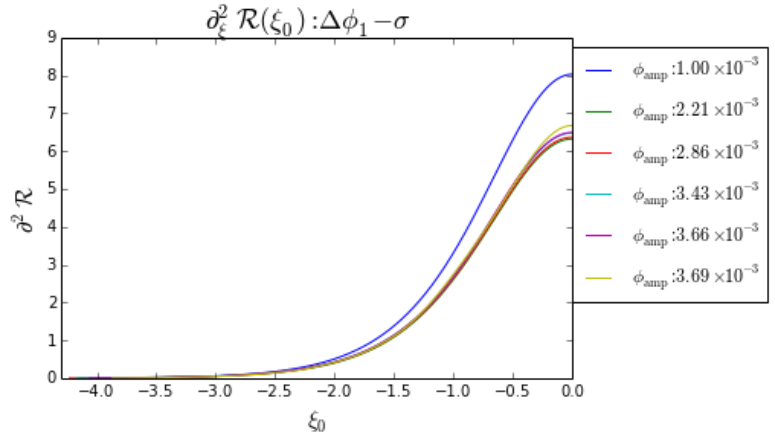

(B)

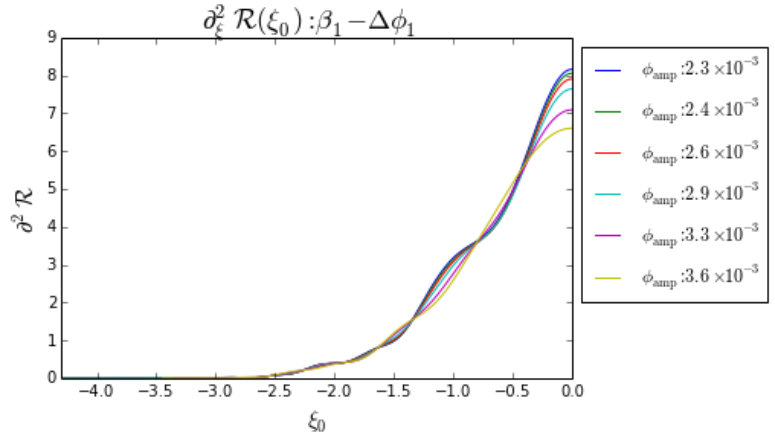

(C)

FIGURE B.5: $\mathcal{R}''$ profiles for the potential shape factor. These plots shows the aftermath of a bubble collision due to varying the instanton amplitude which solely depends on the potential shape.

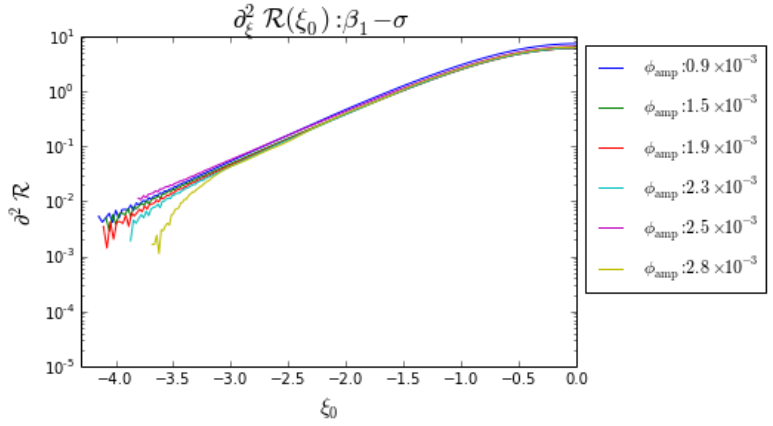

(A)

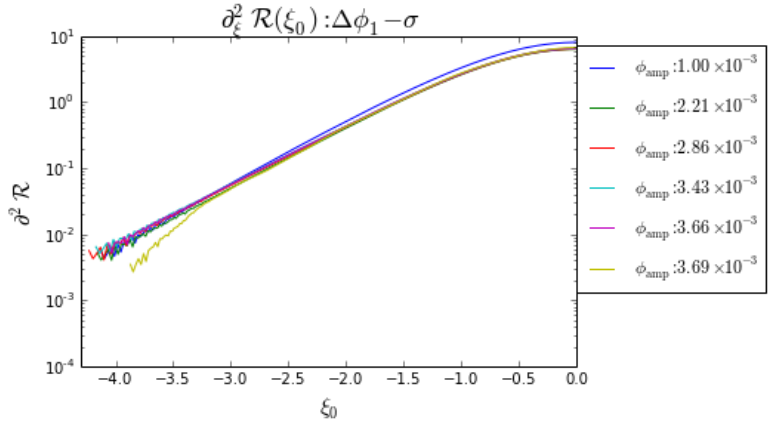

(B)

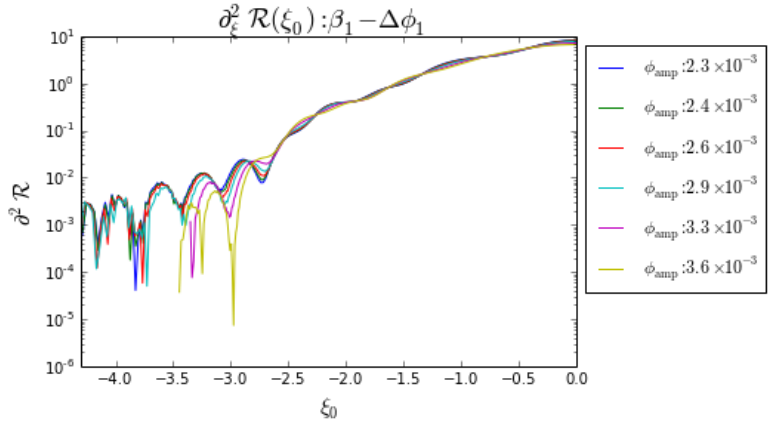

(C)

FIGURE B.6: Identical plots as in Fig B.5 but shown in logged scale.

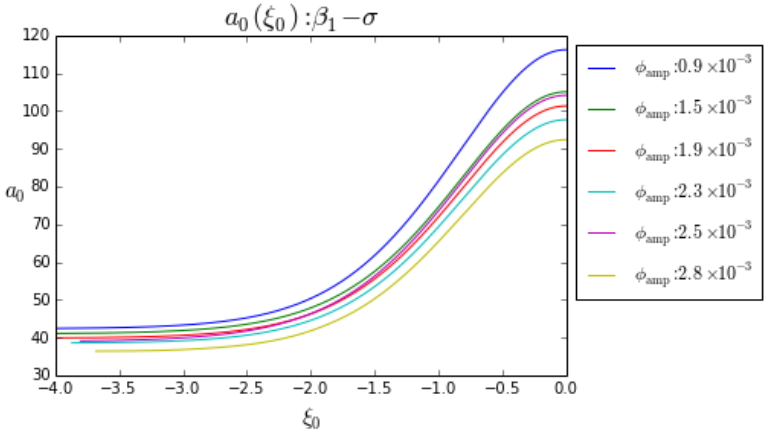

(A)

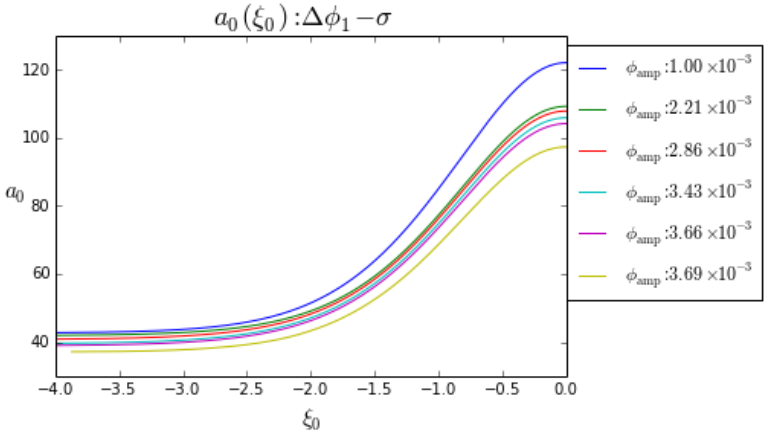

(B)

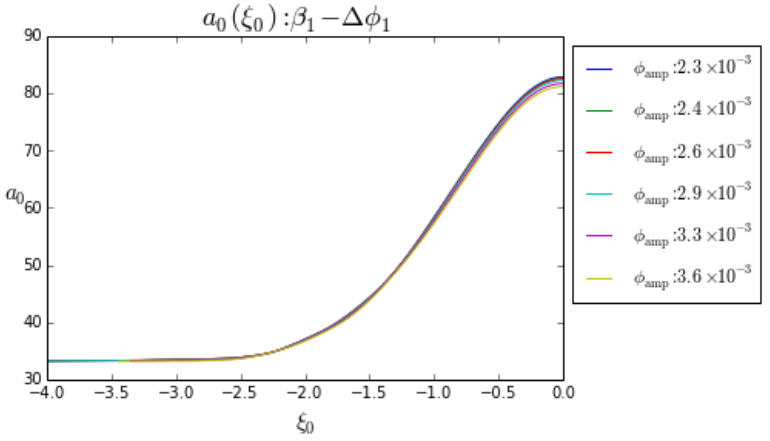

(C)

FIGURE B.7: a_0 profiles in different sector for due to the potential factor in which is obtained by varying the instanton smplitude. Similar trend is seen in the kinematics factor.

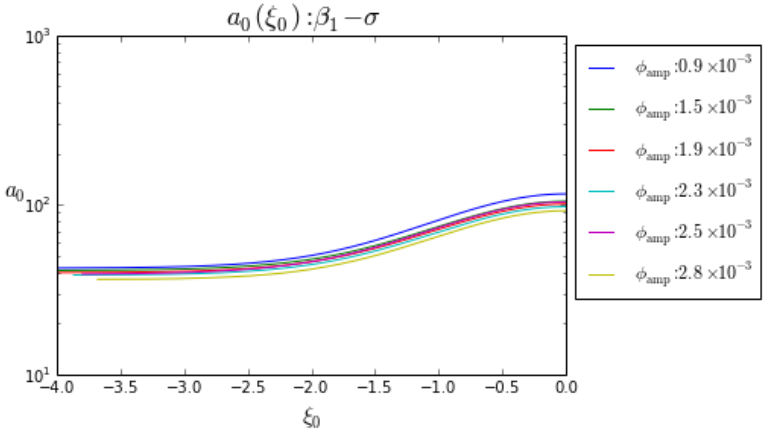

(A)

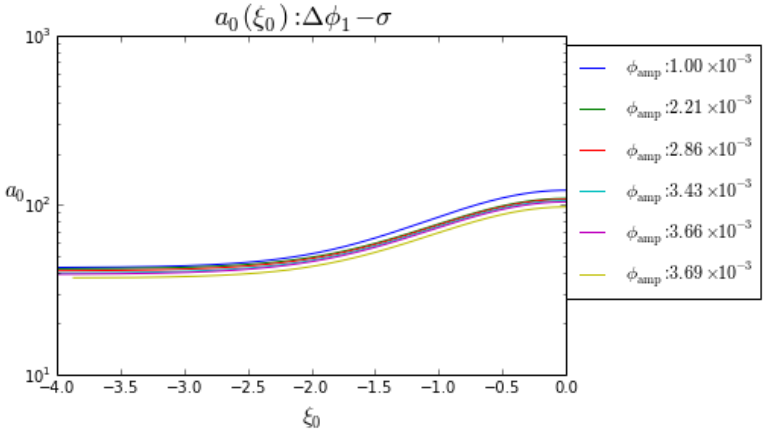

(B)

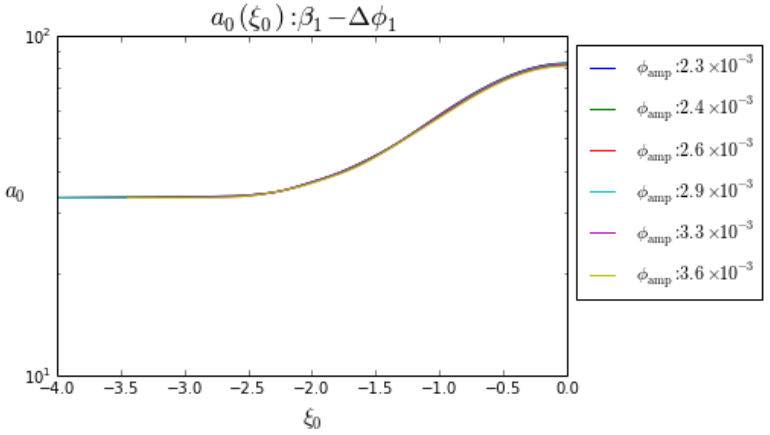

(C)

FIGURE B.8: Identical plots as in Fig B.7 but shown in log scale.

B.2 BIP

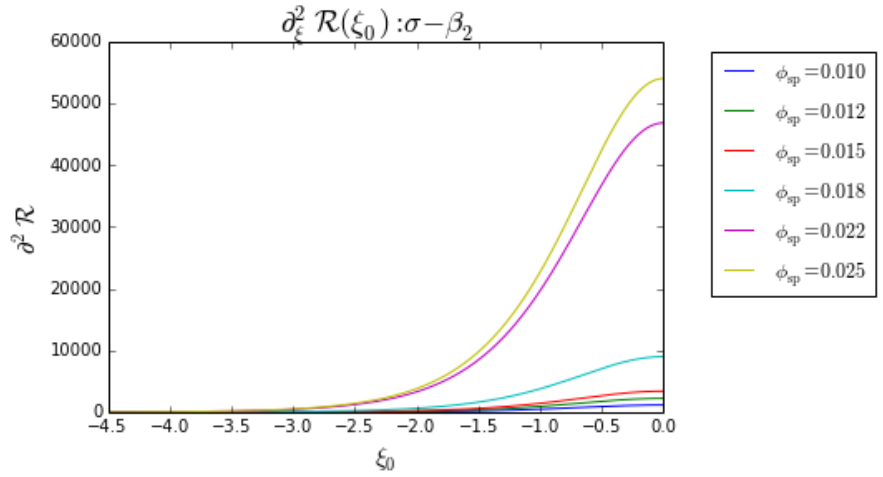

(A)

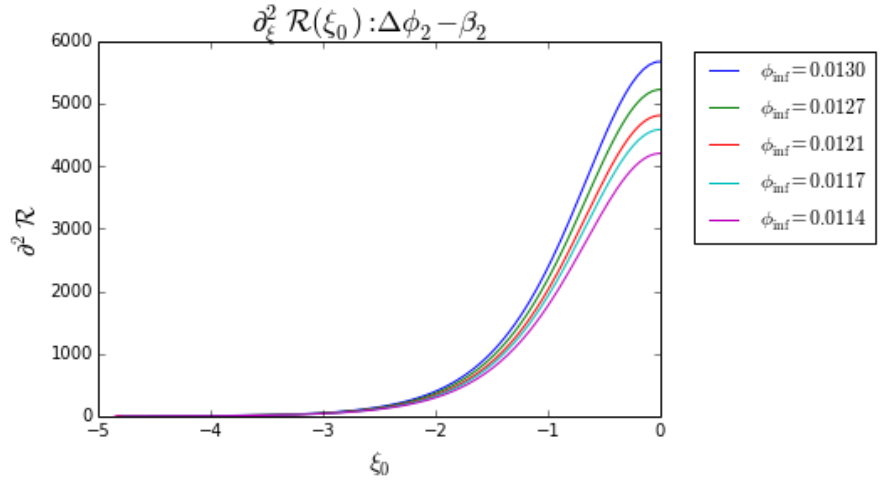

(B)

FIGURE B.9: $\mathcal{R}''$ from the simulation results. (A) $\sigma - \beta_2$ and (B) $\Delta\phi_2 - \beta_2$ sectors. These plots show the second spatial derivative of comoving curvature in the BIP model. As an contrast to the AIP model, the peak at the bubble center is much larger in this case

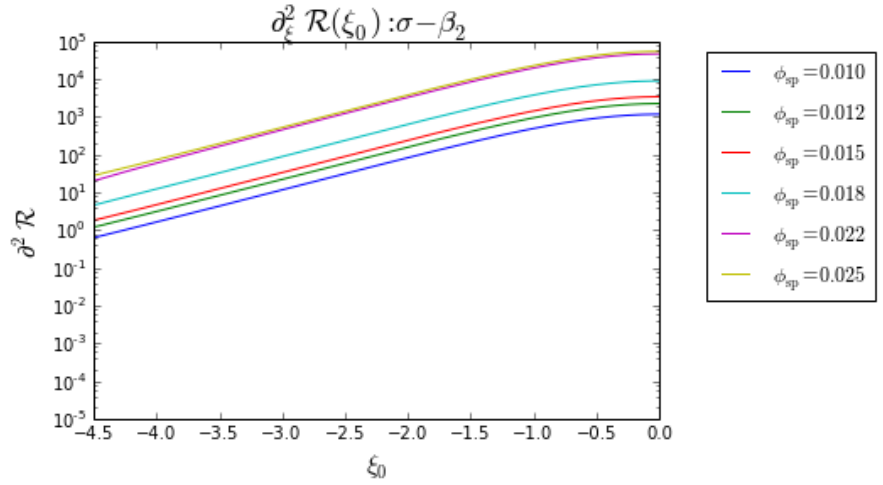

(A)

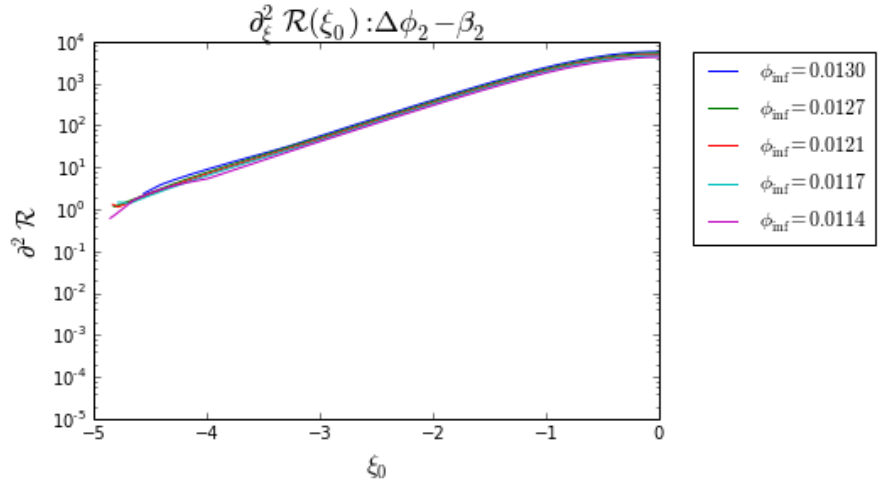

(B)

FIGURE B.10: Identical plots as in Fig B.9 but shown in log scale to obtain clearer end behaviour near the bubble edge.

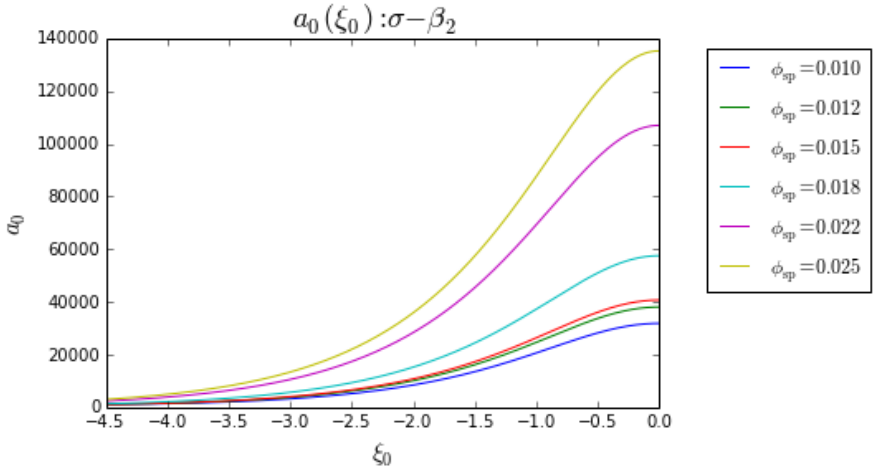

(A)

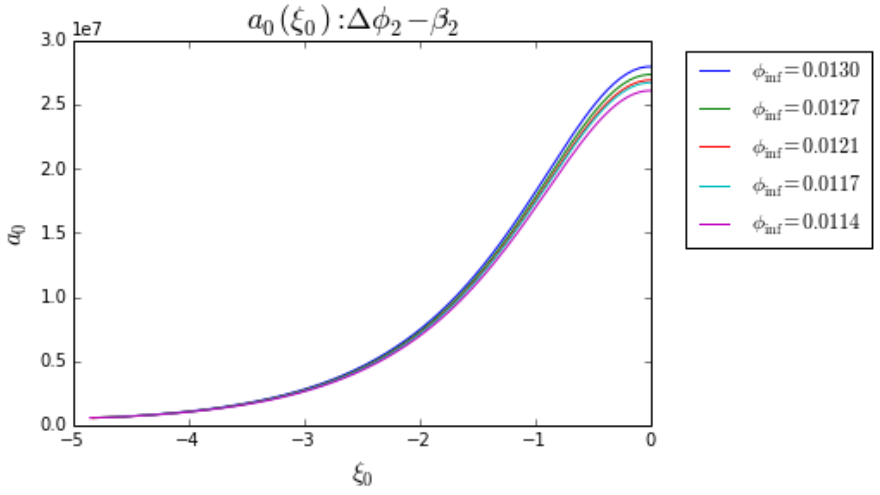

(B)

FIGURE B.11: a_0 prediction according to the simulation results. (A) $\sigma - \beta_2$ and (B) $\Delta\phi_2 - \beta_2$ sectors. In these plots, we see the observer near the bubble edge stay almost stationary compare to the one located at the bubble center.

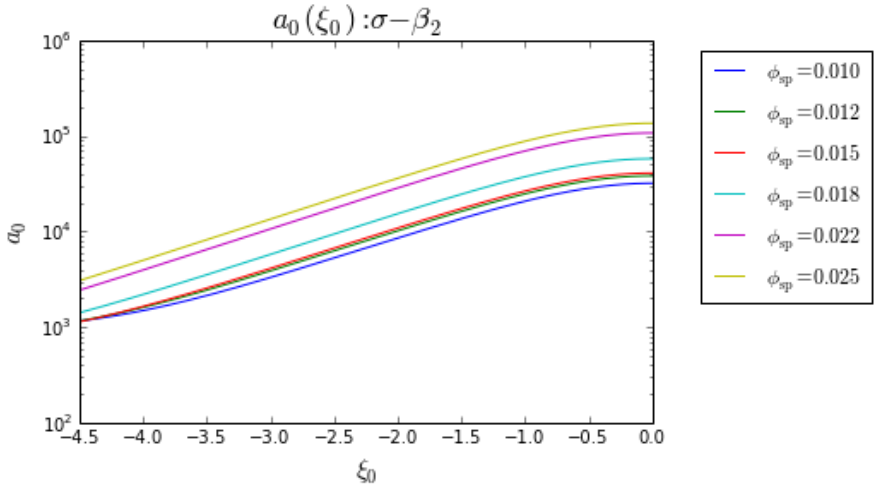

(A)

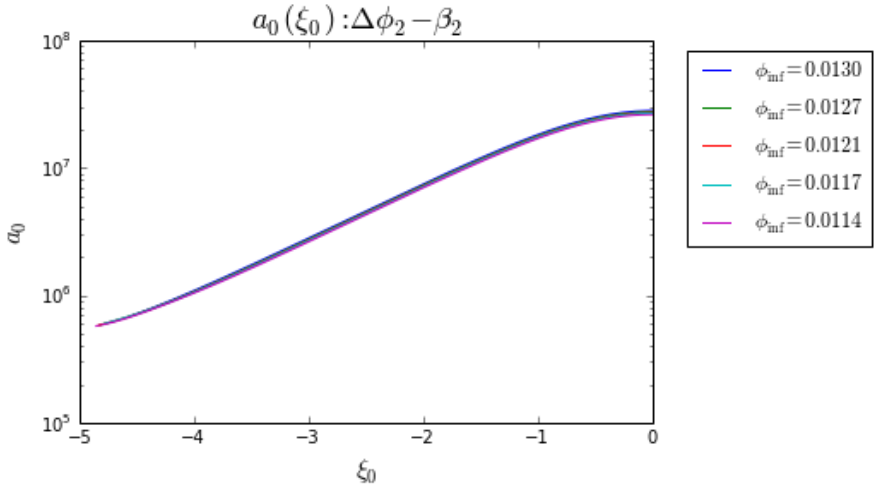

(B)

FIGURE B.12: Identical plots as in Fig B.11 but shown in logged scale.

Bibliography

A. A. Penzias and R. W. Wilson. A measurement of excess antenna temperature at 4080 mc/s. *Astrophysical Journal, vol. 142, p.419-421*, 1965.

Carroll L. Wainwright, Matthew C. Johnson, Hiranya V. Peiris, Anthony Aguirre, Luis Lehner, and Steven L. Liebling. Simulating the universe(s): from cosmic bubble coolisions to cosmological observables with numerical relativity. *JCAP*, 03(030), 12 2014a. URL `http://arxiv.org/abs/1312.1357`.

Carroll L. Wainwright, Matthew C. Johnson, Anthony Aguirre, and Hiranya V. Peiris. Simulating the universe(s) ii: phenomenology of cosmic bubble collisions in full general relativity. 07 2014b. URL `http://arxiv.org/abs/1407.2950`.

Planck, P. A. R. Ade, N. Aghanim, M. Arnaud, M. Ashdown, J. Aumont, C. Baccigalupi, A. J. Banday, R. B. Barreiro, J. G. Bartlett, N. Bartolo, E. Battaner, R. Battye, K. Benabed, A. Benoit, A. Benoit-Levy, J.-P. Bernard, M. Bersanelli, P. Bielewicz, A. Bonaldi, L. Bonavera, J. R. Bond, J. Borrill, F. R. Bouchet, F. Boulanger, M. Bucher, C. Burigana, R. C. Butler, E. Calabrese, J.-F. Cardoso, A. Catalano, A. Challinor, A. Chamballu, R.-R. Chary, H. C. Chiang, J. Chluba, P. R. Christensen, S. Church, D. L. Clements, S. Colombi, L. P. L. Colombo, C. Combet, A. Coulais, B. P. Crill, A. Curto, F. Cuttaia, L. Danese, R. D. Davies, R. J. Davis, P. de Bernardis, A. de Rosa, G. de Zotti, J. Delabrouille, F.-X. Desert, E. Di Valentino, C. Dickinson, J. M. Diego, K. Dolag, H. Dole, S. Donzelli, and et al. (201 additional authors not shown). Planck 2015 results. xiii. cosmological parameters. *Astronomy and Astrophysics*, 02 2015. URL `http://arxiv.org/abs/1502.01589`.

Alan H. Guth. Eternal inflation and its implications. 2007. URL `http://arxiv.org/abs/hep-th/0702178`.

Alan H. Guth and J. Erick Weinberg. Could the universe have recovered from a slow first-order phase transition? *Nuclear Physics B, Volume 212, Issue 2, p. 321-364.*, 1983.

A. D. Linde. A new inflationary universe scenario: A possible solution of the horizon, flatness, homogeneity, isotropy and primordial monopole problems. *Physics Letters B, 108 (6):389 – 393*, 1982.

Serge Winitzki. The eternal fractal in the universe. *Phys.Rev.*, D65:083506, 2002. URL `http://arxiv.org/abs/gr-qc/0111048`.

Andrei Linde. Eternal chaotic inflation. *Mod. Phys. Lett. A 1, 81-5*, 1986.

S. Coleman. Fate of false vacuum: Semiclassical theory. *Physical Review D*, 15(10), May 1977.

C. G. Callan and S. Coleman. Fate of false vacuum. ii. first quantum corrections. *Physical Review D*, 16(6), September 1977.

S. Coleman and F. De Luccia. Gravitational effects on and of vacuum decay. *Physical Review D*, 21(12), June 1980.

G. W. Gibbon and S. W. Hawking. Cosmological event horizon, thermodynamics, and particle creation. *Physical Review D*, 15(10), May 1977.

S.W. Hawking and I. G. Moss. Supercooled phase transitions in the very early universe. *Phys. Lett. B 110, 35*, 1982.

Richard Easther, John T. Giblin Jr, Lam Hui, and Eugene A. Lim. A new mechanism for bubble nucleation: Classical transition. 07 2009. URL `http://arxiv.org/abs/0907.3234`.

S. W. Hawking, I. G. Moss, and J. M. Stewart. Bubble collisions in the very early universe. *Phys. Rev. D26 2681*, 1982.

Matthew C Johnson and I-Sheng Yang. Escaping the crunch: gravitational effects in classical transition. 05 2010. URL `http://arxiv.org/abs/1005.3506`.

Anthony Aguirre and Matthew C. Johnson. A status report on the observability of cosmic buble collision. 08 2009. URL `http://arxiv.org/abs/0908.4105`.

Anthony Aguirre, Matthew C Johnson, and Assaf Shomer. Towards observable signatures of other bubble universes. *Phys.Rev.D*, 76:063509, 2007. URL `http://arxiv.org/abs/0704.3473`.

Anthony Aguirre and Matthew C Johnson. Towards observable signatures of other bubble universes ii: Exact solutions for thin-wall bubble collisions. *Phys. Rev.*, D77 (123536), 12 2008. URL `http://arxiv.org/abs/0712.3038`.

Matthew Kleban, Thomas S. Levi, and Kris Sigurdson. Observing the multiverse with cosmic wakes. 09 2011. URL `http://arxiv.org/abs/1109.3473`.

S. M. Feeney, M. C. Johnson, D. J. Mortlock, and H. V. Peiris. First observational tests of eternal infation: Analysis methods and wmap 7-year results. *Phys. Rev.*, D84 (043507), 2011a.

Spencer Chang, Matthew Kleban, and Thomas S. Levi. Watching worlds collide: Effects on the cmb from cosmological bubble collisions. *JCAP*, 0904:025, 2009. URL `http://arxiv.org/abs/0810.5128`.

Bartlomiej Czech, Matthew Kleban, Klaus Larjo, Thomas S. Levi, and Kris Sigurdson. Polarizing bubble collisions. 06 2010. URL `http://arxiv.org/abs/1006.0832`.

S. M. Feeney, M. C. Johnson, D. J. Mortlock, and H. V. Peiris. First observational tests of eternal infation. *Phys. Rev. Lett.*, 107(071301), 2011b.

Z.-C. Wu. Gravitational effcts in bubble collisions. *Phys. Rev.*, D28(1898-1906), 1983.

Ian G. Moss. Black hole formation from colliding bubbles. URL `http://arxiv.org/abs/gr-qc/9405045`.

Ben Freivogel, Gary T. Horowitz, and Stephen Shenker. Colliding with a crunching bubble. *JHEP*, 0705(090), 2007. URL `http://arxiv.org/abs/hep-th/0703146`.

Spencer Chang, Matthew Kleban, and Thomas S. Levi. When worlds collide. *JCAP*, 0804(034), 12 2008. URL `http://arxiv.org/abs/0712.2261`.

A. Aguirre, M. C. Johnson, and M. Tysanner. Surviving the crash: assessing the aftermath of cosmic bubble collisions. *Phys. Rev.*, D79(23514), 2009.

Matthew C. Johnson, Hiranya V. Peiris, and Luis Lehner. Determining the outcome of cosmic bubble collisions in full general relativity. *Phys.Rev. D85 (2012) 083516*, 2012. URL `http://arxiv.org/abs/1112.4487`.

Michael P. Salem. Bubble collisions and measures of the multiverse. *JCAP*, 1201(021), 08 2012. URL `http://arxiv.org/abs/1108.0040`.

Stephen M. Feeney, Matthew C. Johnson, Jason D. McEwen, Daniel J. Mortlock, and Hiranya V. Peiris. Hierarchical bayesian detection algorithm for early-universe relics in the cosmic microwave background. *Phys.Rev.*, D88(043012), 10 2013. URL `http://arxiv.org/abs/1210.2725`.

J. D. McEwen, S. M. Feeney, M. C. Johnson, and H. V. Peiris. Optimal filters for detecting cosmic bubble collisions. *Phys. Rev.*, D85(103502), 2012. URL `http://arxiv.org/abs/1202.2861`.

Stephen Osborne, Leonardo Senatore, and Kendrick Smith. Collisions with other universes: the optimal analysis of the wmap data. 05 2013. URL `http://arxiv.org/abs/1305.1964`.

K. Larjo and T. S. Levi. Bubble, bubble, flow and hubble: Large scale galaxy flow from cosmological bubble collisions. *JCAP*, 1008(034), 2010.

Marcelo Alvarez, Tobias Baldauf, J. Richard Bond, Neal Dalal, Roland de Putter, Olivier Doré, Daniel Green, Chris Hirata, Zhiqi Huang, Dragan Huterer, Donghui Jeong, Matthew C. Johnson, Elisabeth Krause, Marilena Loverde, Joel Meyers, P. Daniel Meerburg, Leonardo Senatore, Sarah Shandera, Eva Silverstein, Anže Slosar, Kendrick Smith, Matias Zaldarriaga, Valentin Assassi, Jonathan Braden, Amir Hajian, Takeshi Kobayashi, George Stein, and Alexander van Engelen. Testing inflation with large scale structure: Connecting hopes with reality. 12 2014. URL `http://arxiv.org/abs/1412.4671`.

Pengjie Zhang and Matthew C. Johnson. Testing eternal inflation with the kinetic sunyaev zel'dovich effect. 01 2015. URL `http://arxiv.org/abs/1501.00511`.

Jonathan Kozaczuk and Anthony Aguirre. Multiple cosmic collisions and the microwave background power spectrum. 06 2012. URL `http://arxiv.org/abs/1206.5038`.

Carroll L. Wainwright. Cosmotransitions: Computing cosmological phase transition temperatures and bubble profiles with multiple fields. 09 2006-2013. URL `http://arxiv.org/abs/1109.4189`.

Baumgarte and Shapiro. *Numerical Relativity: solving Einstein's Equations on the Computer.* Cambridge University Press, 2010.

R. Courant, K. Friedrichs, and H. Lewy. Uber die partiellen di erenzengleichungen der mathematischen physik. *Mathematische Annalen*, (1):32–74, 1928.

R. K. Sachs and A. M. Wolfe. Perturbations of a cosmological model and angular variations of the microwave background. *Astrophysical Journal*, 147:73.

John T. Giblin, Lam Hui, Eugene A. Lim, and I-Sheng Yang. How to run through walls: Dynamics of bubble and soilton collisions. 05 2010. URL `http://arxiv.org/abs/1005.3493`.